IJL, Issue 2, Vol. 22, 2023 **Research Article**
https://doi.org/10.31900/ijl.v22i2.390

Numerical Simulation of Metasurface Grating to Function as Polarization Modulator in Quantum Key Distribution Systems

Ali Qader Baki*, Shelan Khasro Tawfeeq

Institute of Laser for Postgraduate Studies, University of Baghdad, Baghdad, Iraq
** Email address of the Corresponding Author: ali.qader1101a@ilps.uobaghdad.edu.iq*

Article history: Received 5 Apr 2023; Revised 9 June 2023; Accepted 27 June 2023; Published online 15 Dec 2023

Abstract: Polarization modulation plays an important role in polarization encoding in quantum key distribution. By using polarization modulation, quantum key distribution systems become more compact and more vulnerable as one laser source is used instead of using multiple laser sources that may cause side-channel attacks. Metasurfaces with their exceptional optical properties have led to the development of versatile ultrathin optical devices. They are made up of planar arrays of resonant or nearly resonant subwavelength pieces and provide complete control over reflected and transmitted electromagnetic waves opening several possibilities for the development of innovative optical components. In this work, the Si nanowire metasurface grating polarizer is designed by COMSOL Multiphysics Software to operate in the visible region and transmit the transverse magnetic polarization of light. The same structure can be rotated by different angles, i.e., 90°, 45°, and -45° to mimic the function of polarization modulation in quantum key distribution systems. The designed structure has an extinction ratio of ~ 60000 and a wide angular tolerance range of (-20° - 20°).

Keywords: resonance grating; subwavelength grating; metasurfaces; wire-grid polarizer.

1. Introduction

Quantum key distribution (QKD) was initially suggested in 1984 and has advanced significantly over the past few decades in fiber and free space. QKD is a perfect solution for distributing an absolute secret key between two remote parties. It can be considered as one of the first practical applications that is based on single photons. Moreover, satellite-to-ground QKD and the satellite-relayed intercontinental quantum network have been successfully realized by the quantum science satellite, Micius [1,2]. QKD enables two spatially separated parties, i.e., Alice and Bob, to produce a private and secure cryptographic key based on the laws of quantum physics. This can be done by the exchange of qubits that are encoded into individual photons [3]. Polarization modulation plays an important role in polarization encoding QKD.

Polarization encoding is to a large extent employed in fiber-based QKD and free-space QKD, for which weak coherent pulses are typically encoded into four polarization states, i.e., horizontal $|H\rangle$, vertical $|V\rangle$, $|D\rangle = \frac{1}{\sqrt{2}}(|H\rangle + |V\rangle)$ and, $|A\rangle = \frac{1}{\sqrt{2}}(|H\rangle - |V\rangle)$ [1].

Mainly the multiple-laser scheme is widely used in QKD systems, where each required polarization state is prepared by an independent laser source. However, side-channel information leakage is the most critical issue that affects the performance of these systems [4].

Production of quantum key at competitive rates requires the high-frequency generation of polarization states, which is a challenge. Polarization controllers do not provide the GHz state frequencies needed for present-day QKD setups. The simplest fast QKD configuration for Alice consists of four independent laser sources, one for each state of polarization required, e.g. BB84 protocol [5]. But the indistinguishability of pulses emitted from different laser sources will be hard to guarantee, resulting in the system's vulnerability. Bob as well needs to modify the state of polarization arriving at his station to select the measurement basis [6].

A significantly higher repetition rate with inherent homogeneity in other photon dimensions can be achieved by using the external polarization modulation technique. Essentially, the concept of polarization modulation involves phase modification in particular polarization bases [1]. In order to prevent side-channel attacks a single laser source with an active polarization modulator is typically used. One option is to use the Pockels effect of fast electro-optical $LiNbO_3$ phase modulators to switch the polarization. This type of modulator is based on balanced interferometers. Two orthogonal polarization components enter different arms of the interferometer via a polarization beam splitter, after that one of the components experiences a phase shift induced by the modulator. As a result, two diagonal and two circular states can be generated [6]. Another option is based on the use of birefringent phase modulators in an in-line configuration [3]. In these schemes, the photons are injected in the phase modulator that basically consists of $LiNBO_3$ crystal with a polarization state that is diagonal with respect to the optical axis of the modulator's crystal. By applying a bias voltage, the ordinary and extraordinary refractive indices of the crystal vary independently, where the relative phase between the $|H\rangle$ and $|V\rangle$ polarization is controlled. This option presents several disadvantages. First, the polarization modulation is highly sensitive to temperature and bias voltage drift and requires active stabilization. A second issue is related to the polarization mode dispersion (PMD) induced by the birefringence, which reduces the degree of polarization for short pulses, i.e., decreasing the modulation performance. Thirdly, high voltages are required for these modulators to induce the required polarization modulation [7,8].

Other types were proposed such as a self-compensating polarization encoder based on $LiNBO_3$ phase modulator inside a Sagnac interferometer [9]. Using homogeneous birefringent metasurfaces that are composed of identical elements with varied responses for two linearly polarized orthogonal components (E_x and E_y) is the new technique for polarization conversion [9].

Metasurfaces are composed of distinctively designed subwavelength units in a two-dimensional plane, providing a new principle to design ultra-compact optical elements that show great potential for miniaturizing optical systems. By employing metasurfaces, various parameters of the light wave can be manipulated, such as pixelated polarization manipulation in the subwavelength scale which is a distinguished ability of metasurfaces compared to traditional optical components. But, plasmonic-type metasurfaces have an intrinsic ohmic loss that highly hinders their broad applications due to their low efficiency. Accordingly, metasurfaces composed of high-refractive-index all-dielectric antennas have been proposed to achieve highly efficient optical devices [11].

Compared to conventional optical components that provide wavefront engineering by phase accumulation through light propagation in the medium, metasurfaces have new degrees of freedom to control the phase, amplitude, and polarization response with subwavelength resolution. In addition, wavefront shaping within a distance much less than the wavelength can be accomplished. Their exceptional optical properties have led to the development of versatile ultrathin optical devices [12].

To support extensive phase coverage and low resonance loss, the materials used for dielectric metasurfaces must have a high refractive index (n) and low extinction coefficient (κ). The main materials used for dielectric metasurfaces include Silicon (Si), Gallium nitride (GaN), Titanium dioxide (TiO_2), and Silicon Nitride (SiNx). Si-based metasurfaces are regarded as low-cost metasurface platforms because Si is an abundant element and can be easily processed using standard CMOS-compatible manufacturing techniques [13].

In this work, Si nanowire metasurface grating polarizer that controls the wavefront of incident light is designed and its performance is numerically investigated. COMSOL Multiphysics Software is used to design the proposed structure. The metasurface grating is designed to transmit the transverse magnetic (TM) polarized light. The same structure transmits linearly polarized light with an electric field vector oriented at 0^o, 90^o, 45^o, and -45^o by changing the orientation of the grating. The designed structure can be used for obtaining four states of polarization of light passing through it, so it can replace polarization modulators in QKD systems.

2. Theory of Operation

Guided-mode resonance is a phenomenon that happens at subwavelength grating structures. The term "guided-mode resonance" appeared in 1990 by Wang et al. in an attempt to clearly communicate the fundamental physics governing these phenomena [14].

Figure 1 illustrates the resonant grating waveguide structure. These periodic photonic lattices are also referred to as "metasurfaces" or "metamaterials" in which periodically aligned subwavelength-scale features enable manipulation of incoming electromagnetic waves in a desired manner. The resonant grating waveguide consists of a substrate, a waveguide layer, and a grating layer. When a light beam is incident on such a structure, part of the beam is directly transmitted through the structure, and part is diffracted by the grating and is trapped in the waveguide layer. Part of the trapped light in the waveguide layer is then rediffracted out and it interferes destructively with the transmitted part of the light beam. Resonance happens at a specific wavelength and angular orientation of the incident beam; namely, complete interference occurs, and no light is transmitted [15].

At resonance, coupling is achieved between the diffracted light by subwavelength grating, and the waveguide mode and propagates in the lateral direction. During propagation, the mode leaks out due to the presence of the grating on the waveguide. The constructive (destructive) interference based on the phase difference between the outgoing "leaky" wave and the directly reflected wave from the grating surface forms a reflection (transmission) resonance in the optical spectrum of the device. Accordingly, the guided mode resonance device can be seen as operating in light capture, storage, and release modes. The guided-mode resonance emphasizes the capture of photonic energy whereas leaky-mode resonance emphasizes the release of photonic energy [14].

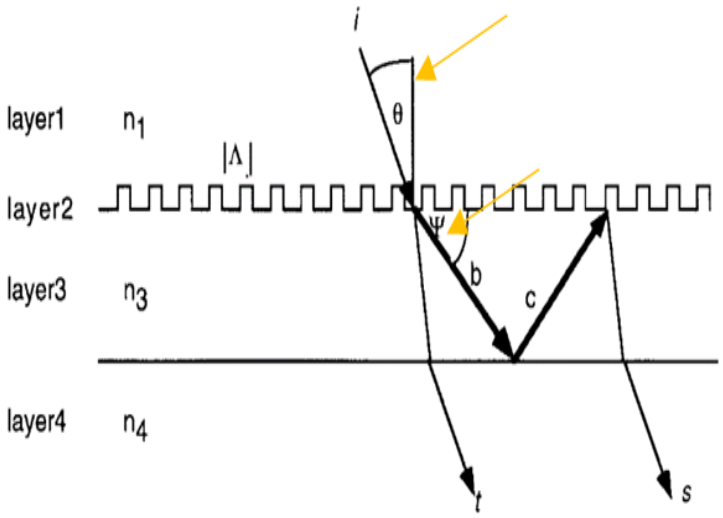

Fig. 1: Grating waveguide structure. Transmitted wave t and diffracted wave s originating from the incident wave i destructively interfere at resonance [15].

3. Design and Investigation of Nanowire Metasurface Grating Polarizer

The schematic structure of the designed metasurface grating polarizer is shown in Fig.2. The structure is designed in the visible region. Based on the effect of guided-mode resonance, the metasurface structure passes the TM polarized light and blocks the TE one.

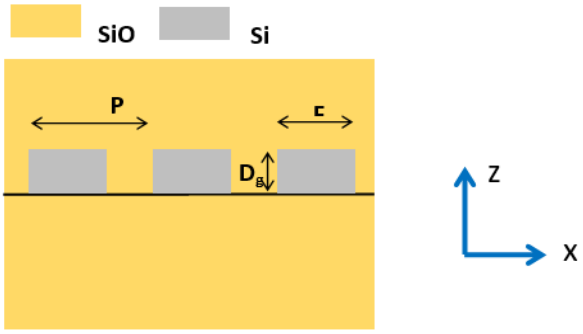

Fig. 2: Metasurface grating polarizer structure.

The structure consists of Si grating on a SiO_2 substrate of 1000 nm thickness. The grating is covered by air. The refractive indices of Si and SiO_2 are (3.8841 and 1.4570) at λ=632 nm respectively. Many optimization methods are used to design the optical components based on metasurfaces such as topology optimization, Bayesian optimization, genetic algorithm, neural networks, and particle swarm optimization method [16]. The last method is very popular for the optimization of metasurface structures especially those consisting of nanowire grating. In this work 2-D framework with Monte Carlo solver optimization supported by COMSOL was used to find the optimum dimensions of the metasurface grating polarizer. In the Monte Carlo solver optimization method, the points are sampled randomly within a uniform distribution by a user-specified box. The Monte Carlo solver is efficient in gathering statistical data for the variations in design parameters by analyzing the range of value of the objective function that is maximized (or minimized) considering several constraints. The optimum dimensions will give maximum transmittance for TM polarization and minimum transmittance for the transverse electric (TE) polarization. The optimum dimensions for P, Dg, and FF are 368 nm, 82 nm, and 0.2465 respectively. Figure 3 (a) shows the transmittance of zero-order TM and TE polarization. The extinction ratio (ER) which is defined as ($ER = T_{TM}/T_{TE}$) is shown in Fig.3 (b). Maximum ER ~ 60000 at λ= 632 nm.

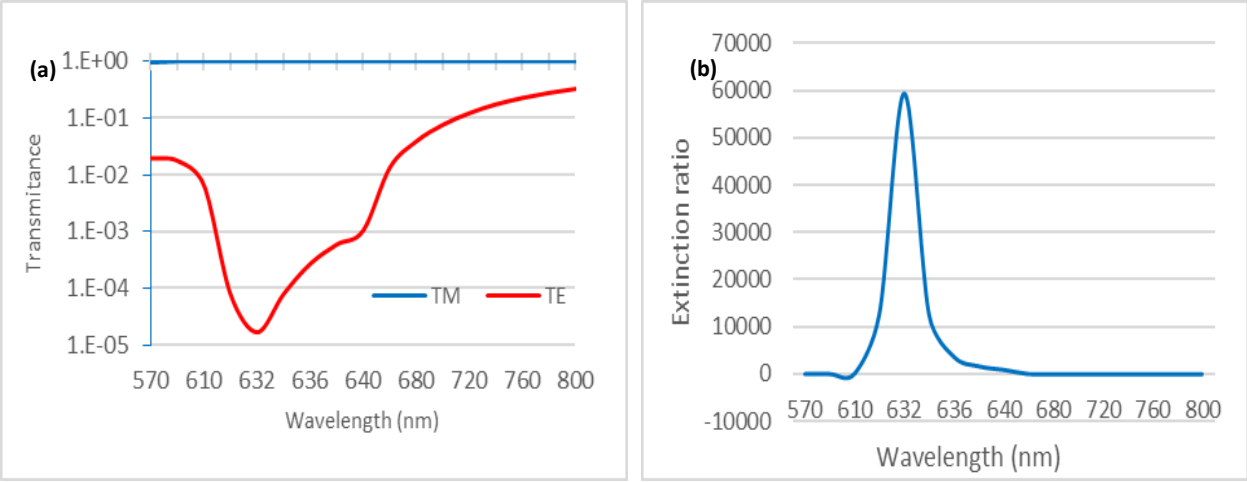

Fig. 3: Metasurface grating polarizer a) Transmittance of TM and TE polarized states (b) ER of metasurface grating polarizer where P, D_g, and FF are 368 nm, 82 nm, and 0.2465 respectively.

The maps of electric field distribution for TM and TE transmission as a function of incidence angle are shown in Fig.4 (a) and (b) respectively. The high transmission and low transmission are shown by red areas and blue areas respectively.

The proposed structure can be rotated by a specific angle so that the orientation of the electric field can be varied which means different polarization of light can be obtained. Figure 5 shows four orientations for the designed metasurface grating polarizer, i.e., 0^{o} (the proposed structure), 90^{o}, 45^{o}, and -45^{o}. The proposed structure can be fabricated and mounted on a suitable rotating base that can be rotated randomly to obtain the polarization states of light in many protocols in QKD systems.

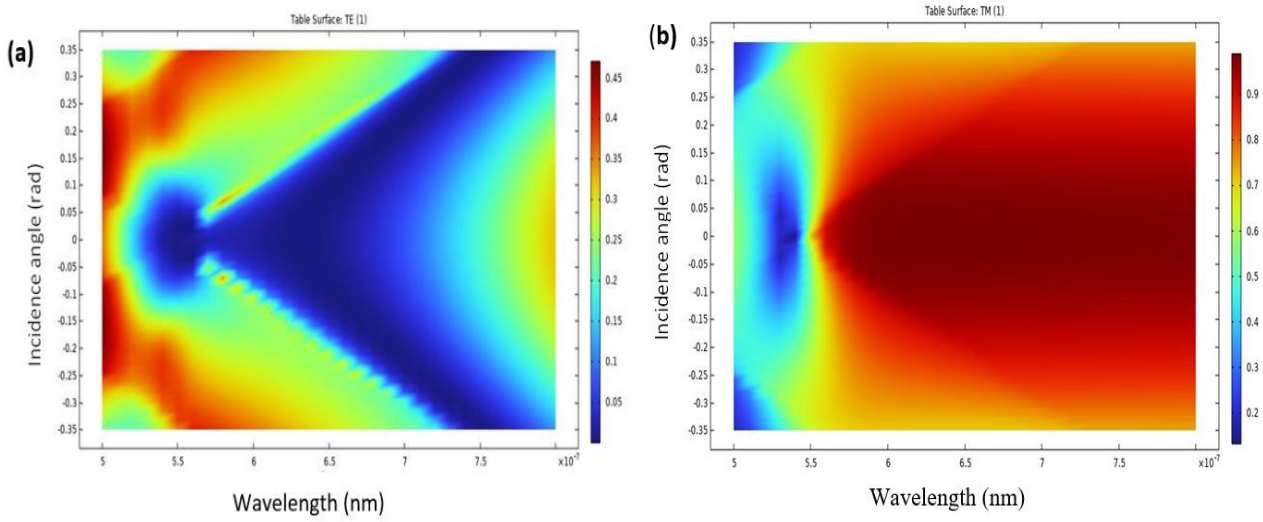

Fig. 4: Transmission map of metasurface polarizer as a function of incidence angle for (a) TM and (b) TE.

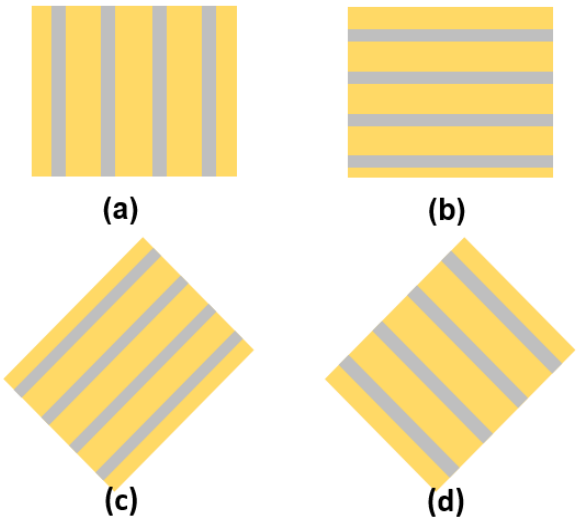

Fig. 5: Samples of Metasurface grating.

4. Conclusions

A Silicon nanowire metasurface grating polarizer operating in the visible region has been numerically designed and its performance to transmit TM-polarized light has been investigated. The design structure showed high ER ~60000 and wide angular tolerance ranging from -20^{o} to +20^{o}. This structure can be used in QKD systems to replace polarization modulators which a key optical component needed to provide the polarization state for photon encoding.

References

[1] Yang Li, Yu-Huai Li, Hong-Bo Xie, Zheng-Ping Li, Xiao Jiang, Wen-Qi Cai, Ji-Gang Ren, Juan Yin, Sheng-Kai Liao, And Cheng-Zhi Peng, "High-speed robust polarization modulation for quantum key distribution", Optics Letters, **44 (**21), 5262-5265 (2019).
[2] Salwa M. Salih, Shelan K. Tawfeeq, and Ahmed I. Khaleel, "Generation of true random ttl signals for quantum key distribution systems based on true random binary sequences", Iraqi J. Laser, **18** (1),31-42 (2019).
[3] Marco Avesani, Costantino Agnesi, Andrea Stanco, Giuseppe Vallone, and Paolo Villoresi, "Stable, low-error and calibration-free polarization encoder for free-space quantum communication", Optics Letters,**45**(17),4706-4709 (2020).
[4] Costantino Agnesi, Marco Avesani, Andrea Stanco, Paolo Villoresi, and Giuseppe Vallone, "All-fiber autocompensating polarization encoder for Quantum Key Distribution", Optics Letters, **44**(10), 2398-2401 (2019).
[5] Charles H. Bennett and Gilles Brassard, "Public Key Distribution and Coin Tossing", International Conference on Computers, System and Signal Processing, India, Volume 1, (1984).
[6] A. Duplinskiy, V. Ustimchik, A. Kanapin, V. Kurochkin, And Y. Kurochkin, "Low loss Qkd optical scheme for fast polarization encoding", Optics Express, **25** (23), 28886-28897 (2017).
[7] Fadri Grunenfelder, Alberto Boaron, Davide Rusca, Anthony Martin, and Hugo Zbinden, "Simple and high-speed polarization-based QKD", Scilight, Appl. Phys. Lett. **112**, 051108 (2018).
[8] M. Jofre, A. Gardelein, G. Anzolin, G. Molina-Terriza, J. P. Torres, M. W. Mitchell, and V. Pruneri, "100 MHz Amplitude and polarization modulated optical source for free-space quantum key distribution at 850 nm", Journal of Lightwave Technology, **28 (**17), 2572-2578 (2010).
[9] Costantino Agnesi, Marco Avesani, Andrea Stanco, Paolo Villoresi, and Giuseppe Vallone, "All-fiber self-compensating polarization encoder for quantum key distribution", Optics Letters, **44**(10), 2398-2401 (2019).
[10] Fei Ding, Shiwei Tang, and Sergey I. Bozhevolnyi, "Recent advances in polarization-encoded optical metasurfaces", Advanced Photonics Research, Res., **2**, 2000173 (2021).
[11] Yueqiang Hu, Xudong Wang, Xuhao Luo, Xiangnian Ou, Ling Li, Yiqin Chen, Ping Yang, Shuai Wang, and Huigao Duan, "All-dielectric metasurfaces for polarization manipulation: principles and emerging applications", Nanophotonics, **9**(12), 3755–3780 (2020).
[12] Hui-Hsin Hsiao, Cheng Hung Chu, and Din Ping Tsai, "Fundamentals and applications of metasurfaces", Advanced Science News, (2017).
[13] Wei-Lun Hsu, Yen-Chun Chen, Shang Ping Yeh, Qiu-Chun Zeng, Yao-Wei Huang, and Chih-Ming Wang, "Review of metasurfaces and metadevices: advantages of different materials and fabrications", Nanomaterials, **12**, 1973 (2022).
[14] S. S. Wang, R. Magnusson, and J. S. Bagby, "Guided-mode resonances in planar dielectric-layer diffraction gratings", J. Opt. Soc. Am. **7,** (1990).
[15] David Rosenblatt, Member, Avner Sharon, and Asher A. Friesem, "Resonant grating waveguide structures", IEEE Journal of Quantum Electronics, **33(**11), 2985-2993 (1997).
[16] Mahmoud M. R. Elsawy, Stephane Lanteri, Regis Duvigneau, Jonathan A. Fan, and Patrice Genevet, "Numerical optimization methods for metasurfaces", Laser & Photonics Reviews, **14** (10), 1900445 (2020).

تصميم رقمي لمحزز حيود بسطح فعال يعمل كمضمن استقطاب لمنظومات توزيع المفتاح الكمي

علي قادر بكي* , شيلان خسرو توفيق

معهد الليزر للدراسات العليا، جامعة بغداد، بغداد، العراق

*البريد الالكتروني للباحث: ali.qader1101a@ilps.uobaghdad.edu.iq

الخلاصة: يلعب مضمن الاستقطاب دورا هاما في ترميز الاستقطاب في توزيع المفتاح الكمي. باستخدام مضمن الاستقطاب، تصبح انظمة توزيع المفتاح الكمي اكثر ترتيبا وامانا حيث يتم استخدام مصدر ليزري واحد بدلا من استخدام عدة مصادر ليزرية قد تتسبب في حدوث هجمات تتسرب من خلالها المعلومات. ادى التطور في الخصائص البصرية الاستثنائية للاسطح الفعالة الى ظهور اجهزة بصرية فائقة الصغر ومتعددة الاستخدامات. حيث تتكون هذه الاسطح الفعالة من مصفوفات مستوية لاجزاء بابعاد تعادل اجزاء من الطول الموجي في حالة رنين او قريبة من الرنين توفر تحكما كاملا في الموجات الكهرومغناطيسية المنعكسة والمرسلة مما يوفر امكانيات عديدة لتطوير تراكيب بصرية مبتكرة. في هذا العمل، تم تصميم مستقطب من محزز حيود لسطح فعال من مادة السليكون باستخدام برامجيات كومسل ذو الفيزياء المتعددة ليعمل في المنطقة المرئية ويسمح بمرور الاستقطاب المغناطيسي المستعرَض. يمكن تدوير نفس التركيب بزوايا مختلفة، اي 90 درجة، 45 درجة و-45 درجة ليماثل وظيفة مضمن الاستقطاب في انظمة توزيع المفتاح الكمي. يمتلك التركيب المصمم نسبة فصل تساوي تقريبا 60000 ومدى تفاوت زاوي واسع من -20 درجة الى 20 درجة.

IJL, Issue 2, Vol. 22, 2023 **Research Article**
https://doi.org/10.31900/ijl.v22i2.389

Photocatalytic Performance of AgNPs-Zeolite Composite by Hydrothermal Synthesis for Water Splitting

Rua'a F. Ahmed*, Mohamed K. Dhahir

Institute of Laser for Postgraduate Studies, University of Baghdad, Baghdad, Iraq
** Email address of the Corresponding Author:ruaa.fawzi1201a@ilps.uobaghdad.edu.iq*

Article history: Received 1 Apr 2023; Revised 1 July 2023; Accepted 5 July 2023; Published online 15 Dec 2023

Abstract: Two samples of (Ag NPs-zeolite) nanocomposite thin films have been prepared by easy hydrothermal method for 4 hours and 8 hours inside the hydrothermal autoclave at temperatures of 100°C. The two samples were used in a photoelectrochemical cell as a photocatalyst inside a cell consisting of three electrodes: the working electrode photoanode (AgNPs-zeolite), platinum as a cathode electrode, and Ag/AgCl as a reference electrode, to study the performance of AgNPs-zeolite under dark current and 473 nm laser light for water splitting. The results show the high performance of an eight-hour sample with high crystallinity compared with a four-hour sample as a reliable photocatalyst to generate hydrogen for renewable energies.

Keywords: nanocomposite, PEC water splitting, catalyst, hydrothermal synthesis, zeolite.

1. Introduction

Water splitting via photoelectrochemical cell (PEC) technology offers a sophisticated method and useful strategy for dealing with the issues of energy and environmental crises by converting light energy to produce hydrogen fuel by splitting water reactions, which divide water into O_2 and H_2 ($2H_2O \rightarrow 2H_2+O_2$). In the PEC process, the water-splitting reaction needs photon energy to be catalyzed by a photocatalyst. To resist the positive free energy result from PEC water splitting. Where it needs stable electrodes, effective photoelectrodes, and scalable PEC cells with cost-effective operation for large-scale hydrogen production [1,2], as shown in Fig.1.

Noble metal nanoparticles were used in PEC cells, where metallic nanoparticles (NP) are attracting the interest of chemists due to their novel properties, which include a high surface area and exceptional surface activity that provide excellent catalytic, optical, and electrical properties. where specifically found in noble metals such as gold and silver or the subnanometric particles contained in zeolites. Zeolite, an alkali or alkaline-earth metal hydrated aluminosilicate mineral, has received a lot of attention lately as a readily accessible and affordable natural mineral [4], which is a significant class of functional materials. Porous zeolites are anticipated to attain high H_2 evolution efficiency due to their distinctive and large surface area.

The family of zeolites is well-known as a class of crystalline porous materials with high catalytic activity, well-confined periodic porous structure, acid resistance, and ion exchange capability [5].

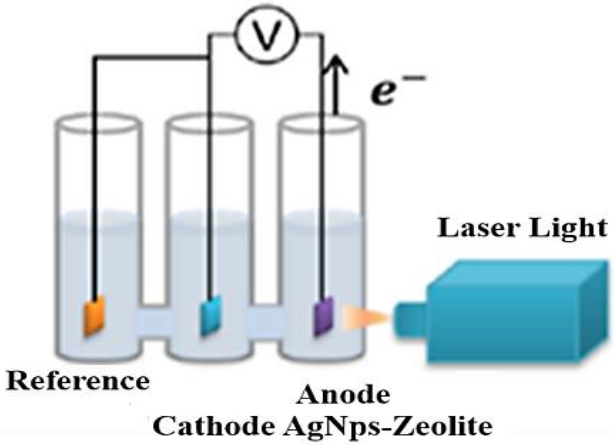

Fig.1: A diagram explaining a PEC cell with a standard three-electrode arrangement [3].

The progress made shows that the improved adsorption performance as well as the high separation and transfer efficiency of photogenerated charge carriers are crucial for the photocatalytic enhancement of zeolite-based composites. Because of their well-defined pore and channel architectures, these materials are commonly utilized as ion exchangers, catalysts, and adsorbents in industry [6]. The zeolite structure can be filled with transition metal atoms through conventional impregnation, hydrothermal processes, photosynthesis, or cation exchange using a traditional ion exchange approach [7].

Fig.2: Image of stainless-steel autoclaves with Teflon lining and internal parts (upper). The reaction chamber, which is made of stainless steel, contains the Teflon chamber. The stainless-steel chamber in the lower image is lined with Teflon and is commercially available [9].

Recently, researchers' interest in the single-pot hydrothermal approach has increased [6]. The process of hydrothermal synthesis is used to create materials at low temperatures with high vapor pressure. This approach is thought to be the most energy-efficient and environmentally benign because the reaction is carried out in closed-system settings. Typically, hydrothermal synthesis is performed in aqueous solutions using a Teflon-lined stainless-steel autoclave, as shown in Fig.2 [8]. Employing laser light as an excitation source to research photocatalyst activity has an extremely high degree of feasibility. A diode laser (473 nm) has the specific characteristics of a special laser light source, including high intensity and monochromaticity.

In this paper, AgNPs-Zeolite composites were synthesized by the hydrothermal method using an autoclave with different crystallization times (4 and 8 hours), and then the structure and morphology characterization were investigated. Also, a comparison between the samples as the best-performing catalyst in photocatalytic water splitting.

2. Materials and Methods

Ag NPs-zeolite has been synthesized by the hydrothermal method, where silver nanoparticles (0.2 g, 20 nm particle size, spherical) from Hongwu International Group Ltd., China, were dissolved in 5 mL of deionized water and 10 mL of polyethylene glycol 600 (PEG 600) from the manufacturer, Alpha Chemika, made in India, at (250C) for 30 min with stirring, and nanozeolite particles of size 50 SSA: 340 m2/gr were added (0.2 g) also with 20 mL from an absolute ethyl alcohol manufacturer. Alpha Chemika, made in India, was added to the mixture gradually with stirring for 2 hours. Finally, the crystallization method was easy; the mixture was placed inside a hydrothermal autoclave and then a thermal oven that was kept at 100 0C for 4 and 8 hours for two samples, respectively, as shown in Figure 3. The Ag-NPs-Zeolite composite was obtained after steps of filtration and drying at 100 0C for 1 hour in the oven, with the pH kept near neutral during the step of the filtration process. Then it is deposited by the distillation method on a fluorine-doped tin oxide (FTO) substrate and used as an electrode in the applications of PEC for water splitting.

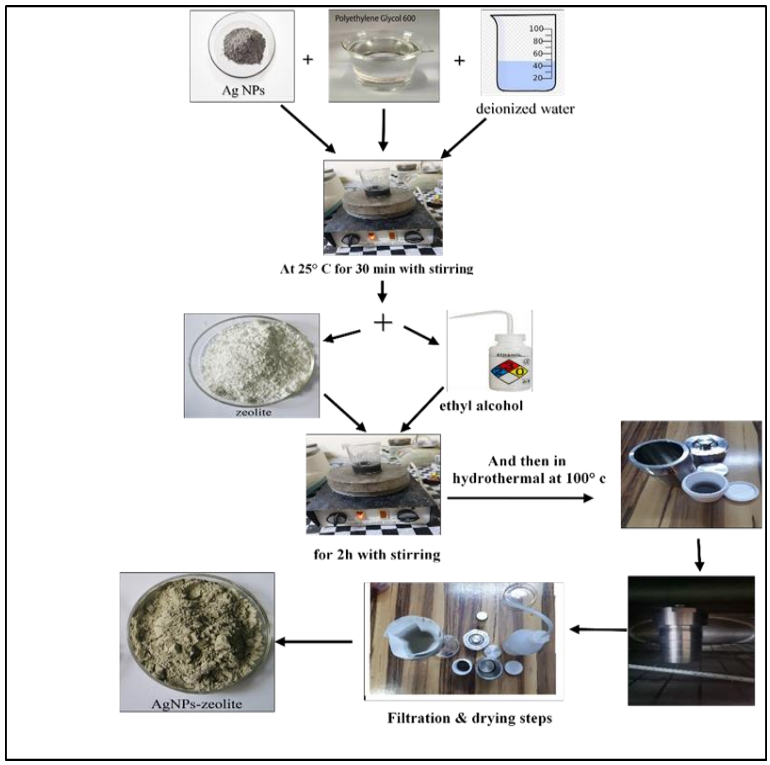

Fig.3: Ag NPs-Zeolite composite preparation steps.

3. Characterization

The X-ray diffraction (XRD-6000) SHIMADZU 220V/50Hz (Japan) patterns of the samples were recorded using a diffractometer operating with a Cu -Kα radiation in the 2θ angle range 50–800 with a step of 0.05° and with 0.60 s of accumulation at each point. A field emission scanning electron microscope (FESEM) (FEI Japan) was used to determine the morphology and particle size of Ag (Np)-zeolite. The SHIMADZU UV-VIS-NIR 1800 240V (Japan) spectrophotometer was obtained using a UV-vis spectrometer, the spectra between 190 and 1100 nm were captured and the Zeta potential analysis was performed (Zeta plus Brookhaven, 90 Bundle Instruments Corporation, USA).

4. Results and Discussion

4.1 X-Ray Diffraction Analysis

Figure 4 depicts the XRD patterns of the Ag-NPs-Zeolite composite. The purpose of the XRD investigation was to learn more about the crystalline nature of the synthesized nanocomposites. The good crystalline quality of the produced samples is confirmed by the sharp peaks [10]. The absorption peaks for zeolite appeared at 2θ = 22.40, 23.10, 26.50, and 27.10. All of the Zeolites' diffraction patterns clearly correspond to those on the Zeolite standard card (JCPDS 39-0223) [6]. From Fig.4, it is shown that the zeolite is crystalline. Also, it is observed that the Ag NPs-zeolite composite has notable peaks around 2θ = 38.60, 44.70, 64.90, and 77.80, which correspond to the silver nanoparticles. (111), (200), (220), and (311) crystal planes, these peaks' development shows that the crystalline phase of silver has developed within the Zeolite framework, which, when matched with standard silver values (JCPDS 04-0783) [11], can be indexed using the facets of silver's face-centered cubic crystal structure with the lattice constants (a = b = c 4.082975 A°). These peak heights are consistent with the values in the standard card, like in the earlier reports [12,13]. Also, Fig. 4 shows that the crystallinity of the sample increases with aging time. The aging process allows for crystal size regulation. According to [14], the production of impurity phases is reduced and crystallization is accelerated. So, the longer crystallization time of the composition of (Ag NPs-Zeolite) produced a highly crystalline phase, as evidenced by the XRD peak intensity of sample 8 hours, which was more desirable in comparison with sample 4 hours.

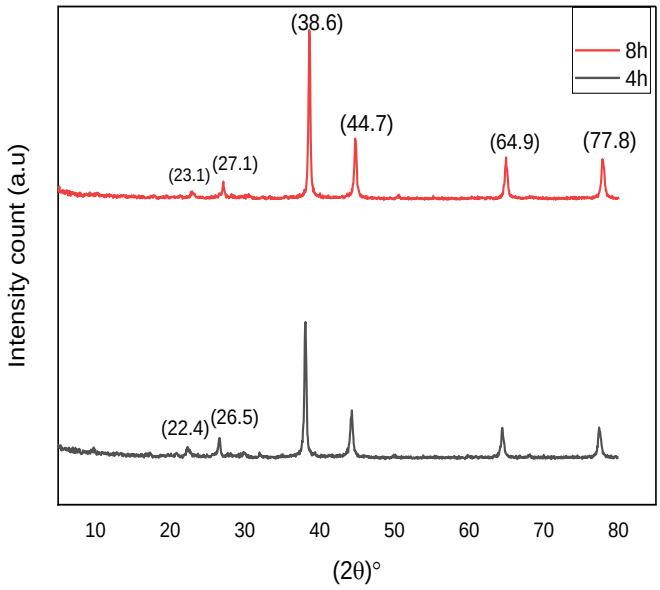

Fig. 4: XRD patterns of (Ag NPs-Zeolite) composite for two samples.

4.2 FESEM Analysis

AgNPs-zeolite electrodes were tested using field emission scanning electron microscopy. FESEM can specify the shape and particle size of samples. Figure 5(a) shows FESEM images for zeolite nanoparticles. From FESEM analysis, the morphology of the Zeolite surface appears as flakes, and their size ranges from (43-50) nm. The morphology of the composite for two samples shows a good distribution of silver nanoparticles in zeolite; this result agrees with the study in [15]. Also, silver nanoparticles are stable inside the pores of zeolite, and some of the AgNPs form clusters on the surface of the zeolite as shown in Fig. 5(b) for the sample after 4 hours with particle sizes ranging between (88–183) nm. Figure 5(c) illustrates an AgNPs-Zeolite nanocomposite for an 8-hour sample, with particle sizes ranging between (56-193) nm**.**
Also, Fig.5(d) represents that the longer the crystallization time, the larger the average particle size; this means that the higher the crystallization time for (Ag NPs-Zeolite) composite, the more metallic particles will be made up, which means convert nanoparticles to bulk material, which begin to enlarge clearly after aging time for 4 hours and 8 hours, which agrees with research [16].

The composite in the previous figures displayed a rough surface with a spherical structure for silver nanoparticles and showed many silver clusters. At 100-200 °C in a hydrothermal autoclave, reduction results in the creation of silver clusters on the surface of zeolite; this agrees with [17]. Also, some shiny spots corresponding to the AgNPs appeared on the surface of the Zeolite nanoparticle; therefore, the AgNPs were rather well distributed in the Zeolite nanoparticles. This agrees with [18].

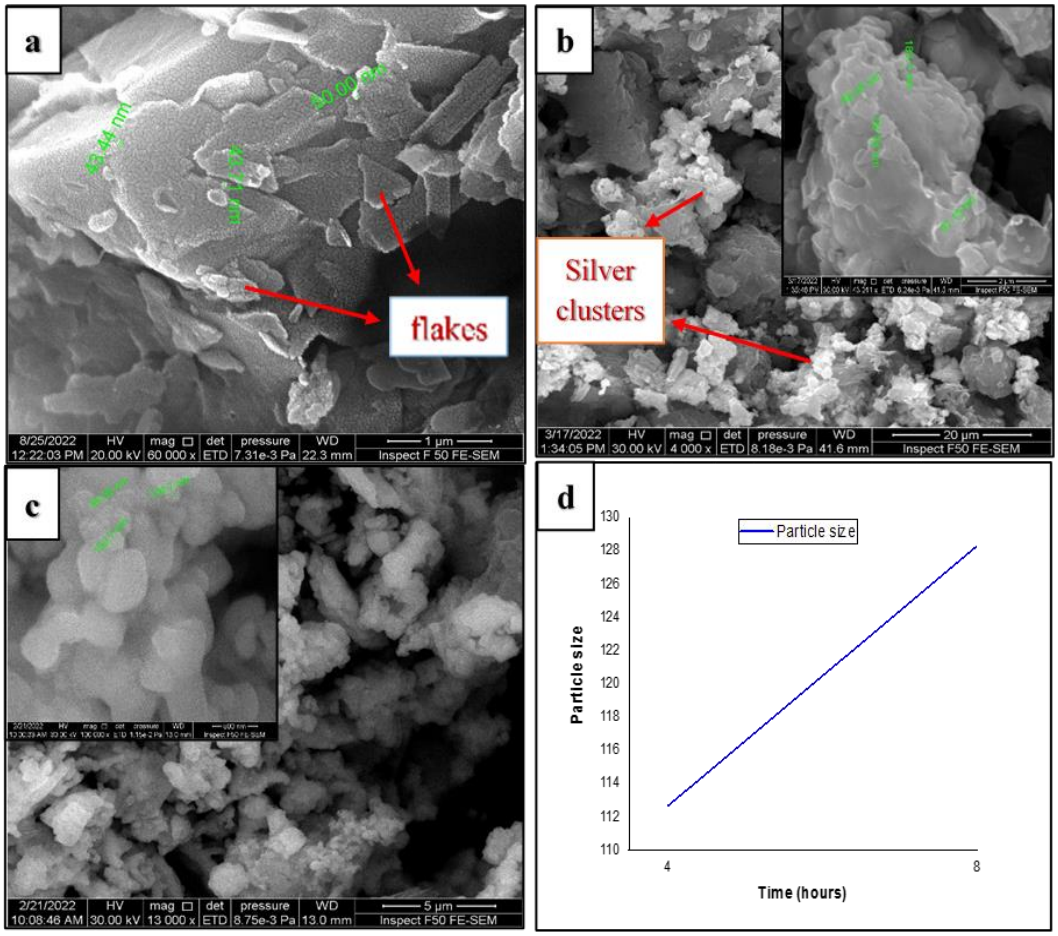

Fig.5: FESEM images for Zeolite and (Ag NPs-Zeolite) composite for two samples: (a) Zeolite, (b) a four-hour sample, (c) an eight-hour sample, and (d) the average particle size for two samples.

4.3 UV-Visible Spectral Study

Two samples exhibit a high level of absorption in the region of UV absorption. Figure 6(a) shows the highest peak of zeolite absorption at the peaks of (248,288) nm, while Fig.6 (b) shows the highest peak at (284) nm for silver. Ag species with more Ag atoms often produce UV-Vis bands at a longer wavelength, and the bands at 260 and 284 nm are attributed to Ag n δ+ (n = 4–8) clusters. This is in agreement with the research [19,20]. The reflectance spectra of the materials used (Ag NPs-Zeolite) in the visible and ultraviolet ranges were recorded below 300 nm; also, non-exchanged zeolites were observed. The silver-loaded zeolites produced stronger signals in the UV range (200–300 nm)**.**

Figure 6 depicts the absorption peaks for (Ag NPs-Zeolite) composite for two samples: 4 hours (c) and 8 hours, (d) at (291,309) and (291,296) nm, respectively. These signals have previously been linked to isolated silver ions that are present at particular locations within the zeolite framework. It also shows that the intercalation of silver ions into the zeolite structure has slightly altered the zeolite's electron structure, which is well in line with other reports [16,21]. The process of prolonging the crystallization time increases the intensity of the absorption, as shown in the 8-hour sample in Fig.6 (d), indicating the growth of the amount of metal Ag particles according to [16].

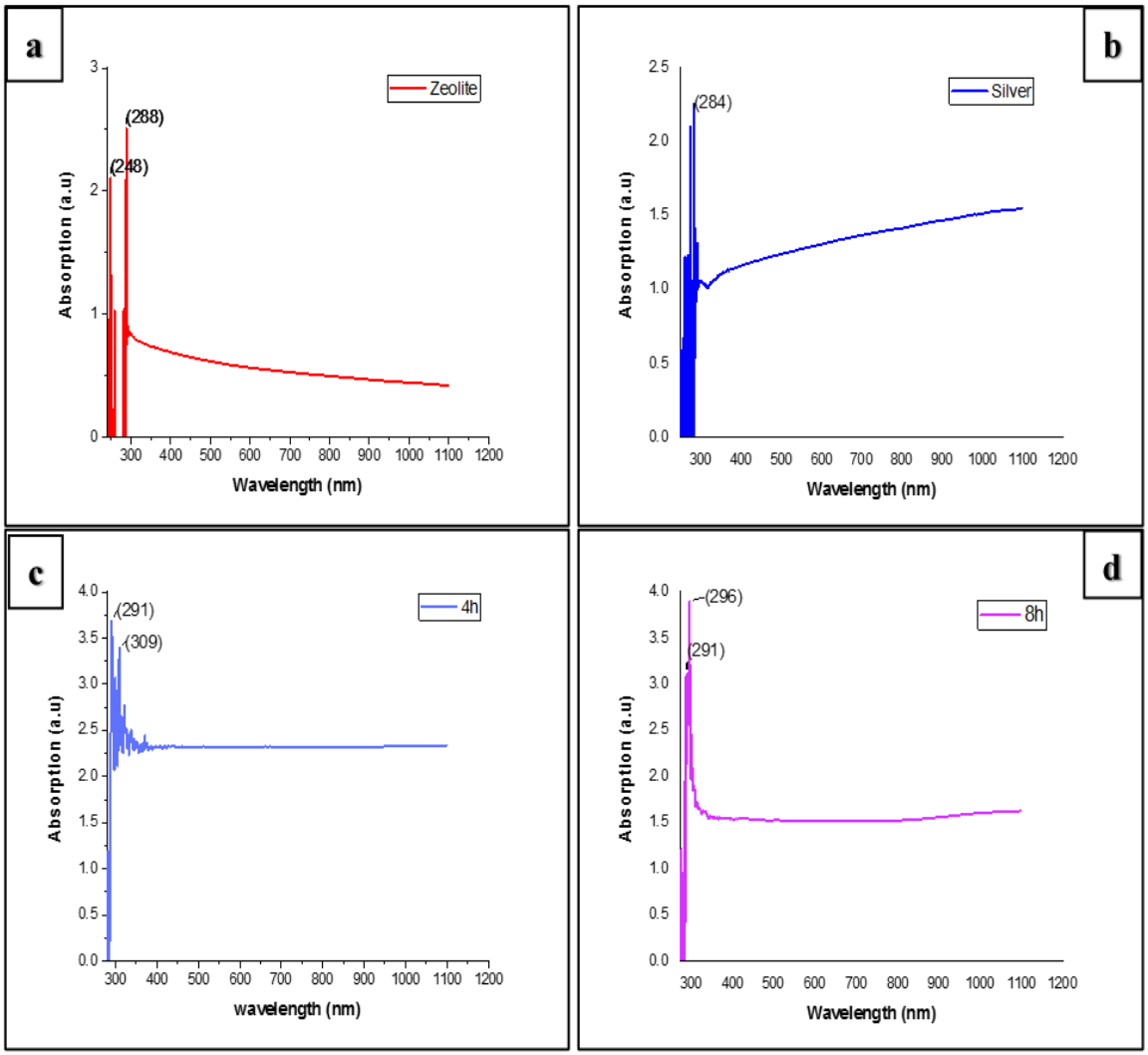

Fig.6: UV-visible spectrum for Zeolite, Silver NPs, and (Ag NPs-Zeolite) composites for two samples (a) Zeolite; (b) Silver (Ag NPs); (c) a 4-hour sample; (d) an 8-hour sample.

4.4 Zeta Potential Analysis

The zeta potential is the total charge that a particle picks up in a specific medium. The surface charge of the (AgNPs-Zeolite) composite dissolved by the solvent solution after the crystallization process by hydrothermal autoclave to obtain the measurement of (AgNPs-Zeolite) by zeta-potential. Zeta potential was typically used to gauge a surface's resistance to agglomeration. The stability of an (AgNPs-Zeolite) composite in colloidal form can be predicted using the zeta potential, with a value of greater than +30 mV or less than -30 mV suggesting the least amount of particle aggregation brought on by electrostatic attraction. Where the electrical stability of colloids increases when their zeta potentials, whether negative or positive, are enhanced, whereas aggregates and agglomerates are described by low zeta potential values, which is supported by [22, 23]. The surface charge for Zeta potential for the (Ag NPs-Zeolite) composite is illustrated in Fig.7. It has low stability of the (Ag-Zeolite) nanoparticles, mobility values, and zeta potential values for the two samples observed in Table 1. This explains the presence of silver nanoclusters on the surface of the zeolite in the above FESEM images.

Table 1: The values of the zeta potential and the mobility of the (Ag-Zeolite) nanoparticle solution.

The Nanoparticle solution	Zeta potential (mV)	The mobility ($m^2 V^{-1} s^{-1}$)
Ag-Zeolite	- 25.01	-1.95

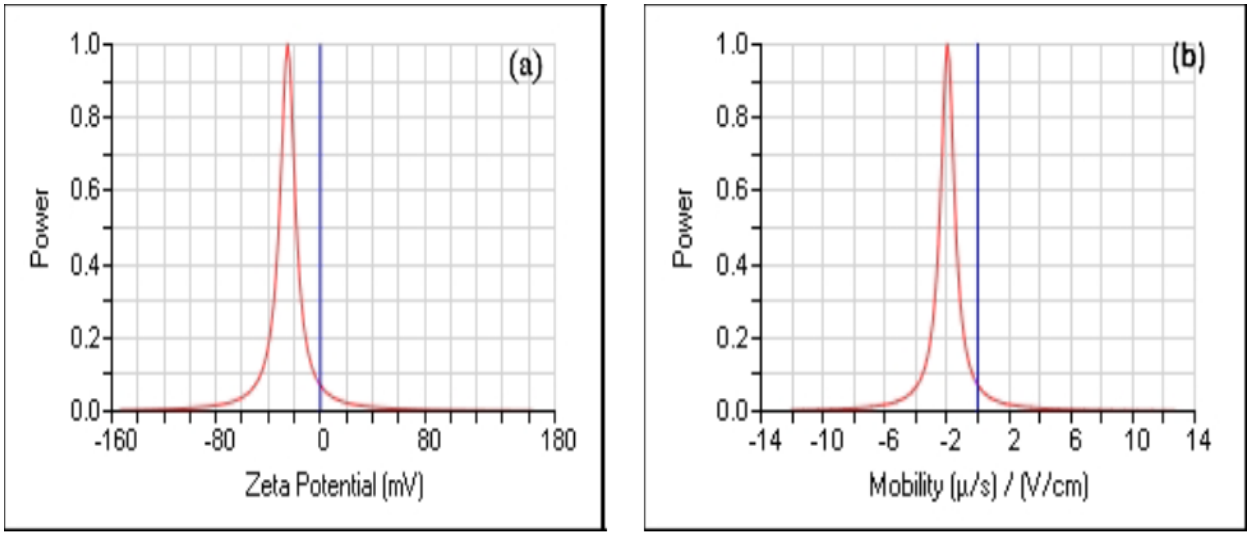

Fig.7: (a) the (Ag-Zeolite) nanoparticle solution's zeta potential (mv); (b) the (Ag-Zeolite) nanoparticle solution's mobility ($m^2 V^{-1} s^{-1}$).

5. Characterization of AgNPs-Zeolite Photocatalyst Performance in a Photoelectrochemical Cell at Dark Current Density and 473nm Laser Illumination

A photoelectrochemical cell containing three electrodes with an electrochemical workstation from (ER466, EDAQ company Australia, potential stat) was used to study the behavior of Ag NPs-Zeolite Photocatalyst. Firstly, at dark current density, and secondly, at 473 nm laser illumination, as shown in Fig.8.

Table 2: The J values at dark current and 473 nm laser illumination for each sample at 1 volt.

NO.	The samples	J mAcm^{-2} at Dark current	J $_{laser}$ (473nm) mA cm^{-2} at (200 mW cm^{-2})
1	AgNPs-Zeolite at 4 hours	0.0427	0.05061
2	AgNPs-Zeolite at 8 hours	0.0731	0.08511

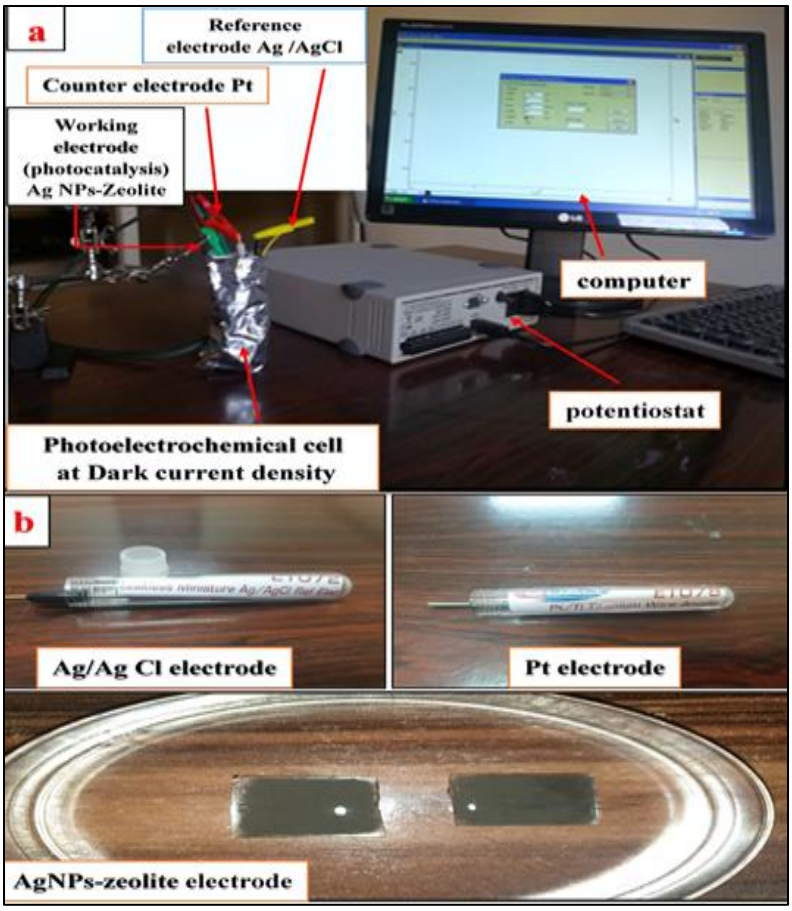

Fig.8: (a) AgNPs-Zeolite Photocatalyst at Dark Current Density (b) Three Electrodes for Photoelectrochemical Cell.

The electrodes of a photocatalyst of (AgNPs-zeolite) nanocomposite were fabricated and employed as a photoanode to study the effectiveness of photoelectrochemical (PEC) water-splitting for AgNPs-zeolite under dark and laser light irradiation. The PEC water splitting performance of the AgNPs-zeolite nanocomposite was measured using linear sweep voltammetry (LSV) techniques to estimate the current density for PEC. Table 2 and Fig.9 of two samples show the electrode's current density increased gradually from (0.0427 to 0.05061) for a 4-hour sample and from (0.0731 to 0.08511) for an 8-hour sample upon exposure to 473 nm laser light, compared with dark current at a given voltage (0–1) V versus Ag/AgCl for 60 s of a cycle. The photo-responsive property of the synthesized catalyst is demonstrated by the enhancement in the current density of (AgNPs-zeolite) nanocomposite photoanode after exposure to laser light. I-V parameters of the (AgNPs-zeolite) photoanode for PEC water-splitting results show that under

laser light illumination as compared to dark current showed a six-fold enhancement in the photocurrent density and therefore enhanced PEC performance this agrees with researchers [24].

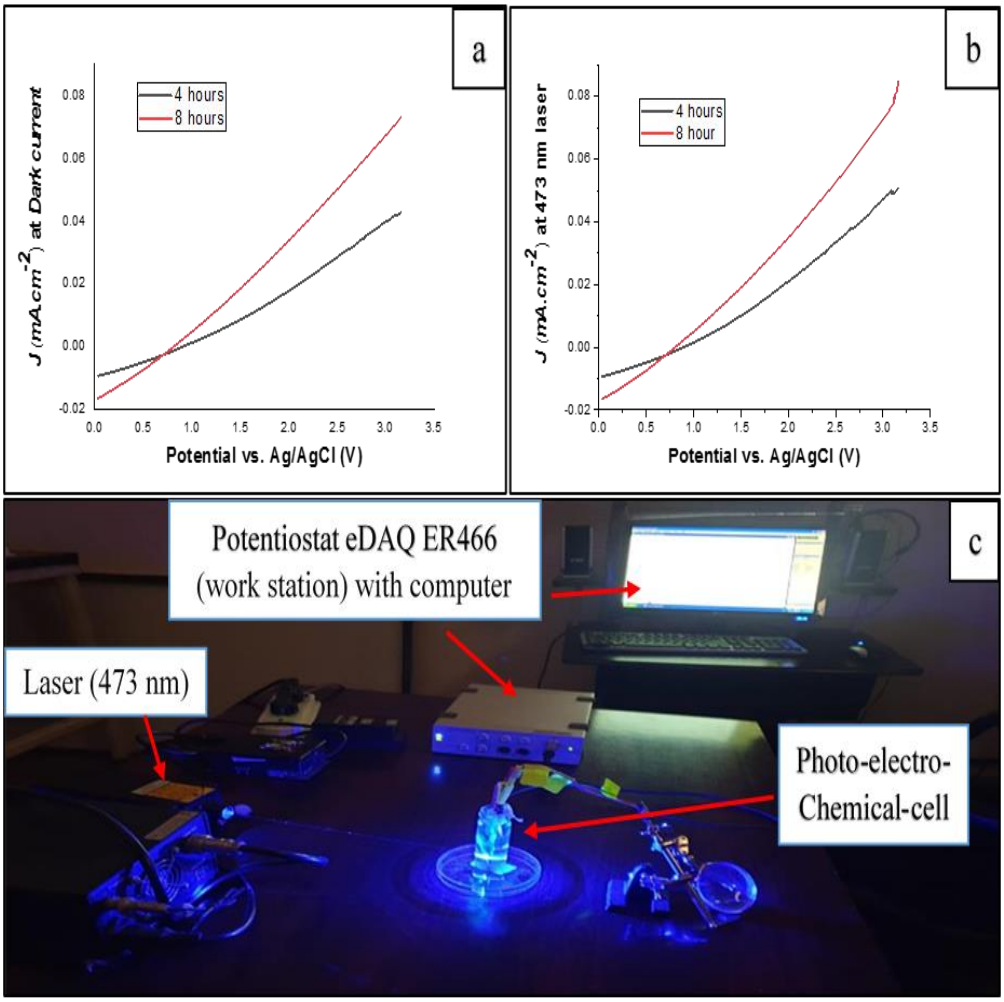

Fig.9: (a) and (b) show the linear sweep voltammetry response of (AgNPs-zeolite) nanocomposite photoanodes of two samples under dark and 473 nm laser light irradiation, respectively; (c) the AgNPs-zeolite photo anodes test for two samples under 473 nm laser light.

6. Conclusions

The results show that the (AgNPs-zeolite photocatalyst is active in improving the performance of the photoelectrochemical cell for water splitting, and the speed of response for the catalyst is good. Also, the longer crystallization time of the AgNPs-zeolite nanocomposite during the manufacturing phase inside the hydrothermal autoclave made the performance of an eight-hour sample with high crystallinity better than a four-hour sample as a reliable photocatalyst to generate hydrogen for renewable energies.

References

[1] Landman A, Halabi R, Dias P, Dotan H, Mehlmann A, Shter GE, Halabi M, Naseraldeen O, Mendes A, Grader GS, Rothschild A. "Decoupled photoelectrochemical water splitting system for centralized hydrogen production" Joule, **4**(2),448-71 (2020).

[2] Chang JH, Kumar M, Shen SY. "Fundamentals of photoelectrochemical water splitting" Nanostructured Materials for Photoelectrochemical Water Splitting IOP Publishing Ltd (2021).
[3] Lee WC. "Photoelectrochemical water splitting and gas ionisation sensing using metal oxide nanostructures" (Doctoral dissertation, University of Sussex).
[4] Torkian N, Bahrami A, Hosseini-Abari A, Momeni MM, Abdolkarimi-Mahabadi M, Bayat A, Hajipour P, Rourani HA, Abbasi MS, Torkian S, Wen Y. "Synthesis and characterization of Ag-ion-exchanged zeolite/TiO2 nanocomposites for antibacterial applications and photocatalytic degradation of antibiotics" Environmental Research., **207,**112157(2022).
[5] Cheng J, Gao C, Jing M, Lu J, Lin H, Han Z, Ni Z, Zhang D. "Photo-catalysis water splitting by platinum-loaded zeolite A." Materials Research Express, **5**(5),055506 (2018).
[6] Hu X, Bai J, Wang J, Li C, Xu W. "Preparation of 4A-zeolite-based Ag nanoparticle composite catalyst and research of the catalytic properties" RSC Advances, **5**(4), 2968-73 (2015).
[7] Shi Y, Ye S, Liao H, Liu J, Wang D. "Formation of luminescent silver-clusters and efficient energy transfer to Eu3+ in faujasite NaX zeolite. Journal of Solid State Chemistry" **285**,121227 (2020).
[8] Hussain SA, Muhammad SK, Alkhayatt AH. "Hydrothermally growth of TiO2 Nanorods, characterization and annealing temperature effect" Kuwait Journal of Science"**48**(3),(2021).
[9] Kafle BP. "Introduction to nanomaterials and application of UV–Visible spectroscopy for their characterization" Chemical analysis and material characterization by spectrophotometry,**6**,(2020).
[10] Salem MA, Elsharkawy RG, Ayad MI, Elgendy MY. "Silver nanoparticles deposition on silica, magnetite, and alumina surfaces for effective removal of Allura red from aqueous solutions" Journal of Sol-Gel Science and Technology,**91**,523-38 (2019).
[11] Agasti N, Kaushik NK. "One pot synthesis of crystalline silver nanoparticles" Am. J. Nanomater, **2**(1),4-7(2014).
[12] Sowmyya T, Lakshmi GV. "Soymida febrifuga aqueous root extract maneuvered silver nanoparticles as mercury nanosensor and potential microbicide" World Scientific News, **114**,84-105 (2018).
[13] Hamid MK, Ghafoor DA, Obaid SA. "Characteristic and anticancer activity of silver nanoparticles of graviola (ANNONA) fruit juice as a reducing agent "Biochemical & Cellular Archives, **21**(1) 2021.
[14] Nazir LS, Yeong YF, Sabdin S. "Formation of pure NaX zeolite: Effect of ageing and hydrothermal synthesis parameters" InIOP Conference Series: Materials Science and Engineering, IOP Publishing, **458,** 012002, (2018).
[15] Das S, Pérez-Ramírez J, Gong J, Dewangan N, Hidajat K, Gates BC, Kawi S. "Core–shell structured catalysts for thermocatalytic, photocatalytic, and electrocatalytic conversion of CO_2". Chemical Society Reviews.;**49**(10), 2937-3004(2020).
[16] Temerev VL, Vedyagin AA, Iost KN, Afonasenko T, Tsyrulnikov P. "Enhanced adsorption properties of Ag-loaded β-zeolite towards toluene" InMaterials Science Forum Trans Tech Publications Ltd., **917**, 180-184 (2018).
[17] Lopes CW, Martinez-Ortigosa J, Góra-Marek K, Tarach K, Vidal-Moya JA, Palomares AE, Agostini G, Blasco T, Rey F. "Zeolite-driven Ag species during redox treatments and catalytic implications for SCO of NH3" Journal of Materials Chemistry A, **9**(48), 27448-58 (2021).
[18] Mintcheva N, Panayotova M, Gicheva G, Gemishev O, Tyuliev G. "Effect of Exchangeable Ions in Natural and Modified Zeolites on Ag Content, Ag Nanoparticle Formation and Their Antibacterial Activity" Materials. **14**(15),4153(2021).
[19] Temerev VL, Vedyagin AA, Iost KN, Pirutko LV, Cherepanova SV, Kenzhin RM, Stoyanovskii VO, Trenikhin MV, Shlyapin DA. "Purification of exhaust gases from gasoline engine using adsorption-catalytic systems. Part 1: trapping of hydrocarbons by Ag-modified ZSM-5" Reaction Kinetics, Mechanisms and Catalysis. **127**(2),945-59 (2019).
[20] Shimizu K, Sawabe K, Satsuma A. "Unique catalytic features of Ag nanoclusters for selective NO x reduction and green chemical reactions" Catalysis Science & Technology, **1**(3), 331-412011.
[21] Mazzocut A, Coutino-Gonzalez E, Baekelant W, Sels B, Hofkens J, Vosch T. "Fabrication of silver nanoparticles with limited size distribution on TiO_2 containing zeolites" Physical Chemistry Chemical Physics, **16** (35),186903(2014).
[22] Inbaraj BS, Chen BY, Liao CW, Chen BH. "Green synthesis, characterization and evaluation of catalytic and antibacterial activities of chitosan, glycol chitosan and poly (γ-glutamic acid) capped gold nanoparticles" International Journal of Biological Macromolecules, **161**,1484-95 (2020).
[23] Yahiya LZ, Dhahir MK, Faris RA. "Novel and low-cost synthesis of ZNO nanorod coated by graphene oxide for enhanced physical absorption of ZNR from UV to VIS-IR region" Plant Archives, **20**(2),1005-8(2020).
[24] Baig U, Khan A, Gondal MA, Dastageer MA, Falath WS. "Laser induced anchoring of nickel oxide nanoparticles on polymeric graphitic carbon nitride sheets using pulsed laser ablation for efficient water splitting under visible light" Nanomaterials,**10** (6),1098 (2020).

أداء التحفيز الضوئي لمركب AgNPs-Zeolite عن طريق التوليف الحراري المائي لتقسيم الماء

رؤى فوزي احمد* , محمد كريم ظاهر

معهد الليزر للدراسات العليا، جامعة بغداد، بغداد، العراق

*البريد الالكتروني للباحث: ruaa.fawzi1201a@ilps.uobaghdad.edu.iq

الخلاصة: تم تحضير عينتين من الغشاء الرقيق (Ag NPs-zeolite) باستخدام طريقة حرارية مائية سهلة لمدة 4 ساعات و 8 ساعات داخل الأوتوكلاف الحراري المائي عند درجات حرارة 100 درجة مئوية. تم استخدام العينتين في خلية كهروكيميائية كمحفز ضوئي داخل خلية تتكون من ثلاثة أقطاب كهربائية: القطب الكهربائي العامل الضوئي (AgNPs-zeolite)، البلاتين كقطب كاثود ، و Ag / AgCl كقطب مرجعي لدراسة أداء AgNPs-zeolite تحت تيار مظلم وضوء ليزر 473 نانومتر لتقسيم الماء. تظهر النتائج الأداء العالي لعينة مدتها ثماني ساعات مع تبلور عالٍ مقارنة بعينة مدتها أربع ساعات كمحفز ضوئي موثوق لتوليد الهيدروجين للطاقات المتجددة.

IJL, Issue 2, Vol. 22, 2023 **Research Article**
https://doi.org/10.31900/ijl.v22i2.387

The Effect of Dual Diode Laser: (810,980) nm in Acceleration of Orthodontic Tooth Movement :A Case Report

Aya A. Assi[1,*], Rawaa A. Faris[1], Balsam Saadi Abdulhameed[2], and Sarmad S. Almalki[3]

[1]*Institute of Laser for Postgraduate Studies, University of Baghdad, Baghdad, Iraq*
[2]*Al-Imamen Al-Kadmen Medical City, Ministry of Health, Baghdad, Iraq*
[3]*Al-Karama Specialized Dental Center, Baghdad, Iraq*

* *Email address of the Corresponding Author: aya.adnan1202a@ilps.uobaghdad.edu.iq*

Article history: Received 23 May 2023; Revised 7 July 2023; Accepted 17 July 2023; Published online 15 Dec 2023

Abstract: Patients are very concerned about the lengthy nature of orthodontic treatment. It is necessary to find a non-invasive way to quicken physiologic tooth movement. This study's objective was to assess the effectiveness of low-intensity laser therapy in shortening the time and discomfort of orthodontic treatment. **Experimental work:** Using a split-mouth study to compare tooth movement with conventional treatment and laser-accelerated orthodontic tooth movement. A patient presenting with a class II division I malocclusion characterized by the misalignment of the upper and lower teeth as classified by Angle's molar classification system was indicated to undergo fixed orthodontic appliance orthodontic treatment. The treatment plan involved bilateral extraction of the upper first premolar teeth on both sides and distalization of the anterior segment to close the created space. For an experimental investigation, a patient was chosen at random and given right-side radiation using a dual diode laser (810,980 nm wavelength, 100 mW output power). **Results:** The tooth movement was measured over a period of 15 weeks; the first three orthodontic activations on the study side included scheduled laser treatment (the first month, laser-assisted treatment on days (0,3,7, and 14), the following two months, on days (0 and 14) from the day of orthodontic activation, and another 3 months of follow-up only); it was observed that orthodontic tooth movement was significantly higher in the study side than in the control side, as measured clinically using a digital vernier. We also noticed a considerable decrease in pain levels following a visual analog test. **Conclusion:** LLLT might clinically considerably speed orthodontic tooth movement and greatly lessen discomfort using the parameter settings employed in this investigation.

Keywords: bio-stimulation, low-level laser therapy, orthodontic tooth movements, and dual diode laser.

1. Introduction

The lengthy orthodontic treatment duration is one of the main issues that orthodontists and adult patients may encounter. Depending on the severity of the malocclusion and the patient, it may take adults an average of 2-3 years to finish the treatments (Ruan and Chen, 2018). This is a significant amount longer than the

time needed for adolescents. The lengthy nature of orthodontic treatments is frequently thought to increase the likelihood of patient disengagement or decreased compliance. Furthermore, root resorption, gingivitis, and tooth decay are all risks that are exacerbated by lengthy orthodontic therapy (Kanzaki et al., 2002). The piezocision technique, corticotomy, photobiomodulation, low-level laser therapy, electric stimulation, pulsed electromagnetic fields, and mechanical and physical methods, among others, have all been the subject of numerous studies looking into ways to speed up orthodontic tooth movement (Yi J. et al., 2017), (Aplimova A. et al., 2020), (Mheissen et al., 2020), and (Kau C. H. et al., 2013).

In order to support the biomechanics of tooth movements, noninvasive low-level laser treatment (LLLT) has been implemented in an orthodontic clinic. When it comes to providing analgesic and anti-inflammatory benefits, LLLT might be viewed as an alternate strategy (Li FJ et al., 2015). Pain alleviation, tooth movement, and root resorption may all benefit from it. (Turhani et al., 2006, Youssef et al., 2008, and Altan et al., 2015).

It has been demonstrated that LLLT, when administered for the right amount of time and at the right intensity, accelerates the production of fibroblasts, osteoclasts, and osteoblasts, as well as angiogenesis and collagen synthesis (S. E. Zahra et al., 2009). Red or infrared light delivers free electrons to the mitochondria's electron transport chain at the molecular level to reduce oxidative stress and produce more Adenosine Triphosphate ATP (M. Greco et al.,1989). This series of events, in turn, activates growth-signaling pathways and stimulates a number of transcription factors (A. C. Chen,2011), increasing the overall amount of growth factors produced (T. I. Karu and S. F. Kolyakov,2005).

This prospective, randomized clinical trial's objective was to determine how low-level laser therapy affected the movement of teeth under Class II orthodontic appliances.

2. Methods

This case report was created as a component of a split-mouth study to investigate the effect of low-level laser therapy on tooth movement during Class II orthodontic treatment. Parents and patients signed informed permission forms after receiving thorough information about the potential dangers and advantages. Between April and October of 2022, the orthodontic department of Al-Karama Specialized Dental Center patients ‘data were collected, and the trial protocol was registered with the Al-Karkh Directorate of the Ministry of Health.

3. Diagnosis

A 13-year-old boy patient who needed orthodontic treatment was referred to the Alkarama Specialty Dental Center's orthodontics department.To confirm the need for orthodontic treatment, a history, radiographic, and clinical examination were first carried out. The patient's clinical and medical fitness, lack of medication use, and lack of prior orthodontic treatment were all discovered during the patient's history. Patients were evaluated radiographically to rule out any issues and to assess the health of their teeth and jaws. The patient was found to have Class II division 1 malocclusion during the clinical examination due to the protrusion of the maxilla, with an increased overjet of around 8 mm, and the patient was diagnosed with class ll division l malocclusion. The specifics of the treatment plan were disclosed to the parents. The Informed Consent Form (ICF) was then signed, and the low-power laser method was used to complete the treatment.

3.1 Treatment Protocol and Follow-Up:

A. Fixed orthodontic appliance:
Upper Roth brackets (Dentarum, Germany), and NiTi wires (Dentarum, Germany) in sizes (12, 14, 16, 18, and 16x22) for leveling and alignment were used to place a fixed orthodontic device for the upper arch.

B. Extractions:

After leveling and alignment, extraction of the upper first premolar was indicated for orthodontic correction necessity and then performed.

C. Canine distalization:
A heavy gauge wire 16x22 stainless wire was used and started retraction of the anterior segment from teeth (13-23) with a crimpable hook and mini-implants by using of power chain which is activated every 3 weeks. A force gauge was also used to measure the retraction force with 150 grams. (Youssef M. et al., 2008)

D. Study design*:*
There was a split-mouth design. The study side and control side were on the same person, with the study side being on the left and the control side being on the right. An 810,980 nm gallium-aluminum-arsenide (GaAlAs) diode laser was used to administer bio-stimulation to the study side, whereas the control group just received standard orthodontic retraction.

E. Laser irradiation and parameters:
QuickLase 810+980 nm (Canterbury, United Kingdom), a high-intensity laser, was used for the procedure. The fiber was cleaved following the treatment, and all precautions were followed to maintain an aseptic chain as well as care linked to the use of laser instruments, such as the use of safety glasses by the patient, operator, and assistant. The laser settings were 12 J (2x60sx100 mW)(Doshi G. et al.,2012) for each application. Each exposure point, alongside the canine root, three points buccally and three points palatally, distributed cervically, medially, and apically, received 2 J in continuous mode, transmitted by a 300 m optical fiber, with dual wavelengths of (810+980) nm in infrared emission for 20 seconds. To perform laser irradiation following orthodontic activation, a high-intensity diode laser was employed in contact mode with these six application points (Fig. 1) and (Fig. 2a,2b).

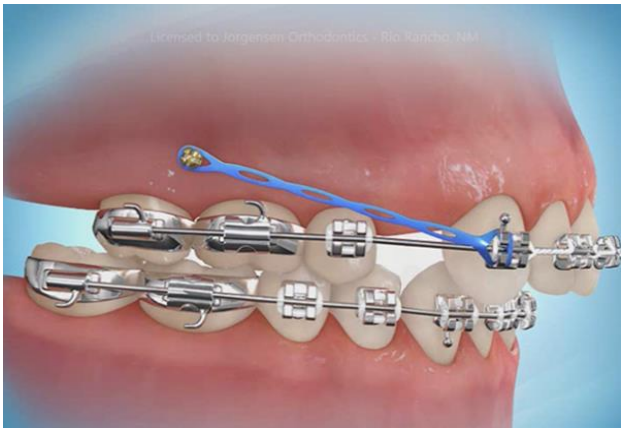

Fig. 1. Points of laser exposure along canine root (same positions buccally and palatally), 20 seconds at each point.

F. Treatment follow-up:
With a total number of 8 laser irradiation sessions, after the first orthodontic activation laser was applied on days (0,3,7,14). For the following two activations on the day (21,35) and (42,56). Measurements of extraction spaces were taken with each activation for 6 months using a digital caliper for both the study and control sides, Pain levels were also taken into account for both sides using VAS (Visual Analog Scale) for six months. Distance measurements between the cusp tip of the right and left canine and the buccal cusp of the maxillary 2nd premolar, they were considered reference points for the measurement of anterior segment movement. The distance between these two reference points was recorded every 21 days as shown in Fig. 3 (a and b). After 3 months of orthodontic activation accompanied by 8 sessions of LLL bio-stimulation,

followed by 3 months of follow-up, the study side showed space closure more than the control side (Fig. 4) as shown in Table 1, the patient also experienced pain reduction for the study side as compared for the control side.

(a) **(b)**

Fig.2. Laser irradiation inside patient's mouth: (a) buccally, and (b) palatally.

(a) **(b)**

Fig.3. Distance measurement between the two reference points for: (a) left and (b) right side inside the patient's mouth.

Fig.4. Difference in extraction space closure between experimental and control group inside patient's mouth.

Table 1: Treatment progress for study and control sides (distance and pain level).

Time interval for orthodontic activation	Distance measurement for study side in mm	Pain levels for study side	Laser irradiation for study side	Distance measurement for control side in mm	Pain levels for the control side	Laser irradiation for the control side
Day 0	15	6	✓	15	7	×
Day 3	-	-	✓	-	-	×
Day 7	-	-	✓	-	-	×
Day 14	-	-	✓	-	-	×
Day 21	14.2	1	✓	14.8	3	×
Day 35	-	-	✓	-	-	×
Day 42	13.6	0	✓	13.8	2	×
Day 56	-	-	✓	-	-	×
Day 63	12.5	0	×	13.5	0	×
Day 84	9.3	0	×	12.02	0	×
Day 105	6.16	0	×	11.15	0	×

4. Discussion

The fact that orthodontic treatment takes a long time and is uncomfortable is one of the main obstacles that may influence patients' decisions regarding the treatment. Several strategies have been investigated to quicken the process; some of these include low-level laser therapy, vibrational therapy, corticotomy-assisted orthodontics, micro-osteoperforation, pharmaceutical interventions, and innovative orthodontic appliances. These accelerating tooth movement strategies produced satisfactory outcomes by increasing the number of osteoclasts and activating already existing osteoclasts to stimulate bone resorption (Diravidamani K. et al.,2012), low-level laser therapy was one of these methods. The advantage of using such laser irradiations rather than drugs or chemicals demonstrates that they have no adverse systemic effects on the body of the patient, nor pain or discomfort, unlike other methods. In the field of medicine, various circumstances, wavelengths, and energy densities have been used to study the interactions of low-level lasers (LLL) with bone components. (Genc G et al.,2013).

laser therapy bio-stimulation effect on the acceleration of orthodontic tooth movement and reducing pain was investigated in this case report using dual diode semiconductor (GaAlAs) laser (980,810) nm with (0.1 W) power, first month: 4 times (days 0, 3, 7, 14); starting from the second month: every 15 days 2. For 20 seconds, for each point. The rate of extraction space closure can be accelerated by biostimulation using an 810 nm diode laser, it was found. As a result, it has the potential to accelerate tooth mobility during orthodontic treatment. (Arumughan S et al.,2018).

Low-level laser (LLL) effects on several cells that are intimately associated with bone remodeling, particularly osteoblasts, have been examined in cytological studies (Amid R et al.,2014). These investigations show that LLLT could encourage differentiation then proliferation. According to animal research, LLLT might have a favorable effect on bone regeneration and quicken experimental tooth movement (Kawasaki K and Shimizu N,2000) (Yoshida T et al.,2009). In the present study, both the laser and non-laser sides had relatively low pain scores. In line with earlier studies (M. Harazaki and Y. Isshiki,1997) (P. Deshpande et al.,2016), the first day of coil activation was when the highest pain scores were recorded. The amount of pain between the experimental and control groups was significantly different. Studies showing the pain-relieving effects of LLLT (Almallah M. M. E. et al.,2020) (Qamruddin I et al.,2020) during canine retraction (Doshi-Meta G and Bhad-Patil W. A.,2012). Which gave similar findings to those obtained by this case report. Youssef et al. evaluated orthodontic pain, and pain levels were collected every 21 days after the placement of nickel-titanium closed-coil springs until full canine retraction. They reported significant reductions in pain scores during all phases of low-intensity laser therapy (Youssef M. et al., 2008).

Similar results were observed in our study on day 21, as shown in Table 1, with pain levels for the study group being significantly lower than those of the control group and pain duration for the study side being shorter than that of the control side for the duration of treatment because pain caused by inflammation may be relieved by low-level laser therapy (LLLT) because it lowers levels of prostaglandin E2 (PGE2), interleukin 1 (IL1), and tumor necrosis factor (TNF), as well as oxidative stress, edema, and neutrophil influx (Alikhani M. et al.,2015). Nonetheless, some researchers find no statistically significant difference in the discomfort caused by canine retraction (Limpanichkul W. et al., 2006; Heravi F. et al., 2014) (Heravi F. et al., 2014). The patient's discomfort reaction was measured using the visual analog scale. Furthermore, some researchers evaluated the rate of tooth movement when using LLLT, Doshi et al. used laser irradiation on the study side on Days 3, 7, and 14 of the first month to determine the rate of tooth movement when LLLT was applied. After that, on the 15th of every month until canine retraction is complete. Maxilla's Mean Tooth Movement Rate increased by an average of 4.5 months at the end of months in the laser group (Doshi G. et al.,2012). Similar results were obtained by this case report with a 4.99mm space difference recorded for the study side on day 105 as demonstrated by Table 1 and Fig. 4 and canine space was nearly closed. Heravi et al. used laser irradiation on Days 4, 7, 11, 15, and 28 in the first month after Activation and on Days 32, 25, 39, 43, and 56 in the second month, and after 56 days there was no difference between the laser group and the control group (Heravi F. et al.,2014). However, in our study, it was found by using the parameters employed that the rate of retraction was almost 58% greater on the study side while the control side was only closed by nearly 25% at the end of 105 days of follow-up there was nearly 5mm difference between both sides.

5. Conclusions

Due to its bio-stimulatory effects, which generated an elevated biological response in the periodontium next to the tooth, it was concluded that LLLT could be clinically useful in accelerating orthodontic tooth movement under the conditions of the current randomized controlled experiment. In order to understand the mechanisms underlying the biostimulation effects, determine the best laser settings, and identify any adverse effects, additional research examining various irradiation parameters, longer experimental times, and more frequent time points is required.

References

Aksakalli S, Calik B, Kara B, Ezirganli S. (2016). Accelerated tooth movement with piezocision and its periodontal-transversal effects in patients with Class II malocclusion. The Angle Orthodontist., **86**(1):59-65.

Alikhani M, Alyami B, Lee IS, Almoammar S, Vongthongleur T, Alikhani M, Alansari S, Sangsuawon C, Chou M, Khoo E, Boskey A, Teixeia C.(2015).Biological saturation point during orthodontic tooth movement. Orthod Craniofacial Res.,**18**(1):8–17.

Almallah M. M. E., Hajeer M. Y., Almahdi W. H., Burhan A. S., Latifeh Y., Madkhaneh S. (2020) Assessment of a single versus double application of low-level laser therapy in pain reduction following orthodontic elastomeric separation: a randomized controlled trial. Dental and Medical Problems.,**57**(1):45–52.

Altan AB, Bicakci AA, Mutaf HI, Ozkut M, Inan VS. The effects of low-level laser therapy on orthodontically induced root resorption. (2015). Lasers Med Sci., **30**:2067–76.

Amid R, Kadkhodazadeh M, Ahsaie MG, Hakakzadeh A. (2014). Effect of low level laser therapy on proliferation and differentiation of the cells contributing in bone regeneration. J Lasers Med Sci., **5**(4):163–70.

Apalimova, A. et al. (2020). Corticotomy in orthodontic treatment: Systematic review. Heliyon, **6**, e04013.

Arumughan S, Somaiah S, Muddaiah S, Shetty B, Reddy G, Roopa S. A Comparison of the Rate of Retraction with Low-level Laser Therapy and Conventional Retraction Technique. (2018). Contemp Clin Dent., **9**(2): 260-266.

Chen A. C., Arany P. R., Y.-Y. Huang et al. (2011), Low-level laser therapy activates NF-kB via generation of reactive oxygen species in mouse embryonic fibroblasts, PLoS One, **6**(7).

Deshpande P, Patil K, Mahima VG, Shivalinga BM, Suchetha M, Ranjan A. (2016). Low-level laser therapy for alleviation of pain from fixed orthodontic appliance therapy: a randomized controlled trial. Journal of Advanced Clinical and Research Insights., **3**(2):43-6.

Diravidamani K, Sivalingam SK, Agarwal V. (2012). Drugs influencing orthodontic tooth movement: An overall review. J Pharm Bioallied Sci. **4**(2): S299-303.

Doshi-Mehta G., Bhad-Patil W. A. (2012). Efficacy of low-intensity laser therapy in reducing treatment time and orthodontic pain: a clinical investigation. American Journal of Orthodontics and Dentofacial Orthopedics., **141**(3):289–297.

Fujita S, Yamaguchi M, Utsunomiya T, Yamamoto H, Kasai K. (2008). Low-energy laser stimulates tooth movement velocity via expression of RANK and RANKL. Orthodontics & craniofacial research., **11**(3):143-55.

Genc G, Kocadereli I, Tasar F, Kilinc K, El S, Sarkarati B, et al. (2013). Effect of low-level laser therapy (LLLT) on orthodontic tooth movement. Lasers Med Sci., **28**:41–7.

Greco M, Guida G, Perlino E, Marra E, Quagliariello E.(1989). Increase in RNA and protein synthesis by mitochondria irradiated with helium-neon laser. Biochemical and biophysical research communications. **163**(3):1428-34.

Harazaki M, Isshiki Y. Soft laser irradiation effects on pain reduction in orthodontic treatment. (1997). The Bulletin of Tokyo Dental College., **38**(4):291-5.

Hashimoto F., Y. Kobayashi, S. Mataki, K. Kobayashi, Y. Kato, and H. Sakai, (2001). Administration of osteocalcin accelerates orthodontic tooth movement induced by a closed coil spring in rats," European Journal of Orthodontics, **23** (5):535–545.

Heravi F., Moradi A., Ahrari F. (2014). The effect of low level laser therapy on the rate of tooth movement and pain perception during canine retraction. Oral Health and Dental Management.,**13**(2):183–188.

Kanzaki, H., Chiba, M., Shimizu, Y. & Mitani, H. (2002). Periodontal ligament cells under mechanical stress induce osteoclastogenesis by receptor activator of nuclear factor kappaB ligand up-regulation via prostaglandin E2 synthesis. J. Bone Miner. Res., **17**: 210–220.

Karu TI, Kolyakov SF. (2005). Exact action spectra for cellular responses relevant to phototherapy. Photomedicine and Laser Therapy., **23**(4):355-61.

Kau, C. H. et al. (2013). Photobiomodulation accelerates orthodontic alignment in the early phase of treatment. Prog. Orthod., **14**:1–9.

Kawasaki K, Shimizu N. (2000). Effects of low-energy laser irradiation on bone remodeling during experimental tooth movement in rats. Lasers Surg Med., **26**(3):282–91.

Li FJ, Zhang JY, Zeng XT, Guo Y. (2015). Low-level laser therapy for orthodontic pain: A systematic review. Lasers Med Sci., **30**:1789–803.

Limpanichkul W, Godfrey K, Srisuk N, Rattanayatikul C. (2006). Effects of low-level laser therapy on the rate of orthodontic tooth movement. Orthod Craniofac Res., **9**:38–43.

Mheissen, S., Khan, H. & Samawi, S. (2020). Is piezocision effective in accelerating orthodontic tooth movement: A systematic review and meta-analysis. PLoS ONE 15, e0231492.

Nimeri G., C. H. Kau, N. S. Abou-Kheir, and R. Corona. (2013). "Acceleration of tooth movement during orthodontic treatment–a frontier in orthodontics," Progress in Orthodontics, **14**(1): 42

Qamruddin I., Khan A. G., Asif F. M., et al. (2020). Pain perception and rate of canine retraction through self-ligating brackets and conventional elastomeric ligation system: a split mouth study. Pesquisa Brasileira em Odontopediatria eClínicaIntegrada., **20**: e5147

Ruan MJ, Chen G, Xu TM. (2018). Comparison of orthodontic tooth movement between adolescents and adults based on implant superimposition. PLoS One., **13**(5): e197281.

Turhani D, Scheriau M, Kapral D, Benesch T, Jonke E, Bantleon HP. (2006). Pain relief by single low-level laser irradiation in orthodontic patients undergoing fixed appliance therapy. Am J Orthod Dentofacial Orthop. ,**130**:371–7.

Yamasaki K, Miura F, Suda T. (1980). Prostaglandin as a mediator of bone resorption induced by experimental tooth movement in rats. Journal of dental research., **59**(10):1635-42.

Yi, J. et al. Effectiveness of adjunctive interventions for accelerating orthodontic tooth movement: A systematic review of systematic reviews. J. Oral Rehabil. **44**, 636–654 (2017).

Yoshida T, Yamaguchi M, Utsunomiya T, Kato M, Arai Y, Kaneda T, Yamamoto H, Kasai K. (2009). Low-energy laser irradiation accelerates the velocity of tooth movement via stimulation of the alveolar bone remodeling. Orthod Craniofac Res. ,**12**(4):289–98.

Youssef M, Ashkar S, Hamade E, Gutknecht N, Lampert F, Mir M. (2008). The effect of low-level laser therapy during orthodontic movement: A preliminary study. Lasers Med Sci. **23**:27–33.

Youssef M., Ashkar S., Hamade E., Gutknecht N., Lampert F., Mir M. (2008). The effect of low-level laser therapy during orthodontic movement: a preliminary study. Lasers in Medical Science., **23**(1):27–33.

Zahra SE, Elkasi AA, Eldin MS, Vandevska-Radunovic V. (2009). The effect of low level laser therapy (LLLT) on bone remodelling after median diastema closure: a one year and half follow-up study. orthodontic waves., **68** (3):116-22.

دراسة أولية لليزر الثنائي: (810،980) نانومتر في تسريع حركة الأسنان التقويمية

اية عدنان عاصي*[1,]، رواء احمد فارس[1]، بلسم سعدي عبد الحميد[2]، و سرمد صالح المالكي[3]

[1]معهد الليزر للدراسات العليا,جامعة بغداد,بغداد, العراق
[2]مدينة الامامين الكاظمين اللطبية,بغداد, العراق
[3]مركز الكرامة التخصصي لطب الاسنان,بغداد, العراق

*البريد الالكتروني للباحث:aya.adnan1202a@ilps.uobaghdad.edu.iq

الخلاصة: يشعر المرضى بقلق بالغ إزاء طول مدة علاج تقويم الأسنان. من الضروري إيجاد طريقة غير جراحية لتسريع حركة الأسنان الفسيولوجية. كان الهدف من هذه الدراسة هو تقييم فعالية العلاج بالليزر منخفض الشدة في تقصير الوقت وعدم الراحة في علاج تقويم الأسنان. **العمل التجريبي:** باستخدام دراسة الفم المنقسم لمقارنة حركة الأسنان بالعلاج التقليدي وحركة الأسنان التقويمية المسرَّعة بالليزر، تمت الإشارة إلى مريض يعاني من سوء إطباق من الدرجة الثانية -الدرجة الأولى لعلاج تقويم الأسنان بجهاز تقويم الأسنان الثابت مع قلع ثنائي لأسنان الضاحك العلوية الأولى وبُعد الجزء الأمامي لإغلاق المسافة المتكونة. بحث عن تصميم الفم المنقسم لمريض سيتم قلع ضواحك العلوية الأولى منه. لإجراء تحقيق تجريبي ، تم اختيار المريض عشوائياً وإعطاء إشعاع الجانب الأيمن باستخدام ليزر ثنائي الصمام (طول موجي 810،980 نانومتر، طاقة 100 ميلي واط). **النتائج:** تم قياس حركة الأسنان على مدى 15 أسبوعًا. تضمنت التفعيلات الثلاثة الأولى لتقويم الأسنان في جانب الدراسة العلاج بالليزر المجدول (الشهر الأول، العلاج بمساعدة الليزر في الأيام (0،3،7 و 14) ، الشهرين التاليين ، في الأيام (0 و14) من اليوم لتفعيل تقويم الأسنان، و3 أشهر أخرى من المتابعة فقط)؛ كان أعلى بشكل ملحوظ في جانب الدراسة منه في جانب التحكم ، كما تم قياسه سريريًا باستخدام الورنية الرقمية. لاحظنا أيضًا انخفاضًا كبيرًا في مستويات الألم بعد اختبار Visual Analog Scale. **الخلاصة:** قد يسرع LLLT سريريًا حركة الأسنان التقويمية بشكل كبير ويقلل بشكل كبير من الألم باستخدام إعدادات المستخدمة في هذا التحقيق.

IJL, Issue 2, Vol. 22, 2023 **Research Article**
https://doi.org/10.31900/ijl.v22i2.382

Intraoral Repair of Dental Ceramics Using Er,Cr:YSGG Laser: Review

Noor Bader Hassan, Basima Mohammed Ali Hussein*

Institute of Laser for Postgraduate Studies, University of Baghdad, Baghdad, Iraq.
**Email address of the Corresponding Author: basma.moh@ilps.uobaghdad.edu.iq*

Article history: Received 5 Feb 2023; Revised 6 July 2023; Accepted 24 July 2023; Published online 15 Dec 2023

Abstract

Introduction: All-ceramic crowns are widely used in prosthodontics and cosmetic dentistry due to their good esthetic and proper physical properties. Chipping of ceramic is one of the most common post-insertion complications, that can be fixed either extraoral or intraorally. The latter is time time-effective alternative, less traumatic, and low-cost. A newer objective method of laser is a surface modification of ceramics to increase surface roughness. The aim of this study is to provide a review of Er,Cr;YSGG (2960nm) in intraoral repair and shear bond strength (SBS). **Method:** A thorough search considering Google Scholar and PubMed published data and ten articles found who published between 2018 to 2022. **Results**:Because of the variation in the material composition of all ceramic crowns (feldspathic porcelain, zirconia, lithium dislocate, hybrid ceramics) different surface treatment methods are required for strong composite ceramic interphase. The effect of Er,Cr:YSGG on porcelain was minimal and lower than hydrofluoric acid, while for zirconia surface can be acceptable compared to no treatment. **Conclusion**: intraoral repair is an effective and cost-effective treatment that does not require multiple appointments. However, the success and durability of the restoration are dependent on technical and clinical experience and a superior understanding of material composition.

Keywords: Intraoral repair, dental ceramics, ceramic chipping, Er,Cr:YSGG laser and shear bond strength (SBS).

1. Introduction

With the newest improvements in the sciences of materials construction processes and techniques, the demand for more aesthetic restoration has increased. The exceptional aesthetic properties and biocompatibility of all ceramic restorations permit their widespread usage in restorative dentistry. (Sousa et al. 2022). All-ceramic restorations, such as aluminum-based porcelains, zirconium oxide ceramics, and leucite or lithium-disilicate-reinforced glass ceramics, can be regarded as an alternative treatment option to porcelain fused to metal restorations. Because it is the most stable and high-strength ceramic material,

zirconium dioxide offers superior mechanical qualities when compared to traditional ceramics. It has a flexural strength of 900 MPa and a fracture toughness of 9 MPa/m1/2. But for the ideal esthetic results the zirconium dioxide does not have the best optical properties that mimic the natural teeth, so the solution was to add a translucent layer of porcelain to permit the light transmission as the natural teeth. Owning to the physical properties of the porcelain it chips easily when exposed to masticatory forces which may extend to 160 ibf upper limit or in cases of occlusal discrepancy, or improper design and construction considering the of masticatory force. (Kimmich and Stappert 2013),(Sailer et al. 2007) (Poli O et al, 2021). According to a systematic literature review, chipping of the veneering ceramic is one of the most frequent technical complications occurring at a rate of 12.7% following a three-year observation period (Pjetursson et al. 2015). Chipping of ceramic can cause esthetic and functional concerns that require repair, small chipping of ceramic can be repaired intraorally with resin composite, which is economically effective, less traumatic to the abutment structure, and pulp, and can be performed with a single session. While some etensive fractures may require replacement or extraoral repair of the crown (Rekow et al. 2011),(Ghavam et al. 2017). Dental composite resin can be used for ceramic repair with intraoral ceramics repair kits. The chemical interaction at this interface is essential for a strong and successful resin-porcelain bond. Surface-roughening treatments on ceramic material are necessary to improve micro-mechanical retention. In these techniques, the silan group could provide onding sites between the substrate and repair material following the etching procedure (Duzyol, Sagsoz, et al. 2016).

In such a circumstance, a number of different treatments can be applied, such as Al_2O_3 particle sandblasting, acid etching as hydrofluoric acid, diamond disc grinding, Cojet system (surface air blasting with silica particles and laser treatment (Ji-Young et al 2015). The increase in use of chairside laser applications such as carbon dioxide (CO_2), neodymium-doped yttrium garnet (Nd:YAG), and erbium chromium: yttrium scandium gallium garnet (Er,Cr:YSGG) lasers. (de Paula Eduardo et al. 2012) (Emre Tokar et al, 2019; Farhad et al. 2012). Er, Cr:YSGG (2780 nm) is effective for removing both hard and soft dental tissues. Erbium lasers eliminate hard dental material by using thermal ablation. This method eliminated explosive tissue via water. This occurs as a result of the fast warming of subsurface water within the structure of the hard tissue, which absorbs infrared laser light. Warming these water particles[molecules] increases their subatomic vibrations, hence increasing the subsurface pressure. Finally, a "blast" of tissue removes tooth material or other hard substances, such as zirconia or ceramics.(Mirhashemi et al. 2019).
This study aim is to review the efficiency of Er,Cr:YSGG in intraoral repair of the ceramic fixed prostheses from 2013 to 2023.

2. Method

2.1. Data source and search strategy

The literature search was performed by using Google Scholar and PubMed for studies about the intra-oral repair that used the Er,Cr:YSGG laser as a surface modification for fracture of ceramics. The studies collected from January 2018 to December 2022, all review studies were excluded from this study.

In this review, keywords such as" Intraoral repair", "ceramic", "porcelain", "zirconia", "Er,Cr:YSGG", "shear bond strength", "SBS" were used to collect data and, only the studies published or translated to English were included. All are in a full-text format and have the Er,Cr:YSGG laser as a main study group or sub-group. Preparing for this review was started first by the selection of sequenced articles which was performed by reading the abstract first and then data collection and arranging from the full text.

3. Results

In order to comprehend the intraoral repair strategies utilized for the treatment of ceramic fractures or chipping, Google Scholar and PubMed searches yielded 6 papers that were included in this review. Table 1 provides a summary of the findings of the listed studies. In regard to Er,Cr:YSGG laser, several surface

treatment methods such as diamond bur, sand blasting, Cojet, hydrofluoric acid, Nd:YAG laser and air ablation were included in this study in order to modify ceramic surface roughness, increase bond strength, and raise shear bond strength. In addition to that, a variety of types of ceramics, such as zirconia, lithium disilicate, and feldspathic porcelain, were taken into consideration for this review. Ceramics that are based on glass and are sensitive to acid were included, as well as ceramics that are not based on glass and are resistant to acid. The repair systems that have been reviewed in this article were Cimara, Cimara zirconia repair, Ceramic repair N, Clearfil repair, and Bisco intraoral repair systems The efficiency of Er,Cr:YSGG during the ceramic intra-oral repair was investigated by considering the shear bond strength. Most of the reviewed studies compared the new method "laser "with the traditional methods like acid etching, bur grinding, Cojet, and sandblasting.

3.1 Intraoral repair without zirconia exposure

For restorations that have been chipped but do not reveal the zirconia layer, surface adhesion between porcelain and composite resin may be achieved either by macro-mechanical, micromechanical, or chemical methods(Borges, Sophr, et al. 2003). Most of the included studies compared SBS of composite the studies review is listed in Table 1. Abdulla and Hassan, 2022 evaluated two repair systems bond strength to porcelain surface and 50% porcelain and 50% zirconia, surface treated by Er,Cr:YSGG, sandblasting, and control group with no treatment. The veneering porcelain surface treated with air abrasion had the highest mean value (13.74 MPa), while the mixed surface's highest value was in the laser group with (11.24 MPa) Lowest value was in the control group. In a similar study made by Polat, Tokar et al. 2021 they reported the highest bond strength for 100% porcelain and mixed were in the control group with diamond bur with 16.76 MPa and 16.6 Mpa respectively. Baiomy et al. 2020 , had four groups for surface treatment air abrasion, Cojet, Er,Cr:YSGG laser, and mixed group (Cojet and laser), in their study they revealed that there was a significant difference between the groups(SBS) highest bond strength was in Cojet group and the lowest value was in the laser group. These results are in accordance with a study made by Sarac et al. 2013. Four studies in the review measured the shear bond strength of composite to laser-treated Lithium disilicate.

In a study by M. Chaharom et al. who modified the lithium disilicate surface with three different methods HF 9,5%, Nd:YAG , Er,Cr:YSGG and compared to the control group with no treatment. The HF group showed the highest shear bond strength, while the laser group was similar to the control group. (Chaharom, Azar et al. 2018). These results disagree with Alkhudairy(Alkhudhairy, Naseem et al. 2019), K.Barutcigit and O.Kirmali (Barutcigil and Kirmali 2020)who Obtained that the Er,Cr:YSGG was efficient in lithium disilicate surface modification and shear bond strength improvement.Vohra et al. assessed the SBS and color stability of lithium disilicate by using three pretreatment methods, HF mean bond strength was comparable to Er,Cr;YSGG. In addition to that the bond strength increases as the power and the duration of the laser increase. For hybrid ceramics, one study performed by Oz (Oz et al. 2019) in 2019, when a comparison of two types of hybrid ceramics treated with sandblasting, acid etching (hydrofluoric acid 8% and phosphoric acid 37%), Er,Cr:YSGG laser (2W and 3W) and control group with no treatment. The lowest SBS was in the control group followed by phosphoric acid, while the highest SBS was at 3W followed by 2W, sandblasting, and hydrofluoric acid.

3.2 Intra-oral repair with zirconia exposure

Most of the reviewed studies used different surface treatment methods to repair exposed zirconia surfaces in full ceramic crowns. Polat et al. compared the efficiency of Er,Cr: YSGG lasers with short and long pulse durations to various surface roughening techniques for repairing zirconia ceramics with different surface configurations. They found that SBS for sandblasting and Er,Cr: YSGG laser treatments exhibited no noticeable differences. (Polat et al. 2021) .These results agree with a study made by Kiramli et al. (Kirmali, Barutcigil, et al. 2015), additionally, a combination group of sandblasting and laser obtained the highest SBS, especially with the Er.Cr:YSGG laser.

Table 1: Reviewed studies.

Author/date	Type of ceramic	Manufacturer	Surface treatment	Study design	repair system	Result /conclusion
Mohammed Abdulla and Radhwan H /2022	- 100% zirconia -100%porcelain -zirconia with a veneering ceramic	-Zirconia (DD BioZ Wiso, Dental Direkt - Ceramic (VITA VM® 9 VITA Zahnfabrik	-Er,Cr,YSGG, 3W, frequency 10Hz, puls duration 140µ - Air- abraded sandblasting	In vitro	- Cimara repair system. - Ceramic repair N system	- air abrasion yields a greater SBS than Er,Cr:YSGG laser -Ceramic repair N system demonstrated significantly higher SBS values for all surface-treated substrates than the Cimara repair system.
Polat et al /2021.	-100% zirconia -100% porcelain - 50% porcelain 50% zirconia	- Vita VMK Master- ICE Zirkon Translucent, , Germany	-Dimond bur grinding -Sand blasting -Er.Cr;YSGG frequency 20Hz, power 1.5W. •Long wavelength pulse duration 200 µs •short wavelength pulse duration 140µs.	In vitro	Clearfil Repair, Noritake, Kuraray, Japan	Grinding is most appropriate for both zirconia and porcelain. -Sand blasting and short pulse duration shoed no significant difference
Baiomy et al 2020.	-100% porcelain -100% zirconia	-Ceramco PFZ Dentsply Sirona, USA -Bio ZX2 Zirconium, dental direkt , germany .	-Air abrasion -Cojet -Er.Cr;YSGG - Cojet +Er,Cr;YSGG 3W, pulse duration140µs and frequency 50 Hz.	In vitro	Bisco intraoral repair kit)	Cojet treatment had the highest SBS for porcelain and zirconia while laser lowest.
Barutcigit and O. Kirmali /2020.	-Lithium disilicate -IPS. E.max press, Ivoclar	----	-No treatment (control) -HF 9.5% -Phosphoric acid 37%- -Er.Cr; YSGG 1,2,3 W Frequency 1-Hz, for 20s.	In vitro	Single bond universal adhesive 3M ESPE	HF and 3W laser treatment obtained comparable results with appropriate bond strength
Vohra et al/2019.	Lithium disilicate	IPS. E, max Ivoclar	-HF 9.6% (control) - Er.Cr;YSGG 3.75W,15HZ, 2 min and 4min - Er.Cr.YSGG 7W, 25HZ 2min and 4min.	In vitro	-Ceramic primer, Mono-bond N Ivoclar -Bonding system (Adhese Universal; Ivoclar	Specimens lased (Er,Cr:YSGG) with 3.75 W power and 15 Hz frequency for 4 min showed bond strength comparable with that of HF acids.

Alkhudairy et al /2019.	Lithium disilicate	IPS. E.max press Ivoclar	-HF + silane -HF + ultrasonic bath silane -Self etch ceramic primer -Er,Cr:YSGG + Silane. 4.5W, frequency 30 Hz, 60s.	In Vitro	-Silane, Ivoclar	Er,Cr:YSGG laser can be used as a surface conditioner for lithium disilicate repair.
OZ / 2019.	Hybrid ceramics	-Lva ultimate 3M -Cerasmart, GC	-No treatment -Phosphoric acid 37% -Hydrofluoric acid 6% -Sandblasting -Er,Cr:YSGG 2W, 3W , 10 Hz, 20s.	In vitro	Single bond universal adhesive 3M ESPE	Er,Cr:YSGG can be an alternative etching method for hybrid ceramic repair
Tokar et al 2019.	-100% zirconia -100% porcelain	-ICE zirkon tranlucent -Vita VMK-master	-Diamond bur. -Er.Cr.YSGG 6W, frequency 20Hz. •Long wave length pulse duration 200 µs •short wavelength 140µs	In vitro	Ceramic repair N, Ivoclar	SBS for 100% zirconia was highest in short pulse duration laser while the diamond bur group provided the highest SBS for 100% porcelain.
Chahrom et.al/2018.	Lithium disilicate	PS E,max Ivoclar	-Control(no treatment) - HF 9,5% -Nd;YAG Power 4.5W,15Hz - Nd;YAG 6W,20Hz -Er.Cr:YSGG 1.5W and 6W for 1min.	In vitro	Porcelain silane, ultradent -primer and adhesive, self-etch silorane system, 3M	HF group showed the highest SBS while all laser groups did not improve the bond strength of composite to ceramic
Kirmali et al/2015.	Zirconia	- Noritake Co. -Nagoya	-Bur grinding (control) - CoJet sandblasting -Nd:YAG 1W, 20Hz, -Er.Cr.YSGG 1.5W -Sandblasting +Nd:YAG -sandblasting + Er;Cr:YSGG	In vitro	Cimara repair system	Combination of sandblasting and laser treatment is effective in zirconia repair, especially the Er,Cr;YSGG

Tokar et al. discovered that the SBS between zirconia and composite resin may be strengthened by using (Er,Cr: YSGG) laser surface treatments, shorter pulse laser with 140µs irradiation was more effective than longer pulse duration 200µs but it was not significant from the diamond bur grinding (control)group (Tokar et al. 2019). In a vitro study by Abdulla and Hassan that applied laser, air ablation and no treatment on the zirconia surface the highest SBS value was at air ablation followed by laser treatment.(Abdulla and Hasan 2022) .

4. Discussion

This review aimed to summarize the effect of Er.Cr:YSGG laser in intraoral repair of all ceramic crowns and how the surface treatment can reflect on SBS in years between 2018- December 2022.

Chipping of veneering porcelain is the most common complication of ceramic crowns and the incidence of chipping is higher in all ceramic crowns than in porcelain fused to metal crowns (Molin and Karlsson 2008). Multiple factors can be the cause of ceramic chipping such as lack of support, parafunctional occlusion, or intra-ceramic defects (Pjetursson, Sailer et al. 2015). The first step of the repair is to understand the classification of ceramic failure and the material, its extension an of the framework material. The ceramic fracture can either be static, adhesive, or cohesive, and the material of the chipped part can determine the method of repair (Aslam, Hassan, et al. 2018). Composite resin is the material of choice for repairing the fracture, for successful repair, a strong bond between the composite and the ceramic must be established. Mechanical and chemical methods are usually used. A variety of techniques are applied to increase ceramic roughness like HF, sandblasting, silica embedding, air abrasion with aluminum oxide particles, and laser there after silane application and resin bond before the repair composite(Swain 2009). In the current review adherence to glassy matrix ceramics is well-established by the application of HF, salinization, and adhesive resin, while the Er,Cr.YSGG did not improve repair bond strength alone. For lithium disilicate in one study, the laser had comparable results to HF.

Surface treatment processes such as acid etching and silane application have no effect on the adhesion between the zirconia framework and the composite material since zirconia is chemically inert and does not contain any silica(Qeblawi et al. 2010). To form a chemical bond with silane, Z-prime is used to create a chemical link with zirconia because it includes 10-MDP phosphate ester monomer, which chemically binds with the oxide layer of zirconia and increases bond strength.(El-Ashkar and Nabil 2022)

Other published research, however, has shown that the use of a laser does not improve the adhesion of composite resins and zirconia.

4. Conclusions

On the basis and the limitations of our review regarding the Er,Cr;YSGG laser effect on all ceramic repair the following conclusions could be drawn:

1- Er, Cr;YSGG laser does not improve the composite repair bond strength to porcelain in different powers, frequency, and energy. For lithium disilicate ceramic can be improved. The HF is the best surface treatment method for silica-based ceramics followed by silane and resin bonds.

2- The zirconia surface roughness was increased after laser treatment and even the shear bond strength compared to no treatment surface .

References

Abdulla, M. A. and R. H. Hasan (2022). "Shear Bond Strength of Two Repair Systems to Zirconia Ceramic by Different Surface Treatments." Journal of Lasers in Medical Sciences **13**: e31-e31.

Alkhudhairy, F., M. Naseem, Z. H. Ahmad, A. N. Alnooh and F. Vohra (2019)."Efficacy of phototherapy with different conventional surface treatments on adhesive quality of lithium disilicate ceramics." Photodiagnosis and Photodynamic Therapy **25**: 292-295.

Aslam, A., S. Hassan, M. Nayyer and B. Ahmed (2018)."Intraoral repair protocols for fractured metal-ceramic restorations-Literature review." South African Dental Journal **73**(1): 35-41.

Baiomy, A. A., J. F. Younis and A. H. Khalil (2020)."Shear bond strength of composite repair system to bilayered zirconia using different surface treatments (in vitro study)." Brazilian Dental Science **23**(1): 11.

Barutcigil, K. and O. Kirmali (2020). "The effect of different surface treatments on repair with composite resin of ceramic." Nigerian Journal of Clinical Practice **23**(3): 355-355.

Borges, G. A., A. M. Sophr, M. F. De Goes, L. C. Sobrinho and D. C. Chan (2003). "Effect of etching and airborne particle abrasion on the microstructure of different dental ceramics." The Journal of prosthetic dentistry **89**(5): 479-488.

Chaharom, M. E. E., F. P. Azar, N. Mohammadi and R. Nasiri (2018). "Effect of surface preparation with Nd: YAG and Er, Cr: YSGG lasers on the repair bond strength of lithium disilicate glass ceramic to a silorane-based composite resin." Journal of dental research, dental clinics, dental prospects **12**(1): 12.

de Paula Eduardo, C., M. S. Bello-Silva, S. G. Moretto, P. F. Cesar and P. M. de Freitas (2012). "Microtensile bond strength of composite resin to glass-infiltrated alumina composite conditioned with Er, Cr: YSGG laser." Lasers in medical science **27**(1): 7-14.

Duzyol, M., O. Sagsoz, N. Polat Sagsoz, N. Akgul and M. Yildiz (2016). "The effect of surface treatments on the bond strength between CAD/CAM blocks and composite resin." Journal of Prosthodontics **25**(6): 466-471.

El-Ashkar, A. S. F. and O. Nabil (2022)."Dealing with the Internal and External Surfaces of Zirconia Restorations; between Past and Present Trends. A Review of Literature." Acta Scientific Dental Sciences **6**(7).

Emre Tokar, Serdar Polat, and Caner Ozturk. "Repair bond strength of composite to Er,Cr:YSGG laser irradiated zirconia and porcelain surfaces". Biomed J. **42**(3): 193–199.

Farhad Sobouti, Sepideh Dadgar, Negareh Salehabadi, Aryousha Moallem Savasari. (2021). Diode laser chairside frenectomy in orthodontics: A case series. Clin Case Rep.;9:e04632.

Ghavam, M., M. Soleimanpour, S. S. Hashemikamangar, H. Ebrahimi and M. J. Kharazifard (2017). "Microshear bond strength of self-adhesive composite to ceramic after mechanical, chemical and laser surface treatments." Laser therapy **26**(4): 297-304.

Ji-Young Yoo, Hyung-In Yoon, Ji-Man Park, Eun-Jin Park. Porcelain repair - Influence of different systems and surface treatments on resin bond strength. (2015). J Adv Prosthodont,**7**:343-8

Kimmich, M. and C. F. Stappert (2013). "Intraoral treatment of veneering porcelain chipping of fixed dental restorations: a review and clinical application." The Journal of the American Dental Association **144**(1): 31-44.

Kirmali, O., Ç. Barutcigil, M. M. Ozarslan, K. Barutcigil and O. T. Harorlı (2015). "Repair bond strength of composite resin to sandblasted and laser irradiated Y-TZP ceramic surfaces." Scanning **37**(3): 186-192.

Mirhashemi, A. H., S. M. H. Hossaini, A. Etemadi, M. J. Kharazifard, A. Bahador and A. Soudi (2019). "Effect of Er: YAG and Er, Cr: YSGG lasers on ceramic bracket debonding from composite blocks." Frontiers in Dentistry **16** (2): 88.

Molin, M. K. and S. L. Karlsson (2008). "Five-Year Clinical Prospective Evaluation of Zirconia-BasedDenzir 3-Unit FPDs." International Journal of Prosthodontics **21**(3).

Poli O, Manzon L, Niglio T, Ettorre E, Vozza I. (2021). "Masticatory Force in Relation with Age in Subjects with Full Permanent Dentition: A Cross-Sectional Study". Healthcare (Basel). **9**(6):700.

Oz, F. D., S. Canatan and S. Bolay (2019). "Effects of surface treatments on the bond strength of composite resin to hybrid computer-assisted design/manufacturing blocks." Journal of adhesion science and technology **33**(9): 986-1000.

Pjetursson, B. E., I. Sailer, N. A. Makarov, M. Zwahlen and D. S. Thoma (2015). "All-ceramic or metal-ceramic tooth-supported fixed dental prostheses (FDPs)? A systematic review of the survival and complication rates. Part II: Multiple-unit FDPs." Dent Mater **31**(6): 624-639.

Polat, S., E. Tokar, N. V. Asar and O. Kirmali (2021). "Evaluation of Efficacy of Various Surface Conditioning Methods on the Repair Bond Strength of Composite to Different Fracture Types of Zirconia Ceramics." Scanning 2021.

Qeblawi, D. M., C. A. Muñoz, J. D. Brewer and E. A. Monaco Jr (2010). "The effect of zirconia surface treatment on flexural strength and shear bond strength to a resin cement." The Journal of prosthetic dentistry **103**(4): 210-220.

Rekow, E., N. Silva, P. Coelho, Y. Zhang, P. Guess and V. Thompson (2011). "Performance of dental ceramics: challenges for improvements." Journal of dental research **90**(8): 937-952.

Sailer, I., A. Fehér, F. Filser, L. J. Gauckler, H. Lüthy and C. H. F. Hämmerle (2007). "Five-year clinical results of zirconia frameworks for posterior fixed partial dentures." International Journal of Prosthodontics **20**(4).

Sarac, D., Y. S. Sarac, S. Külünk and A. Erkocak (2013). "Effect of various surface treatments on the bond strength of porcelain repair." International Journal of Periodontics & Restorative Dentistry **33**(4).

Sousa, N., C. Galvão, E. Almeida and A. F. Júnior (2022). "Factors that Influence the Clinical Longevity of Ceramic Unit Restoration: A Scoping Review." European Journal of Dental and Oral Health **3**(2): 24-29.

Swain, M. (2009). "Unstable cracking (chipping) of veneering porcelain on all-ceramic dental crowns and fixed partial dentures." Acta biomaterialia **5**(5): 1668-1677.

Tokar, E., S. Polat and C. Ozturk (2019). "Repair bond strength of composite to Er,Cr:YSGG laser irradiated zirconia and porcelain surfaces." Biomedical journal **42**(3): 193-199.

Vohra, F., N. Labban, A. Al-Hussaini, M. Al-Jarboua, R. Zawawi, A. Alrahlah and M. Naseem (2019). "Influence of Er; Cr: YSGG laser on shear bond strength and color stability of lithium disilicate ceramics: an in vitro study." Photobiomodulation, Photomedicine, and Laser Surgery **37**(8): 483-488.

استخدام ليزر Er:Cr;YSGG في اصلاح السيراميك داخل الفم: دراسة استطلاعية

نور بدر حسن ، باسمة محمد علي حسين*

معهد الليزر للدراسات العليا، جامعة بغداد، بغداد، العراق.

*البريد الالكتروني للباحث: basma.moh@ilps.uobaghdad.edu.iq

الخلاصة

مقدمة: تستخدم التيجان الخزفية على نطاق واسع في التعويضات الاصطناعية السنية في طب الاسنان نظرًا لخواصها الجمالية والفيزيائية المناسبة. يعد تكسر السيراميك أحد أكثر مضاعفات ما بعد تركيب التعويضات شيوعًا ، ويمكن إصلاحه إما خارج الفم أو داخل الفم, هذا الأخير يعد هو بديل أقل تكلفة وأقل تاثيرا على السن والتركيب وفعالة اكثرمن حيث الوقت. تتمثل إحدى طرق المعالجة بالليزر في معالجة لسطح السيراميك لزيادة خشونة السطح (Er,Cr,YSGG 2780 nm). الهدف من هذه الدراسة هو تقديم مراجعة لتاثير هذا النوع من الليزر في اصلاح السيراميك في السنوات وتاثيره في قوة الربط بين السيراميك والحشوه التجميلية . بحثنا في الطريقة Google, PubMed Scholar وتم العثور على 10 مقالات من سنه2013 الى 2023. **النتائج**: بسبب الاختلاف في تركيب المواد لجميع التيجان الخزفية (الخزف الفلدسباثي والزركونيا وثاني سيليكات الليثيوم والسيراميك الهجين) ، فإن طرق المعالجة السطحية مختلفه حسب نوع السيراميك . وجد ان تاثير الليزر على البورسلين كان اقل كفاءة من أجل زيادة قوة الربط .ولكن الليزر كان افضل تأثير بينما بالنسبة لسطح الزركونيا اة يمكن أن يكون مقبولاً مقارنة بعدم المعالجة .**خلاصة الدراسة:** الإصلاح داخل الفم علاج ناجح وفعال من حيث التكلفة وقلة المضاعفات ولا يتطلب عدة مواعيد. ومع ذلك ، فإن نجاح واستمرارية الترميم يعتمدان على الخبرة الفنية والسريرية والفهم الفائق لتركيب المواد.

IJL, Issue 2, Vol. 22, 2023 **Research Article**
https://doi.org/10.31900/ijl.v22i2.405

Silver Nanoflowers as an Interfacial Liquid-State Surface Enhanced Raman Spectroscopy (SERS) Sensor for Water Pollution

Zinah Salahuddin Shakir[1,2]*, Ayad Abdul Razzak Dhaigham[3], and Sameer Khudhur Yaseen[4]

[1] *Institute of Laser for Postgraduate Studies, University of Baghdad, Baghdad, Iraq.*
[2]*Department of Applied Sciences, University of Technology, Baghdad, Iraq.*
[3]*Directorate of Materials Research, Ministry of Science & Technology, Baghdad, Iraq.*
[4]*Department of Physics, College of Science for Women, University of Baghdad, Baghdad, Iraq.*

**Email address of the Corresponding Author: zena.salahaldeen1101a@ilps.uobaghdad.edu.iq*

Article history: Received 18 July 2023; Revised 2 Aug 2023; Accepted 14 Aug 2023; Published online 15 Dec 2023

Abstract: Water pollution has created a critical threat to the environment. A lot of research has been done recently to use surface-enhanced Raman spectroscopy (SERS) to detect multiple pollutants in water. This study aims to use Ag colloid nanoflowers as liquid SERS enhancer. Tri sodium phosphate (Na_3PO_4) was investigated as a pollutant using liquid SERS based on colloidal Ag nanoflowers. The chemical method was used to synthesize nanoflowers from silver ions. Atomic Force Microscope (AFM), Scanning Electron Microscope (SEM), and X-ray diffractometer (XRD) were employed to characterize the silver nanoflowers. This nanoflowers SERS action in detecting Na_3PO_4 was reported and analyzed concerning both shape and size using a 532 nm laser. We observed that the nanoflower's structure produced strong SERS signals. The increase in the SERS signal is related to the deposition of Na_3PO_4 molecules in the aggregated silver nanostructure in the solution. The concentration of Na_3PO_4 plays a main role in detection since the Raman signal becomes stronger as the concentration increases. The highest phosphate analytical enhancement factor obtained for SERS in colloidal nanoflowers was 1.7×10^3 at 0.7×10^{-6} M which was the lowest concentration.

Keywords: AgNFs, Hotspot, Raman spectroscopy, Tri Sodium phosphate, Surface Plasmon resonance.

1. Introduction

Water pollution, one of the world's challenges, results from fast industrialization and poses a severe environmental danger. Organic and inorganic contaminants, like organic dyes, heavy metals, pesticides, sulfides, and so on, harm the aquatic system [1-3]. One of these pollutants that are dangerous to human health is fertilizers tri-sodium phosphate, which we will address in this research, as it can cause permanent

damage to human kidneys, leading to death [4]. Raman spectroscopy is a method that employs the vibrational spectrum to detect chemical interactions in a molecule and also being sensitive to surrounding changes [5]. As a consequence, Raman spectroscopy is a valuable tool for chemical and physical study. The Raman spectrum offers information particular to a substance, allowing for molecular identification [6]. Furthermore, Raman spectroscopy necessitates a simple preparation of the sample [7]. Raman signals are typically weak, but they can be significantly increased by adsorbing molecules on a roughened surface of metal or metal nanoparticles. This technique is known as surface-enhanced Raman spectroscopy (SERS) [8]. SERS is considered an effective optical sensing process to detect various analytes. The SERS impact has been linked to an improvement in the effectiveness of Raman scattering for molecules that are present on or very close to the surface of specific metal nanostructures, particularly free-electron metals like gold, silver, and copper. As a result, chemically or physically adsorbed molecules on these metal nanostructures experience a considerable Raman signal increase. SERS is capable of detecting even a single molecule and achieving very large enhancement factors (more than 10^{10}) with appropriate metal nanostructures and measurement settings [2,9]. The most frequently accepted explanations for SERS are the electromagnetic mechanism (EM) and the chemical mechanism (CM) [10,11]. EM has been reported to be more significant than CM [12]. EM is primarily based on surface plasmon in a metal nanostructure [13, 14]. In the EM process, electromagnetic waves interact with plasmonic metal nanostructures which leads to amplifying the Raman signal [15,16]. SERS has evolved into a valuable instrument for the quantitative study of hazardous compounds, even at low levels in food and the environment. SERS substrates are metal nanostructures that increase the Raman spectral signature of molecules deposited on them. SERS substrates can be of two different natures: colloidal nanoparticles in solution or nanostructures deposited on a surface [17]. It is commonly assumed that the significant Raman signal increase in SERS results from electromagnetic motivation at 'hot spots' on the SERS substrate [9,18,19]. These 'hot spots' are often nanogaps between neighboring metal nanostructures or narrow areas surrounding metal nanostructure tips [18,19]. Because of the number of 'hot spots,' experimental research and theoretical calculations have revealed that complex silver nanostructures including dendritic, flower-like, and star-like nanostructures can give an extremely high increase in the electromagnetic field [20-21].

This study will focus on the flower-like silver nanostructure as a liquid SERS substrate to demonstrate the detection of tri-sodium phosphate as a pollutant in water. Several research teams have created flower-like silver nanostructures known as silver nanoflowers-AgNFs to be used as SERS substrates [2].

2. Experimental work

2.1. Materials and methods

Tri-sodium phosphate (Na_3PO_4), and silver nitrate ($AgNO_3$) were purchased from CDH, India, and ascorbic acid (AA, $C_6H_8O_6$) tri-sodium citrate di-hydrate (TSC $C_6H_5Na_3O_7{\cdot}2H_2O$), polyvinylpyrrolidone (PVP) were purchased from SABIC, KSA, De-ionized (DI) water

2.2. Synthesis of silver nanoflower

First, an ice water bath arrangement was prepared by placing a 50 mL beaker holding 20 mL of distilled water in a 250 mL beaker having ice cubes. This configuration was exposed to 400 rpm magnetic stirring. After 10 minutes, a 0.5 M aqueous solution of $AgNO_3$ (2 mL) was added to the water. For another 10 minutes, the solution was treated with 0.3 M PVP aqueous solution (2 mL). The solution was then treated with 0.25 M tri-sodium citrate di-hydrate (0.2 mL) at 10-minute intervals. After 10 minutes, 0.5 M of AA (2 mL) was poured into the previously stated solution while stirring constantly [2]. A dark grey solution was obtained. A scanning electron microscope (SEM) AxiaChemiSEM by Thermo Scientific, the Netherlands, and an atomic force microscope (AFM) Model TT-2 AFM workshop, USA, were used to examine the surface morphologies and nanoparticle size distributions of the prepared Ag nanoflower. An

X-ray diffractometer (XRD) was applied to measure the crystallographic information of the Ag nanoflower in the range from 10 to 80. An ultraviolet-visible (UV-Vis) spectrophotometer was utilized to investigate the absorption spectrum of Na_3PO_4.

2.3. Preparation of Samples for SERS Spectra

Four samples of Na_3PO_4 were prepared at concentrations ($0.7x10^{-3}$, $0.7x10^{-4}$, $0.7x10^{-5}$, and $0.7x10^{-6}$) M in the Ag nanoflower colloidal. In order to make a comparison, we prepared a sample with a concentration of $0.7x10^{-3}$ M of Na_3PO_4 in distilled water only. This bare sample will allow us to better understand the effects of the pollutant in question. SERS spectra samples were measured in a glass vial with the laser beam focused within. Raman scattering measurements were taken by using a Raman microscope (532 nm Preconfigured Raman Spectrometer System) by (Stellar Net, lnc. Florida, USA). Samples were stimulated by a 532 nm laser line generated by a laser with a power of 70 mW at the sample and an integration time of 9 ms. In all cases, the spectral resolution was adjusted to 2 cm^{-1}. SERS spectra were registered using a total acquisition time of 10s for each SERS spectrum and a single scan. All Raman measurements were taken in the spectral region (200 – 2000) cm^{-1}.

4. Results and Discussion

According to the SEM images in Fig.1, the size of silver nanoflower was approximately 400 nm. The nanoparticles were aggregated and formed hot spots which were thought to be the source of the substantial rise in signal strength required for single-molecule detection [22, 23].

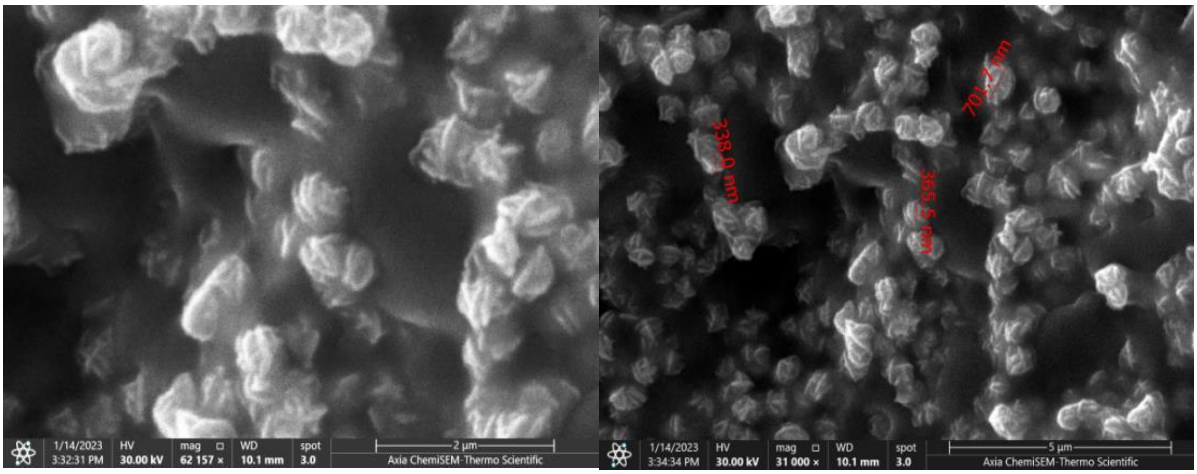

Fig.1: Scanning Electron microscope images for silver nanoflower.

According to the results obtained from the AFM, the average silver nanoparticle size was 13.61 nm; see Fig.2. The image shows that the nanosilver cluster formation in the topographic distribution is uniformly distributed. The test also revealed that the density of the silver nanoflower colloidal solution was 434 million particles/mm^2. The X-ray diffraction pattern of the AgNF structure exhibited unique diffraction peaks at (38.341°, 64.656°, and 77.625°), which are similar to pure silver crystal planes (111), (220), and (331); see Fig.3. These strong peaks in the planes suggest that the AgNFs are extremely crystalline. There were no further impurity peaks found, indicating that the samples were extremely pure. The crystalline size of Ag-NF was calculated from the Debye – Scherer equation and the average value of it was 43.6 nm [24].

$$L = \mathrm{k}\,\lambda / \beta\, cos\theta_B \quad (1)$$

Where L, k, λ, β, and θ_B are the crystalline size, the shape factor value which equals 0.9, the wavelength of the X-ray in nm, full width at half maximum (FWHM) in radians, and the diffraction angle in radians respectively. It is clear from Fig.4 that the absorption spectrum of Na_3PO_4 is approximately 200 nm which makes the 532 nm laser used in the Raman measurement suitable hence it is not very close to the absorbance area that produces fluorescence.

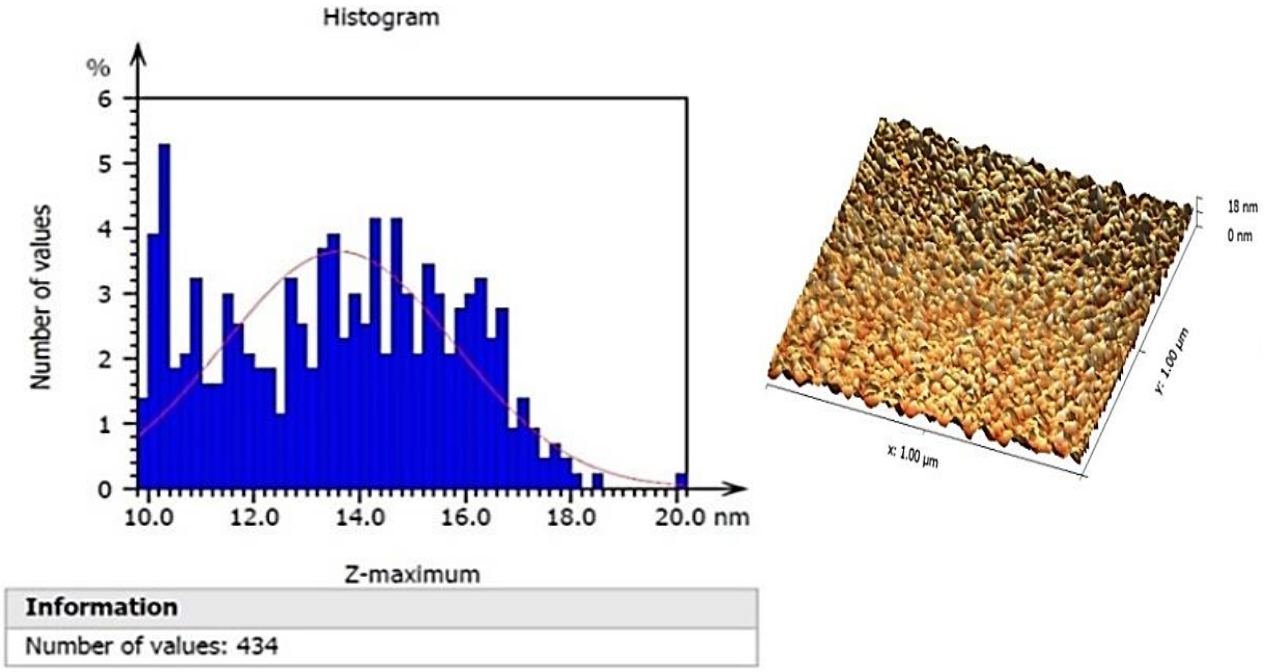

Fig.2: AFM analysis: Granularity cumulation distribution histogram and AFM- 3 dimensions image of silver nanoflower.

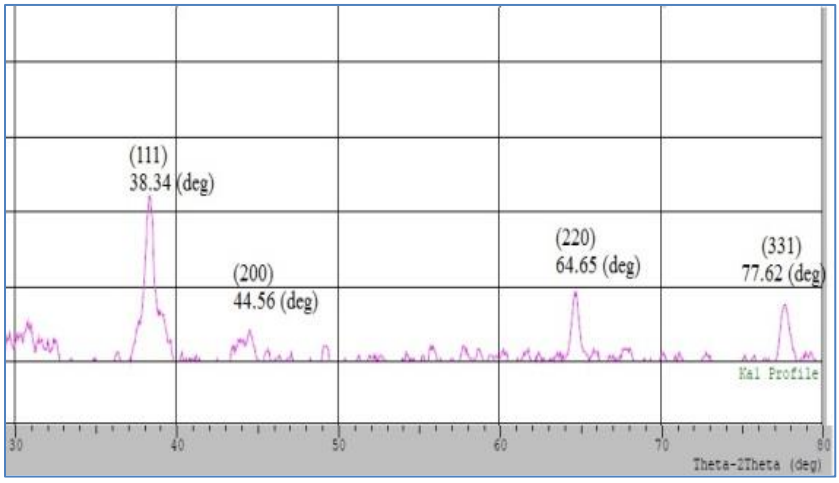

Fig. 3: Typical XRD pattern of AgNFs that have been synthesized.

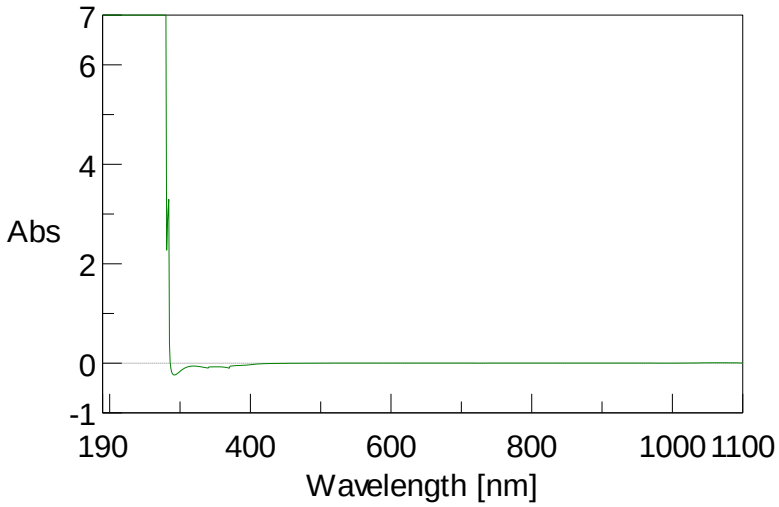

Fig.4: The absorption spectrum of Na_3PO_4.

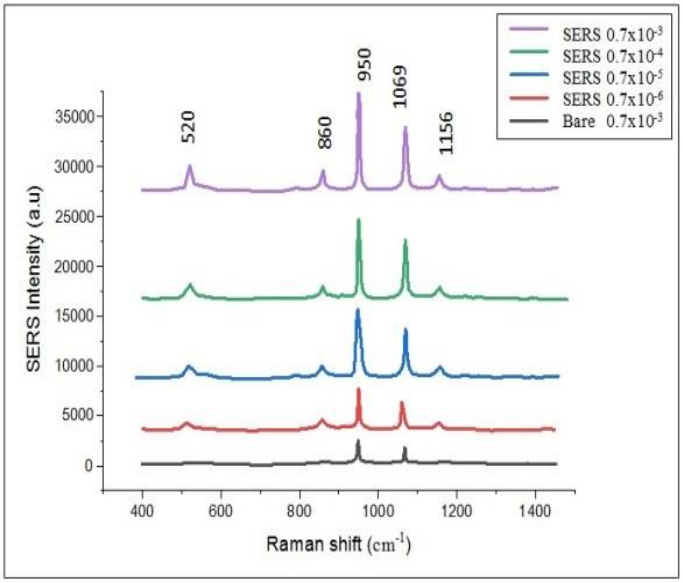

Fig.5: SERS intensity at the main peak (950 cm^{-1}) of Raman spectrum for Na_3PO_4 against the concentrations of Na_3PO_4 in Ag nanoflowers colloids.

The samples containing AgNFs showed greater Raman intensities at all Raman peaks than the bare ones; see Fig.5. It has been linked to the massive hotspots generated by the sharp edges and nanogaps of AgNFs structure when subjected to laser light [2,25]. A significant local electromagnetic field is generated around the surface of the nanostructure which can be up to 100 times stronger than the incident one [26], resulting in a significant amplification of the Raman signal. This strong local electromagnetic field resulted from the excitement of localized surface plasmon (LSP), which correlates with collective oscillations of the cloud of electrons within nanostructures, or electromagnetic interaction between nanostructures. [27,28]. Based on previous research, it has been found that the greatest increase in hot spot enhancement occurs when the distance between nanoparticles is reduced and the particle diameter is smaller, especially when the surface curvature increases [29].The electromagnetic coupling in the space between the nanoparticles is caused by

the nanoflowers aggregated in the solution. Due to the adjacency effect, the enhancement with the aggregated nanoparticles is more intense than for individual ones owing to forming electromagnetic "hot spot" in the nanoparticle gap, which produce a strong SERS signal from the molecules around it [17].

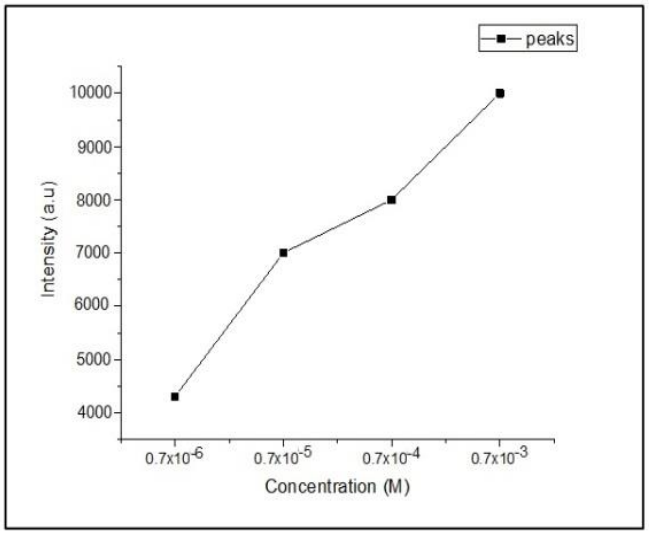

Fig.6: SERS intensity at the main peak (950 cm^{-1}) of Raman spectrum for Na_3PO_4 against the concentrations of Na_3PO_4 in Ag nanoflowers colloids.

The relationship between the concentrations of Na_3PO_4 and SERS intensity has shown in Fig.6. It is obvious that when Na_3PO_4 concentration increases, the SERS intensity increases too; this is attributed to the increase of the molecules of Na_3PO_4 attracted to AgNFs, Thus the Raman signal will be strengthened so the enhance Raman scattering strengthen which agree with articles [8, 30].

The analytical enhancement factor (AEF) was utilized to assess the actual SERS enhancement produced by EM and CM. AEF takes an analytical method for signal enhancement, combining signal strength with analyte concentration (C). This measure is useful when estimating the amount of analyte molecules present is difficult, especially for analytes that have no specific affinity for the plasmonic surfaces. AEF influences the vibration mode of a specific analyte in a normal Raman signal in the SERS technique, and it is directly proportional to the strength of the local electromagnetic field, referred to as a hot spot [31, 8].

$$AEF = \frac{I_{SERS} \times C_{NRS}}{C_{SERS} \times I_{NRS}} \quad (2)$$

Where; I_{NRS} and I_{SERS} refer to the counterpart intensities of normal Raman and SERS, respectively, C_{NRS} and C_{SERS} are the concentrations of the analyte in the normal Raman and SERS liquid substrates, respectively.

Based on our analysis, there appears to be a nonlinear increase of AEF at the highest peak (950 cm^{-1}) as the concentration of Na_3PO_4 decreases. This means that SERS is more efficient with lower concentrations. Overall, this information can help us better understand the effects of Na3PO4 on the samples we are analyzing; see Fig.7. Very low molecule concentrations improve the probability of specific molecule localization, which leads to better detection and hence raises the AEF by enhancing the SERS signal. At $0.7x10^{-6}$ M, the maximum phosphate AEF found for SERS in colloidal nanoflowers was $1.7x10^{3}$. The variation in (AEF) was mostly related to the variation in overlaps between SPR bands as a function of edge size and degree and the laser source. For ultrasensitive detection of phosphate molecules, the electromagnetic process of aggregated AgNF creates multiple hotspots from plentiful nanogaps on nanoflowers [29].

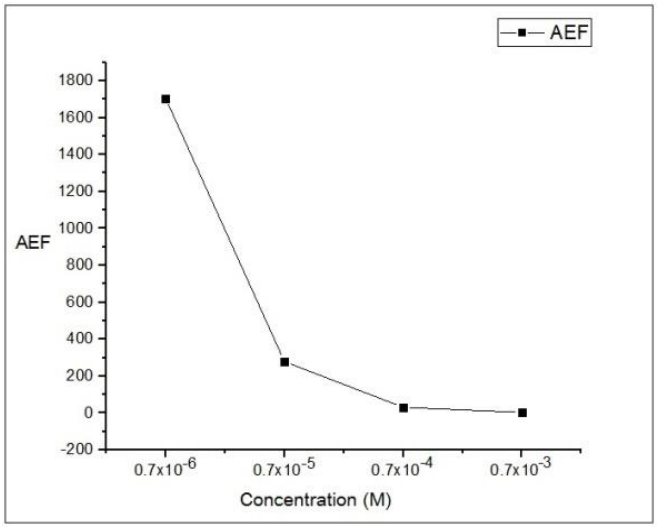

Fig.7: AEF at the main peak of SERS Raman intensity (950 $cm^{-1)}$ against the concentration of Na_3PO_4 in the Ag nanoflowers colloid.

5. Conclusions

Tri sodium phosphate was examined as a pollutant utilizing liquid SERS based on colloidal silver nanoflowers. The structure of nanoflowers with sharp edges and corners produced strong SERS signals. The aggregated nanoflowers in the colloidal have generated hot spots When Na_3PO_4 molecules are absorbed in solution and engage hot spots, the electromagnetic field increases, so the Raman signals are enhanced. The hot spot regions, which exist as minimal distances between nanoparticles, have an effect on the intense electromagnetic fields; SERS signals are greater within these microscopic hot spots. The AEF is directly proportional to the strength of the local electromagnetic field (a hot spot). The AEF influences the vibration mode of a specific analyte in a normal Raman signal in the SERS technique. As the Na_3PO_4 concentration increased, so did the Raman peaks. At $0.7x10^{-6}$ M (the lowest concentration), the highest phosphate AEF for SERS in colloidal nanoflowers was $1.7x10^3$ which means SERS is more efficient with lower concentrations.

References

[1] J. Wang, C. Qiu, X. Mu, H. Pang, X. Chen, D. Liu, "Ultrasensitive SERS detection of rhodamine 6G and p-nitrophenol based on electrochemically roughened nano-Au film", Talanta.,**210**,120631(2020).
[2] Nazar Riswana Barveen, Tzyy-Jiann Wang, Yu-Hsu Chang. "In-situ deposition of silver nanoparticles on silver nanoflowers for ultrasensitive and simultaneous SERS detection of organic pollutants". Microchemical Journal., **159**, 105520 (2020).
[3] Manh Cuong Nguyen, Truc Quynh Ngan Luong, Thi Thu Vu, Cao Tuan Anhc, Tran Cao Daoab. "Synthesis of wool roll-like silver nanoflowers in an ethanol/water mixture and their application to detect traces of the fungicide carbendazim by SERS technique".RSC Adv.,**12**,11583-11590 (2022).
[4] Wimalawansa SA, Wimalawansa SJ. Impact of changing agricultural practices on human health: Chronic kidney disease of multi-factorial origin in Sri Lanka. Wudpecker J Agric Res.,**3**(5),110-24 (2014).
[5] Durickovic, I. Using Raman spectroscopy for characterization of aqueous media and quantification o/f species in aqueous solution. In Applications of Molecular Spectroscopy to Current Research in the Chemical and Biological Sciences; Stauffer, M., Ed.; Intech: Rijeka, Croatia, 2016.
[6] Leonardo M. Moreira, Landulfo Silveira Jr., Fábio V. Santos, Juliana P. Lyon, Rick Rocha, Renato A. Zângaro, Antonio Balbin Villaverde, Marcos T. T. Pacheco, "Raman spectroscopy: A powerful technique for biochemical analysis and diagnosis", Journal of Spectroscopy",**22**, 19 (2008).

[7] Cyrankiewicz, M.; Wybranowski, T.; Kruszewski, S. "Study of SERS efficiency of metallic colloidal systems". In Journal of Physics: Conference Series, Proceedings of the XIII International Seminar on Physics and Chemistry of Solids, Ustron, Poland, IOP Publishing: Bristol, UK, **79**, 01203(2007).
[8] Hidayah AN, Triyono D, Herbani Y, Saleh R. "Liquid Surface-Enhanced Raman Spectroscopy (SERS) Sensor-Based Au-Ag Colloidal Nanoparticles for Easy and Rapid Detection of Deltamethrin Pesticide in Brewed Tea". Crystals, **12**(1), 24(2022).
[9] L. T. Q. Ngan, D. T. Cao, C. T. Anh, and L. V. Vu, "Trace detection of herbicides by SERS technique, using SERS-active substrates fabricated from different silver nanostructures deposited on silicon:.Int. J. Nanotechnol.,**12**, 358 (2015).
[10] Zhang Y, Mi X, Tan X, Xiang R. "Recent Progress on Liquid Biopsy Analysis using Surface-Enhanced Raman Spectroscopy". Theranostics, **9**(2):491-525 (2019).
[11] Fromm, D.P.; Sundaramurthy, A.; Kinkhabwala, A.; Schuck, P.J.; Kino, G.S.; Moerner, W.E. "Exploring the chemical enhancement for surface-enhanced Raman scattering with Au bowtie nanoantennas". J. Chem. Phys., **124**, 61101(2006).
[12] Davies, R.A.; Chong, N.S.; Ooi, B.G. "Chemical enhancement of the surface enhanced Raman scattering signals of anilines via their Ortho-substituents". Opt. Photonics J., **3**, 13–23(2013).
[13] Ding, S.Y.; You, E.M.; Tian, Z.Q.; Moskovits, M. "Electromagnetic theories of surface-enhanced Raman spectroscopy". Chem. Soc. Rev., **46**, 4042–4076 (2017).
[14] Wang, J.; Lin, W.; Cao, E.; Xu, X.; Liang,W.; Zhang, X. "Surface plasmon resonance sensors on Raman and fluorescence spectroscopy". Sensors, **17**, 2719 (2017).
[15] Ling, Y.; Zhuo, Y.; Huang, L.; Mao, D. "Using Ag-embedded TiO2 nanotubes array as recyclable SERS substrate". Appl. Surf. Sci., **388**, 169–173 (2016).
[16] Roguska, A.; Kudelski, A.; Pisarek, M.; Opara, M.; Janik-Czachor, M. "Surface-enhanced Raman scattering (SERS) activity of Ag, Au and Cu nanoclusters on TiO2-nanotubes/Ti substrate". Appl. Surf. Sci., **257**, 8182–8189 (2011).
[17] Raymond Gillibert, Jiao Qi Huang, Yang Zhang, Wei Ling Fu, Marc Lamy de la Chapelle. "Explosive detection by Surface Enhanced Raman Scattering". TrAC Trends in Analytical Chemistry. ,**105**,166-172 (2018).
[18] H. Tang, C. Zhu, G. Meng and N. Wu, J. "Review—Surface-Enhanced Raman Scattering Sensors for Food Safety and Environmental Monitoring".Electrochem. Soc., **165**, B3098 (2018).
[19] T. C. Dao, T. Q. N. Luong, T. A. Cao and N. M. Kieu. Fabrication of Silver Nanodendrites on Copper for Detecting Rhodamine 6G in Chili Powder Using Surface-enhanced Raman Spectroscopy. Adv. Nat. Sci. Nanosci. Nanotechnol.,**10**, 025012(2019).
[20] H. B. Li, P. Liu, Y. Liang, J. Xiao and G. W. Yang. "Super-SERS-active and highly effective antimicrobial Ag nanodendrites"Nanoscale., **4**, 5082(2012).
[21] Y. Han, S. Liu, M. Han, J. Bao, and Z. Dai, "Fabrication of Hierarchical Nanostructure of Silver via a Surfactant-Free Mixed Solvents Route". Cryst. Growth Des.,**9**, 3941–3947(2009).
[22] A. Garcia-Leis, J. V. Garcia-Ramos, and S. Sanchez-Cortes. "Silver Nanostars with High SERS Performance". J. Phys. Chem. C, **117**, 7791(2013).
[23] C. S. Kumar. "Raman spectroscopy for nanomaterials characterization. Springer Science & Business Media", 2012.
[24] Francisco M. L., Felipe M. M., Paulo H., Ana F., and Francisco N. "Nanostructured titanium dioxide average size from alternative analysis of Scherrer's Equation" revista. Matéria, **23**(1), (2018).
[25] J. Tong, Z. Xu, Y. Bian, Y. Niu, Y. Zhang, Z. Wang. "Flexible and smart fibers decorated with Ag nanoflowers for highly active surface-enhanced Raman scattering detection. J. Raman Spectrosc".,**50,** 1468–1476(2019).
[26] E. C. Le Ru, P. G. Etchegoin, "Quantifying SERS enhancements". MRS Bull ,**38**., 631- 640 (2013).
[27] N. Guillot, M. L. de la Chapelle, "The electromagnetic effect in surface enhanced Raman scattering: Enhancement optimization using precisely controlled nanostructures". J.Quant. Spectrosc. Radiat. Transf., **113,** 2321–2333(2012).
[28] M J. Grand, et al. "Role of localized surface plasmons in surface-enhanced Raman scattering of shape-controlled metallic particles in regular arrays". Phys Rev B, **72**,033407(2005).
[29] Robert C. Maher. "Raman Spectroscopy for Nanomaterials Characterization" SERS Hot Spots., Chapter 10, 215–260. (2012).
[30] McLellan JM, Siekkinen A, Chen J, Xia Y. "Comparison of the surface-enhanced Raman scattering on sharp and truncated silver Nanocubes". Chemical Physics Letters. ,**427**(1-3),122-6(2006).
[31] W. Plieth, H. Dietz, A. Anders, G. Sandmann, A. Meixner, M. Weber, H. Kneppe. "Electrochemical preparation of silver and gold nanoparticles: Characterization by confocal and surface enhanced Raman microscopy".Surface Science, **597**(1–3), 119-126 (2005).

محلول الفضة الغروي النانوي الزهري الشكل كمستشعر مطياف رامان المحسن للسطح للكشف عن ملوثات المياه

زينة صلاح الدين شاكر*[1،2] ، اياد عبد الرزاق ضيغم[3] ، سمير خضر ياسين [4]

[1]معهد الليزر للدراسات العليا، جامعة بغداد، بغداد، العراق.
[2]قسم العلوم التطبيقية، الجامعة التكنولوجية، بغداد، العراق.
[3]دائرة بحوث المواد، وزارة العلوم والتكنولوجيا بغداد، العراق
[4] قسم الفيزياء، كلية العلوم للبنات، جامعة بغداد، بغداد، العراق.

*البريد الالكتروني للباحث: zena.salahaldeen1101a@ilps.uobaghdad.edu.iq

الخلاصة : قد خلق تلوث المياه تهديدًا خطيرًا للبيئة ، وقد تم إجراء الكثير من الأبحاث مؤخرًا لاستخدام مطيافية رامان المعززة على السطح (SERS) لاكتشاف الملوثات المتعددة في المياه. تهدف هذه الدراسة إلى استخدام الفضة النانوية الغروية الزهرية ككاشف محسن السطح لتقنية رامان. تم فحص ثلاثي فوسفات الصوديوم (Na_3PO_4) باعتباره ملوثًا باستخدام SERS السائل بناءً على محلول الفضة الغرواني الزهري الشكل . تم استخدام الطريقة الكيميائية لتجميع الزهور النانوية من أيونات الفضة. تم استخدام مجهر القوة الذرية (AFM) ، والمجهر الماسح الإلكتروني (SEM) ، ومقياس حيود الأشعة السينية (XRD) لتوصيف الزهور النانوية الفضية. تم تقييم إجراء SERS هذا في الكشف عن الفوسفات وتحليله فيما يتعلق بكل من الشكل والحجم باستخدام ليزر 532 نانومتر. لاحظنا أن البنية الزهرية للفضة النانوية الغروية أنتجت إشارات SERS قوية. ترتبط الزيادة في إشارة SERS بترسيب جزيئات Na_3PO_4 في البنية النانوية للفضة المتكتلة في المحلول. يلعب تركيز الفوسفات دوراً رئيسياً في الكشف حيث تصبح إشارة رامان أقوى مع زيادة التركيز. كان أعلى معامل للتحسين التحليلي للفوسفات الذي تم الحصول عليه لـ SERS في زهور النانو الغروية 1.7×10^3 عند 0.7×10^{-6} مولار والذي كان أقل تركيز.

IJL, Issue 2, Vol. 22, 2023 **Research Article**
https://doi.org/10.31900/ijl.v22i2.392

In vitro Investigation the Antifungal and 940 nm Diode Laser Effects on Inhibition of Candida Albicans Isolated from Oral Cavity

Roaa Osamah Adnan*, Hussein Ali Jawad

Institute of Laser for Postgraduate Studies, University of Baghdad, Baghdad, Iraq
** Email address of the Corresponding Author: ruaa.usama1202a@ilps.uobaghdad.edu.iq*

Article history:Received 27 May 2023; Revised 26 July 2023; Accepted 15 Aug 2023; Published online 15 Dec 2023

Abstract

Background: Candida albicans is a prevalent commensal that can cause severe health problems in humans. One such condition that frequently returns after treatment is oral candidiasis. **Aim**: the goal of this research is to evaluate the efficiency of 940 nm as a fungicidal on the growth of Candida albicans in vitro. **Material and Methods:** In vitro samples (fungal swabs) were taken from the oral cavity of 75 patients suffering from oral thrush. Following the process of isolating and identifying Albicans. The samples are divided into four groups:(Group 1): Suspension of C. albicans was put in a solution of saline as a control group. (Group 2): Suspension of C. albicans that had been treated with nystatin. (Group 3): Suspension of C. albicans was irradiated by diode laser 940 nm at 1 W for 300 seconds in continuous mode. (Group 4): C. albicans suspension was irradiated by laser in a combination of nystatin. ANOVA, Dunnett t, and LSD tests were used to examine the data. A highly significant statistical variation in the count of C. Albicans before and after therapy. **Results:** The result of this study, finds that the reduction in the CFU/ml in group 4 (laser+nystatin) is highly significant and diode laser has a fungicidal effect on the growth of candida albicans. **Conclusion:** using a 940 nm diode laser (continuous mode) in a combination of antifungal (nystatin) acts as a fungicidal effect on Candida albicans.

Keywords: Candida Albicans, diode laser, 940 nm, Nystatin, oral thrush.

1. Introduction

Oral candidiasis is caused by a fungal infection called Candida albicans, which accounts for 60-70% of all cases (Hussain and Al-Drobie, 2022). Non-pathogenic Oral candidiasis could be caused by the yeast Candida albicans, which was a common member of the oral microbiota. (Al-Ali DA and Al Groosh D,2022). In persons with decreased cellular immunity, C. albicans could become active and cause oral infections (Williams et al,2012). Fungi have been discovered in dental root canals, dentin walls, and even periodontal pockets (Al-Maliky MA et al, 2022).

People who wore poorly fitting dentures were at risk for developing denture stomatitis, a chronic inflammatory condition of the palatal mucosa. (Karkosh ZS et al , 2018; Mawlood ZS and Naji GA,2020; Mohammed HA and Fatalla AA,2020).Even more concerning was the fact that 81% of AIDS patients receiving oral candidiasis treatment had Candida species that were resistant to antifungal drugs like fluconazole. (Johnson EM et al,1995). Between one-third and two-thirds of those who wore full dentures suffer from this problem. (Jainkittivong A et al,2010). Treating fungal infections, particularly systemic ones, is notoriously challenging due to therapeutic limitations and the emergence of drug-resistant strains. These findings highlight the importance of continuing to investigate and develop innovative therapies for fungal illnesses. (Chabrier et al,2008; Cowen LE et al,2009; Coleman JJ et al, 2010). Denture stomatitis is difficult to treat due to the multifaceted complexity of the disease's source. Traditional treatments include things like better dental care, antiseptic mouthwash, denture removal and soaking in disinfectant solution at night, and the replacement of ill-fitting dentures. The antifungal drug nystatin is effective in treating denture stomatitis. (Cueto et al,2013).

Nystatin is a Polyenes family member, and it functions by binding to ergosterol (a part of the fungal cell wall). Furthermore, it forms a complex with cholesterol in the cytoplasmic membrane of the host cell. Nystatin has an association with a number of unpleasant side effects, including diarrhea, stomach discomfort, tachycardia, bronchospasm, face swelling, muscular stiffness, Itching, burning, and rashes; Stevens-Johnson syndrome (Hammond SI.,1977). Using nystatin for an extended period of time not only requires the patient's cooperation but also raises the possibility that the fungus Candida albicans will develop resistance to the drug(Janeth et al.,2019). Furthermore, the drug is quite expensive (Zomorodian K et al,2011; Orlandini et al,2020). Low-level laser (LLL) is a type of laser that has non-thermal effects on biological systems (Lin et al,2010) and is used in biological systems to promote tissue regeneration and minimize inflammation (Huang et al,2011). The optical window for low-level laser treatment is between 600 and 1100 nanometers (nm), resulting in deeper tissue penetration and a larger cell-light response (Raghavendra,2005). The 940 nm diode laser is often used in dental offices because it is small, easy to get, cheap, and can be used for many different things in oral medicine.This source's radiation has an effect on the biofilm and destroys it (Mustafa and Salah,2020).

The aim of this research was to assess the efficacy of a 940 nm laser with a 1 W power output and a 300 s duration in inhibition of C. Albicans colonies.

2. Materials and methods

2.1 Samples collection and preparation

The University of Baghdad's Basic Science and Microbiology Department provided a Candida albicans strain isolated from the oral cavity of a patient suffering from oral thrush in order to test the antifungal activity. This strain was grown in a 48-hour incubation at 37^0C by plating it on Sabouraud Dextrose Agar. The suspension was diluted in an optical density 0.5 McFarland standard solution. The amount of C. albicans that was prepared was 10^4 viable cells/m. The suspension (10^4 cell/ml) was transferred to a 96-well microplate (0.1 ml in each well) using a sampler. Every antifungal activity test was carried out inside the laminar flow hood, at room temperature, in complete darkness, and under sterile circumstances.

2.2 Groups

Four groups were investigated on different microtiter plates:

Group 1: C. albicans suspended in saline solution served as a control.
Group 2: a suspension of C. albicans that has been treated with (0.1ml) of nystatin solution (100.000 Units/ml).
Group 3: C. albicans, irradiated by (940 nm diode laser) only.

Group 4: C. albicans irradiated by (940 nm diode laser) in a combination of(0.1ml) nystatin.

2.3 Laser Irradiation

The laser source in use is a 1 W continuous mode diode laser with a wavelength of 940 nm. Irradiation was performed at a 90-degree incidence angle with the laser beam's constantly pointing in a direction perpendicular to the wells' entrance, as in Fig.1

Fig.1: Irradiation procedure**.**

2.4 Antifungal activity test

A 0.1 ml of a diluted fungal culture containing $1*10^4$ CFU/ml was administered to group 2 along with 0.1 ml of nystatin. Following that, (0.1 ml) was seeded on Sabouraud dextrose agar. The dishes had been incubated for 48 hours at 37°C. The number of total colonies of Candida albicans (colony forming units CFU/mL) was used to analyze the plates. Using the Swanson, Petran, and Hanlin approach, a sample of colonies between 30 and 300 colonies was chosen for counting. (Swanson et al,2001).

3. Statistical analysis

In order to compare the means of different groups, the gathered data were put through an ANOVA is a one-way analysis of variance. The data was summarised using the mean and standard deviation (SD) and statistical significance was assessed by comparing means and testing for differences using a p-value threshold of 0.05. Multiple Comparisons by Dunnett t-tests were used in order to compare between tested groups and control. SPSS was used for all the statistical analyses (v 20).

4. Results

After isolation and identification of C.albicans, radiated by laser as adjacent or assistant to nystatin for biomodulation process, the result was sent to statical analysis. Table 1 demonstrated significant differences between tested means. Table 1 demonstrated significant differences between tested means. The letters A, B, C denoted the degrees of significance, with the most significant beginning with (A) G4(Laser+nystatin)and decreasing with the (C) last (laser alone) .To quantify the significant differences between tested means, the LSD test was performed . Table 2 shows the difference in the statical analysis between groups, compare the colony-forming unit of Candida albicans in G1(control) with other groups, it's the highest then laser alone G3 and the lowest one is the G4 (laser + nystatin). The test used in Table 2 is the Dunnett Test which compares the means of two sets of data to determine whether or not there is statistical significance between them.

Table 1. Differences between several groups.

940 nm Laser 1 watt 5 minutes	CONTROL	AF	LASER	L+AF	*P value*
N	5	5	5	5	
Mean × 10^4 CFU/mL	372.60	B 69.20	C 90.80	A 34.40	
Median	372.00	70.00	91.00	35.00	0.01 SIG
Std. Error of Mean	1.08	1.02	0.86	1.21	
Std. Deviation	2.41	2.28	1.92	2.70	
Minimum	370.00	66.00	88.00	30.00	
Maximum	376.00	72.00	93.00	37.00	

AF=antifungal

L+AF=Laser + antifungal

Table 2. Descriptive data comparing the CFU/ml of *Candida albicans* in different tested means.

Multiple Comparisons/ 940 nm Laser 1 watt 5 minute

Dependent Variable: CFU Dunnett t (2-sided)

GROUPS	(J) GROUPS	Mean Difference (I-J)	Std. Error	Sig.	95% Confidence Interval	
					Lower Bound	Upper Bound
AF	CONTROL	303.40	1.45052	0.000	307.2454	299.5546
LASER	CONTROL	281.80	1.45052	0.000	285.6454	277.9546
L+AF	CONTROL	338.20	1.45052	0.000	342.0454	334.3546

AF=antifungal

L=Laser

L+AF=Laser +antifungal

* The mean difference is significant at the 0.05 level.

Table 3. Time's effect on the CFU/mL.

940 nm Laser 1 watt	CONTROL	100 SEC	150 SEC	200 SEC	250 SEC	300 SEC	P VALUE
N	5	5	5	5	5	5	
Mean × 10^4 CFU/mL	372.60	E 323.40	D 295.60	C 254.60	B 187.80	A 90.80	
Median	372.00	324.00	295.00	255.00	188.00	91.00	
Std. Error of Mean	1.08	1.08	0.68	0.51	0.86	0.86	0.001 SIG
Std. Deviation	2.41	2.41	1.52	1.14	1.92	1.92	
Minimum	370.00	320.00	294.00	253.00	185.00	88.00	
Maximum	376.00	326.00	298.00	256.00	190.00	93.00	

Table 3 exhibited a statistically significant difference between different groups by studying the effect of time on the CFU, showed the significant difference in (300 s) and the lowest one in (100 s). Fig 1. Showed the percentage of mean values of CFU of Candida albicans, in G1(control) is a very highest percentage, then the Group of lasers alone(G3), then the percentage of (G2) Group of nystatin alone and the lowest percentage is the Group of (laser+nystatin) G4.

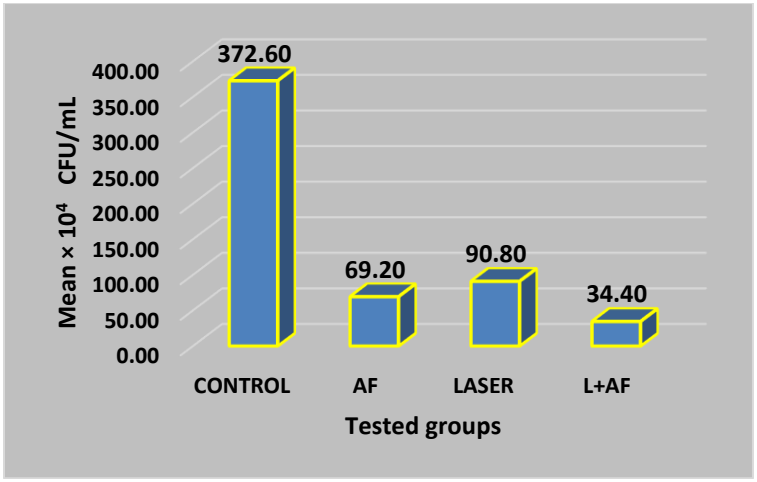

Fig.1: Average of colony-forming unit percentage between tested groups**.**

5. Discussion

Although light's effects have been studied for quite some time, its application as an antifungal agent is more recent.(Mt L et al,2004; Gutknecht N etal ,2000). Many pathogenic microbes have become resistant to conventional antimicrobials, prompting researchers to investigate this phenomenon. The process of acquiring new knowledge by any number of methods, some of which may be therapeutic in nature, is often referred to as "therapeutic." (Tardivo JP et. al,2005; Donnelly RF et. al,2008; Gonzales FP and Maisch T,2012; Oliveira et. al,2014; Bota C and Căruntu B,2015; Meimandi M et al 2017).

The term "therapeutic" refers to the process of obtaining new knowledge through a variety of approaches, including therapeutic techniques. The size of the microbe, the presence of the nucleus, and the

cell wall all contribute to the distinct properties of a fungal cell, emphasising the need to select the appropriate wavelength, power, and time. Group 4 (laser with nystatin) had considerably higher mean values of percentage of CFU compared to the other groups (Table 1). Table 3 exhibited statistically significant changes in CFU with increasing exposure duration, this might be related to the laser's direct action on the cytoplasmic membrane. According to other studies, this one demonstrated that diode laser treatment decreased candida albicans CFU with time. (Mahdi RA and Mohammed AA,2010; Anwer AG.,2005).

In our pilot study, A general mechanism can be developed to explain this phenomenon, one that can account for promoting cell culture activities with visible and infrared lasers at low laser doses, as well as the destructive action of these same lasers at large dosages. In the mitochondria, laser irradiation may result in the creation of a transmembrane electrochemical proton gradient. This increases ATP generation, which activates the Ca^{2+} pump, which depletes the Ca^{2+} concentration gradients of the surrounding media compared to the cytoplasm. This stimulus increases Ca^{2+} entry into cells through the Ca^{2+} ion channels in the plasma membraneMore Ca^{2+} is released from mitochondria via an antiport mechanism when enough irradiation is applied, as a result of the proton motive force (pmf) caused by the proton gradient. Together with other variables regulated by pmf, the increased cytoplasmic calcium induces mitosis and boosts cell proliferation. (Anwer AG.,2005).

Too much Ca^{2+} is released at high laser dosages. Ca^{2+}- ATPase becomes hyperactive as a result, depleting the cell's ATP supply. Certain wavelengths of light can also activate some of the intrinsic components of cells. This allows for the modification of both individual biochemical events and the metabolic activity of entire cells. It is thought that low-power laser effects depend on this kind of reaction. The results of this investigation agreed well with those of previous studies. Mitochondria are vulnerable to exposure to monochrome visible and near-infrared light, as shown by a number of different lines of evidence. (Anwer AG.,2005).

6. Conclusion:

A 940 nm diode laser (continuous mode, 1 W, 300 s) was found to be effective in decreasing the quantity of Candida albicans in an in vitro investigation, especially when used in conjunction with nystatin.

References

Al-Ali DA, Al Groosh D. (2022). “The influence of fixed orthodontic retainer on oral microbiota”. International Journal of Health Sciences. (II):2214-23.

Al-Maliky MA, Zardawi FM, Meister J, Frentzen M, Al-Karadaghi TS. (2022).“Transmission of 940 nm diode laser to the radicular area during its application as root canal disinfectant”. Australian Endodontic Journal. **48**(1):65-71.

Anwer AG. (2005). “Stimulation of Phagocytic Activity of Human Polymorphonuclear Leukocytes in Vitro Using 10 mW He-Ne Laser”. Iraqi Journal of Laser., **4**(B):23-7.

Bota C, Căruntu B. (2015).“Approximate analytical solutions of the fractional-order brusselator system using the polynomial least squares method”. Advances in Mathematical Physics.,**2015:**5.

Chabrier-Roselló Y, Foster TH, Mitra S, Haidaris CG. (2008). “Respiratory deficiency enhances the sensitivity of the pathogenic fungus Candida to photodynamic treatment”. Photochemistry and photobiology.,**84**(5):1141-8.

Coleman JJ, Okoli I, Tegos GP, Holson EB, Wagner FF, Hamblin MR, Mylonakis E. (2010).“Characterization of plant-derived saponin natural products against Candida albicans”. ACS chemical biology.;**5**(3):321-32.

Cowen LE, Singh SD, Köhler JR, Collins C, Zaas AK, Schell WA, Aziz H, Mylonakis E, Perfect JR, Whitesell L, Lindquist S. (2009).“Harnessing Hsp90 function as a powerful, broadly effective therapeutic strategy for fungal infectious disease”. Proceedings of the National Academy of Sciences.;**106**(8):2818-23.

Cueto A, Martínez R, Niklander S, Deichler J, Barraza A, Esguep A. (2013).“Prevalence of oral mucosal lesions in an elderly population in the city of Valparaiso”, Chile.Gerodontology. **30**(3):201-6.
Donnelly RF, McCarron PA, Tunney MM. (2008). “Antifungal photodynamic therapy. Microbiological research”., **163**(1):1-2.

Gonzales FP, Maisch T.(2012).“Photodynamic inactivation for controlling Candida albicans infections”. Fungal biology.,**116**(1):1-0.

Gutknecht N, Al-Karadaghi TS, Al-Maliky MA, Conrads G, Franzen R. (2016). “The bactericidal effect of 2780 and 940 nm laser irradiation on Enterococcus faecalis in bovine root dentin slices of different thicknesses”. Photomedicine and laser surgery., **34**(1):11-6

Gutknecht N, Conrads G, Apel C, Schubert C, Lampert F. (2000).“Effect of diode laser radiation in root canal wall dentine: a microbiological study”. InLasers in Dentistry VI **3910**: 124-127.

Hammond S M. (1977).” Biological activity of polyene antibiotics”. Progress in medicinal chemistry. **14**:105-79.

Huang YY, Sharma SK, Carroll J, Hamblin MR. (2011).“Biphasic dose response in low level light therapy–an update”. Dose-response.,9(4):602-18.

Hussain HS, Al-Drobie BF. (2022). “Clinicopathological assessment of chronic hyperplastic candidasis”. Journal of Baghdad College of Dentistry., **34**(4):28-33.

Jainkittivong A, Aneksuk V, Langlais RP.(2010).“Oral mucosal lesions in denture wearers”.Gerodontology., **27**(1):26-32.

Janeth Rimachi Hidalgo K, Cabrini Carmello J, Carolina Jordão C, Aboud Barbugli P, de Sousa Costa CA, Garcia de Oliveira Mima E, Pavarina AC. (2019). “Antimicrobial photodynamic therapy in combination with nystatin in the treatment of experimental oral candidiasis induced by Candida albicans resistant to fluconazole”. Pharmaceuticals., **12**(3):140.

Johnson EM, Warnock DW, Luker J, Porter SR, Scully C. (1995). “Emergence of azole drug resistance in Candida species from HIV-infected patients receivingprolonged fluconazole therapy for oral candidosis”. Journal of Antimicrobial Chemotherapy.,**35**(1):103-14.

Karkosh ZS, Hussein BM, AL-Wattar WM. (2018).“Effect of phosphoric containing and varnish-coated groups on Candida albicans adhesion and porosity of heat cure acrylic denture base material”. Biomedical and Pharmacology Journal.,**11**(1):179-85.

Lin F, Josephs SF, Alexandrescu DT, Ramos F, Bogin V, Gammill V, Dasanu CA, Necochea-Campion D, Patel AN, Carrier E, Koos DR.(2010).“Lasers, stem cells, and COPD”. Journal of translational medicine.,**8**(1):1-0.

Mahdi RA, Mohammed AA. (2010).“Photodynamic inactivation of candida albicans sensitized by malachite green”. Iraqi J Laser. **9**(2):31-6.

Mawlood ZS, Naji GA. (2020). “Bergamot essential oil effect against candida albicans activity on heat cure acrylic denture base”. Indian Journal of Forensic Medicine & Toxicology.,**14**(2):703-8.

Meimandi M, Ardakani MR, Nejad AE, Yousefnejad P, Saebi K, Tayeed MH. (2017). “The effect of photodynamic therapy in the treatment of chronic periodontitis: A review of literature”. Journal of lasers in medical sciences.;**8**(Suppl 1):S7.

Mohammed HA, Fatalla AA. (2020). “The effectiveness of chitosan nano-particles addition into soft denture lining material on Candida albicans adherence. Pak J Med Health Sci.;**14**:3.
Mustafa M Buraihi and Salah A Alkurtas. (2020). “The Photothermal Effect of 940nm Diode Laser on Enterococcus Faecalis Biofilm in Infected Root Canal”. Journal of Research in Medical and Dental Science., **8** (7): 480-486.

Mt L, PS B, Walsh LJ. “Photo-activated disinfection of the root canal: a new role for lasers in endodontics”. Aust Endod J. **30**(3):93-8.

Oliveira BP, Lins CC, Diniz FA, Melo LL, Castro CM.(2014).“In Vitro antimicrobial photoinactivation with methylene blue in different microorganisms. Brazilian Journal of Oral Sciences., **13**:53-7.

Orlandini, Renata Klemp, Davi Ariel Nobuo Bepu, Maria da Conceição Pereira Saraiva, Valdes Roberto Bollela, Ana Carolina Fragoso Motta, and Alan Grupioni Lourenco. (2020). "Are Candida albicans isolates from the oral cavity of HIV-infected patients more virulent than from non-HIV-infected patients? Systematic review and meta-analysis." Microbial Pathogenesis **149**: 104477.

Raghavendra S, Wood MC, Taylor TD. (2005). "Early wound healing around endosseous implants: a review of the literature". International Journal of Oral & Maxillofacial Implants., **20**(3): 425-31.

Swanson KM, Petran RL, Hanlin JH. (2001). "Culture methods for enumeration of microorganisms". Compendium of methods for the microbiological examination of foods.,**4**:53-62.

Tardivo JP, Del Giglio A, De Oliveira CS, Gabrielli DS, Junqueira HC, Tada DB, Severino D, de Fátima Turchiello R, Baptista MS. (2005). "Methylene blue in photodynamic therapy: From basic mechanisms to clinical applications". Photodiagnosis and photodynamic therapy.,**2**(3):175-91.

Williams D, Silva SC, Malic S, Kuriyama T, Lewis MA. (2012)."Candida biofilms and oral candidosis: treatment and prevention"., **55**(1):250–265.

Zomorodian K, Rahimi MJ, Pakshir K, Motamedi M, Ghiasi MR, Rezashah H. (2011). "Determination of antifungal susceptibility patterns among the clinical isolates of Candida species". Journal of global infectious diseases., **3**(4):357.

دراسه تاثير ليزرالدايود (940 نانومتر) و المضادات في تثبيط فطريات المبيضات البيض المعزوله من تجويف الفم في المختبر

رؤى اسامة عدنان* , حسين علي جواد

معهد الليزر للدراسات العليا، جامعة بغداد، بغداد، العراق

*البريد الالكتروني للباحث: ruaa.usama1202a@ilps.uobaghdad.edu.iq

الخلاصة

الخلفيه: المبيضات البيض هي نوع سائد يمكن أن يسبب مشاكل صحية خطيرة لدى البشر. أحد هذه الحالات التي تظهر بشكل متكرر بعد العلاج هو داء المبيضات الفموي.الهدف: الهدف من هذا البحث هو تقييم فعالية ليزر 940 نانومتر كمبيد فعال على نمو المبيضات البيض في المختبر.**المواد والطرق:** تم أخذ عينات (مسحات) من تجويف الفم لـ 75 مريضاً يعانون من مرض القلاع الفموي.بعد عملية العزل والتعرف على فطريات المبيضات البيض. العينات تقسم إلى اربع مجموعات: (المجموعة1): تعليق المبيضات البيض بوضعها بمحلول ملحي كمجموعة تحكم. (المجموعة2): تعليق المبيضات البيض وعلاجها بمحلول النيستاتين. (المجموعة 3): تم تشعيع معلق المبيضات البيض بواسطة ليزر الديود 940 نانومتر عند 1 وات لمدة 300 ثانية في الوضع المستمر. (المجموعة 4): تم تشعيع معلق المبيضات البيض بواسطة الليزر مع محلول النيستاتين.تم استخدام اختبارات الاحصاء لفحص البيانات. لوحظ فروقات ذات دلالة إحصائية عالية في عدد المبيضات قبل وبعد العلاج. **النتائج:** بعد التحليل الإحصائي وجد انه انخفاض ملحوظ في عدد المبيضات البيض في المجموعه 4 مع مضاد للفطريات (محلول النيستاتين) وايضا ان ليزر الدايود يعمل كمطهر فعال ومثبط للمبيضات البيض. **الخلاصة** : استخدام ليزر الدايود 940 نانومتر (الوضع المستمر) مع مزيج من مضاد الفطريات (nystatin) بمثابة مبيد فعال على المبيضات البيض.

IJL, Issue 2, Vol. 22, 2023 **Research Article**
https://doi.org/10.31900/ijl.v22i2.398

The Reliability of Two Different Laser Wavelengths in Inducing Bone Healing Around Dental Implants: Comparative Clinical Trial

Zahraa A. Alameeri*, Hussein A. Jawad

Institute of Laser for Postgraduate Studies, University of Baghdad, Baghdad, Iraq
** Email address of the Corresponding Author:zahraa.abdulrazaq12021a@ilps.uobaghdad.edu.iq*

Article history:Received17 June 2023; Revised 18 Aug 2023; Accepted 20 Aug 2023; Published online 15 Dec 2023

Abstract

Background/purpose: Dental implantology involves different treatments that have been used in conjunction with dental implant surgery to increase implant stability and bone regeneration process. Photobiomodulation(PBM) can be one of these techniques. The objective of this study was to evaluate the bone density around implants. **Materials and methods:** in this study, 10 individuals had 20 implants inserted in the posterior of their mandibles. each patient received two implants the left side served as the control whereas the right side served as the study group with a diode laser (same patients). measurements were made for each implant. Measurements were obtained using cone-beam computed tomography (CBCT). **Results:** Cone beam computed tomography (CBCT)analysis found statistically significant quotient differences between the study groups were discovered. (P = <0.001) had a better degree of bone integration than the control group after 3 months of observation of different powers the best power effect on bone density around the implant from group 1 is 50 mW while the best power in bone density around the implant from group 2 is 4 W Conclusion: Effective osteogenesis promotion by photobiomodulation is possible; the bone healing process was accelerated around implants by different powers of 650nm and 976nm of the laser's photobiomodulation action.

Keywords: Dental implantology; biostimulation; diode lasers; PBM; bone density.

1. Introduction

A dental implant (also known as an end-osseous implant) has been used to substitute missing teeth for more than 50 years. Modern dentistry aims to get the patient back to normal function., contour, comfort, esthetics, speech, and health by replacing teeth with a prosthetic or treating a diseased tooth, a dental implant is a significant development in dentistry as has improved greatly the success rate of replacing lost teeth (Warreth et al,2017). Success in implant dentistry depends on several parameters that may improve the phenomenon of osseointegration and new bone formation in close contact with the implant (Jani et al,2015).

Implant stability is considered one of the most important factors affecting the healing and successful osseointegration of dental implants (Ibraheem et al,2015). The stability of an implant is its ability to sustain loads in axial, lateral, and rotational directions (Staedt et al,2020). Generally known to be "a measurement of the difficulty of moving an item or system from equilibrium (Atsumi et al,2007). Secondary stability results from osteointegration, a biological process, whereas primary stability is mechanical (Yoshiki Oshida et al,2007). By coincidence, the Swedish orthopedist Branemark and his associates discovered osseointegration the occurrence of bone integration with titanium in the 1960s. Consequently, osseointegration includes the clinically asymptomatic, hard fixation of alloplastic materials, which is maintained during functional loads (Duqum et al,2008).Osseointegration is defined as the direct structural and functional connection between both the titanium implant surface and the organized vital bone, which can receive functional loads (Albrektsson et al,1981). This connection is characterized by forming a thin layer of bone tissue around the implant, which becomes firmly attached to the implant over time without fibrous tissue in between (Abdullah et al,2023).

The clinical success of dental implants is directed by the implant surface and bone cell responses that promote rapid osseointegration and long-term stability (Turkyilmaz et al,2007). Implant stability is considered one of the most important factors affecting the healing and successful bone healing of dental implants (Heinemann F et al, 2o15). Many attempts have been made in recent years to enhance implant shape, design, materials, and processes to accelerate bone healing. process and implant density success rates. treatment with PBM is a new technology that has been developed to the osseointegration surrounding dental implants should be improved. Based on its capacity to stimulate the biochemical and molecular processes involved in tissue repair, increased to promote the biochemical and molecular mechanisms needed for tissue (Arakeeb et al,2019).

Laser light irradiation has been applied in the medical field and has biostimulatory effects on wound healing, collagen synthesis, and fibroblast proliferation in addition, laser light appears to increase mitochondrial respiration and adenosine triphosphate (ATP) synthesis (Avci P et al,2013). Furthermore, an adequate method of measuring the effectiveness of primary stability and bone density is required. Since the removal torque method and histomorphometry analysis measurements are invasive techniques (Matys et al,2015). Additionally, it has been noted that cone-beam computed tomography (CBCT) offers submillimeter isotropic voxels that enable precise measurements of bone density (error 0.1) (Matys et al,2019). The method can be considered a preferential diagnostic tool for bone, density evaluation during implant treatment as it provides qualitative and quantitative analysis (Matys et al,2015) (Dahiya et al,2018). Noninvasive osseointegration assessment technologies include X-ray imaging, cone beam computed tomography (CBCT), multislice computed tomography (CT), and micro-computed tomography (MCT) (Arakeeb et al 2019). Some studies have reported that PBMT has the best result when compared with other methods (Matys et al,2015) while other studies have reported no significant difference. This controversy may be due to multiple factors, some related to laser parameters and others related to the incorrect diagnosis of selected patients (García-Morales et al,2012). Any implant procedure's success is influenced by several patients- and procedure-related factors, including the patient's overall health the implant surface design, the biocompatibility of the implant material, the surgical procedure, and the quantity and quality of the surrounding bone (Parithimarkalaignan et al,2013).

The purpose of the study was to compare the effects of 650 and 976 nm diode lasers of varying powers on bone density around implants using computed tomography (CBCT). Using OnDemand software, relative bone density (RBD) was determined by placing a simulated implant at the inserted implant and adjusting it to the same size and position, then measuring the relative bone density using the software's verification tool.

2. Materials and method

The study was performed in line with the principles of the Declaration of Helsinki. Approval was granted by the Institute of Laser for post-graduate studies.

3. Design and Investigation of Nanowire Metasurface Grating Polarizer

Ten male patients (age: 30-50 years) with missing teeth for at least 6 months were randomly selected for this study. Each patient had received two implants (neoabietic company), On both sides of the lower jaw. According to the delayed implant placement protocol, the late insertion approach requires a 6- to 8-month waiting period between tooth extraction and implant placement (Gallucci GO et al 2018). Each group (divided into 2 groups Group 1(study group) 650nm (n=5, 10 implants), power used is 25 mW,50 mW, 75 mW,100 mW, and 200 mW on the right-side Time used 40 seconds, continuous emission mode and group 2 (study group) treated with 975nm (n=5,10 implants) power used is 0.5W,1W,1.5W,2W,4W on the right side. Time used 40 seconds, continuous emission mode. The left side of each group served as a control.

4. Diode Laser

The Woodpecker LX 16 diode laser used two wavelengths 650 nm and 976 nm, handpiece diameter:8mm, output differentness power, spot area: 0.5024 cm^2, continuous mode, time: 40 sec per point, 2 points (irradiation on a buccal and a lingual side of the alveolus/implant). when the irradiance law is used (irradiance = power/cm^2). Inclusion Criteria: Patients ranged in age from 30 to 50; they were missing lower posterior teeth; the working regions were edentulous for at least 6 months; and the investigation was performed on the lower jaw's two-sided structure. is shown in Fig.1.

Fig. 1. The patient's lower jaw two-sided missed lower posterior teeth.

The group1 and group2 (test) group's implants were irradiated with the aluminum gallium arsenide (diode laser) from Woodpecker Company according to the following protocol: immediately after the surgery and 3, 5, 7, 9,11,13,15,17, and 19 days. Exclusion Criteria Patients with significant bone loss, diseases that slow the healing process, such as diabetes and thyroid disease, females who could have hormonal changes that might alter the research's findings (Koszuta P et al 2015), and patients who get radiation or chemotherapy are all excluded from the study.

5. Surgical phase

All patients had surgery under local anesthetic made up of 2% lidocaine and 1:100,000 epinephrine, both provided by Novocol Pharmaceutical of Canada. Lower mandibular posterior left and right had a horizontal mid-crestal incision made using a #15 Bard-Parker blade through the connected gingival and rather lingual to the ridge's crest (3-4 mm to the crest), and the mucoperiosteal flap was bluntly dissected with a periosteal elevator and performed exposed buccally and lingually by a reflection on the alveolar ridge's buccal side.

Osteotomies were performed using a starting drill with a pilot hole of 2.0 mm, followed by further drills directed by the manufacturer at a drilling speed of (800 rpm), then the implant was put in its position shown in Fig.2. A Preoperative CBCT (Kavo OP 3D PRO, Biberach, Germany) was performed on the patients to assess bone density using the OnDemand3DTM software (Cybermed Inc., Seoul, Korea) (Mello-Machado et al., 2021). To examine the relative bone density around each implant, all patients in the two groups were tested by CBCT on the first day after implant insertion, followed by another one month later, and finally after three months. Relative bone density (RBD) was measured around the implants with OnDemand software by placing a simulated implant at the implanted implant and adjusting to the identical size and position, then measuring. The software's verification function was used to determine the relative bone density as shown in Fig.3.

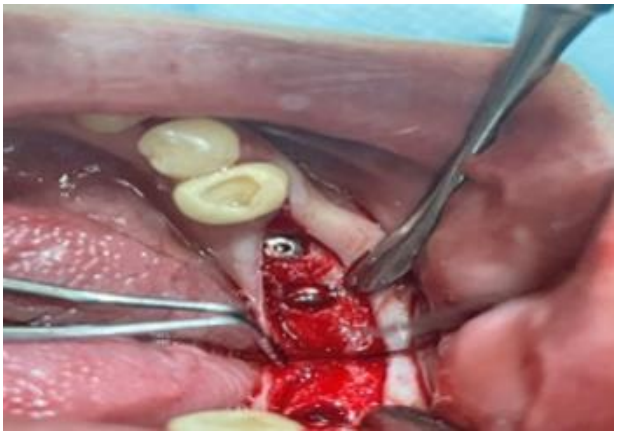

Fig. 2. Patient after implant placement.

Fig. 3. Using the verification tool in the simulation, measuring the relative bone density surrounding the simulated implants in On-Demand software.

Bone density (grayscale value) was measured at the two-sided around implant the implant of each patient. The greyscale value for all subjects was measured by CBCT software in recent years (CBCT) and has grown in acceptance in the dental field. Other studies discovered a strong correlation between the Hounsfield unit calculated from CBCT voxel values and real parameters of bone density acquired from Micro-CT and multi-slice CT, suggesting that CBCT may be used to measure bone density.

6. Statistical analysis

ANOVA analysis was performed. repeated measure compared to the control concentration. Information presented as mean SD. The letters (A, B, C, and D) are extremely significant beginning with the letter (A) or (a), decreasing with the final one. The least significant difference (LSD) test was used to assess the significant differences between the tested mean. Similar letters indicate that the tested means are not significantly different from one another. Values of $p>0.05$ were considered statistically unimportant while $p\leq0.05$ and $<0.01,0.001$ were considered extremely significant differences, significant differences respectively. The statistical analysis was carried out by SPSS (v 20).

7. Results

Measurement was taken for bone density around the implant in the Hounsfield unit for (HU) each implant between tested and controlled by On-Demand software immediately after implant placement, one month and 3rd month.

7.1 Bone density for the 650 nm group

The best result affected bone density around the implant in one day with a maximum mean value was 2112.96 HU. Following this, after one month of exposure to laser light at a wavelength of 650 nm, a power of 50 (mW) was found to have the best effect on bone density. This was supported by a maximum mean value of 1982.46 HU. When assessing the impact of laser wavelength on bone density over three months, the analysis indicated that a power level of 50 mW had the most significant effect on bone density around the implant area. This was evident through a mean value of 2134.52 HU. These findings are presented comprehensively in Table 1 and visualized through Figure 4, providing a clear representation of the influence of power levels and laser wavelength on bone density around implants.

Fig. 4. Comparison of power levels and their effects on bone density were analyzed across various study periods, focusing specifically on bone density around implants within Group 1.

Table 1: Comparison powers on bone density between the different studied periods according to bone density around implants of group 1.

Powers of 650 nm in watt	Bone density around implant in HU with 650 nM		Bone density around implant in HU with control		P VALUE
25	**mean**	**SD**	**Mean**	**SD**	
Time 1day/25	C 1297.18	376.10	1856.73	1188.94	0.001
Time 30 day/25	B 1866.36	826.58	1886.39	1247.12	NS
Time 90 day/25	**A 2049.67**	823.69	2015.71	1254.99	NS
P value	0.001		NS		
50	**mean**	**SD**	**Mean**	**SD**	**P VALUE**
Time 1day/50	**A 2112.96**	1311.34	B 1860.20	1259.48	0.001
Time 30 day/50	B 1982.46	1060.26	C 1638.83	956.65	0.001
Time 90 day/50	A 2134.52	1193.16	A 2007.37	1777.57	0.05
P value	0.001		0.001		
75	**mean**	**SD**	**Mean**	**SD**	**P VALUE**
Time 1day/75	C 1486.59	1106.23	A 1909.28	1349.39	0.001
Time 30 day/75	A 1768.11	918.38	C 1599.37	592.58	0.001
Time 90 day/75	B 1643.32	694.22	B 1719.56	586.41	0.05
P value	0.001		0.001		
100	**mean**	**SD**	**Mean**	**SD**	**P VALUE**
Time 1dy/100	C 1609.48	1451.46	1645.35	1400.74	NS
Time 30 day/100	B 1909.28	1349.39	1552.75	1277.01	0.001
Time 90 day/100	**A 2010.83**	1247.75	1683.27	1277.11	0.001
P value	0.001		NS		
150	**mean**	**SD**	**Mean**	**SD**	**P VALUE**
Time 1day/150	**C 1650.31**	990.09	1683.49	961.60	-
Time 30 day/150	**B 1768.41**	917.95	1751.48	875.43	-
Time 90 day/150	**A 1940.83**	934.06	1737.33	746.72	-
P value	0.001		NS		

Time: Time of measurement/ Day of implant placement.
*P value: calculated between the three times of measurement/LSD test was used to calculate the significant differences between tested mean, the letters (A, B, and C) represented the levels of significant, highly significant start from the letter (A) and decreasing with the last one. Similar letters mean there are no significant differences between the tested mean. $p \leq 0.05$ were considered significantly different.

7.2 Bone density for the 976 nm group

In one day, the maximum recorded power mean value is 2112.96 Hounsfield Units (HU) was achieved at a power of 1 watt. After one month, the most favorable power level for enhancing bone density in patients exposed to laser light at a wavelength of 976 nm was 4 watts. At this power level, the average mean value reached 2456.47 HU. The subsequent effective power level was 1 watt, resulting in an average bone density of 2346.23 HU. After three months, the impact of laser wavelength on bone density was examined. The most notable improvement in bone density around the implant site, with a maximum average of 2941.10 HU, was observed at a power level of 4 watts. Following closely was a power level of 1.5 watts, yielding an average bone density of 2636.50 HU. These findings are detailed in Table 2 and illustrated in Fig. 5.

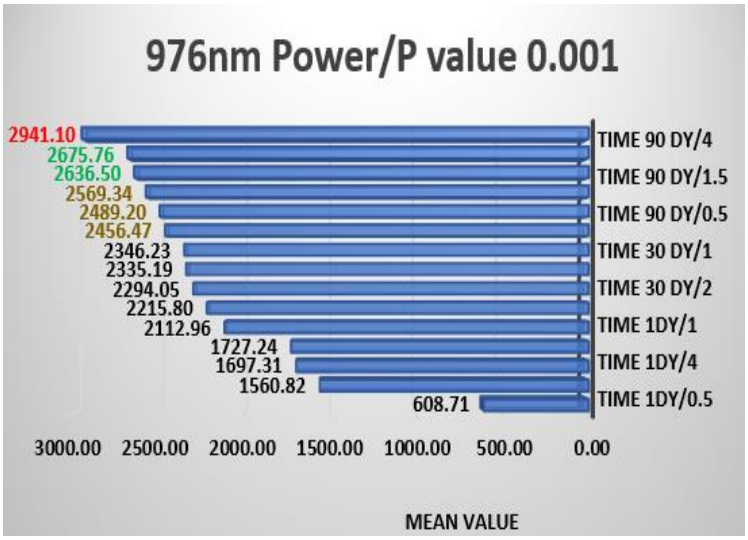

Fig. 5. Comparison powers on bone density between the different studied periods according to bone density around implants of group 2.

8. Discussion

Extrinsic bone healing stimuli, including those associated with the use of PBM, have been shown to improve implant osseointegration and have a positive impact on the healing and attachment of titanium implants (Blay et al,2016). Authors believe that the administered dose, or the proper energy density and power, determines the metabolic changes carried about by PBM that stimulate tissue regeneration as well as the proliferation and viability of reparatory cells (Fahimipour et al,2013). There is a lot of discussion around the research studies that have looked at how PBM alters the process of bone regeneration, which suggests that further studies are necessary to determine how PBM affects bone tissue (Fávaro-Pípi et al,2010). Our study aimed to determine the impact of the photo modulation on implant-bone density following peri-implant soft tissue irradiation with a 650 nm and 976nm diode laser accounted for significantly greater bone density after 3rd month in contrast to nonirradiated subjects. The main finding of the study was the best power of 4Win laser 976nm bone density around the implant after one month and 3rd month Because, in the infrared region, the absorption rate is small, so in order to obtain the best result, we increase power while in BDI the best power effect for the similar period the effect of 50 mW due to the absorption rate is higher in the visible region, so we did not need a higher power until we get bone density. The results of our study were in good agreement with (Matys et al,2019) found improved bone density, in the red to the near-infrared spectrum (600–1500nm), Thus, the energy can be absorbed by the soft tissue and bone.

Table 2: Comparison powers on bone density between the different studied periods according to bone density around implants of group 2

976 nm powers in watt	Bone density around implant in HU with 976 nm		Bone density around implant in HU control		P value
0.5	**mean**	**SD**	**Mean**	**SD**	
Time 1day/0.5	C 608.71	597.70	C 1083.26	160.71	0.001
Time 30 day/0.5	B 2215.80	402.05	B 1873.44	827.97	0.001
Time 90 day/0.5	**A 2489.20**	472.09	A 1936.09	806.62	0.001
P value	0.001		0.001		
1	**mean**	**SD**	**Mean**	**SD**	**P value**
Time 1day/1	C 2112.96	1311.34	C 1723.70	1452.52	0.001
Time 30 day/1	B 2346.23	691.10	B 2059.83	1552.04	0.001
Time 90 day/1	**A 2675.76**	812.27	A 2137.84	1521.12	0.001
P value	0.001		0.001		
1.5	**mean**	**SD**	**Mean**	**SD**	**P value**
Time 1day/1.5	C 1727.24	1102.44	C 1768.11	918.38	NS
Time 30 day/1.5	B 2335.19	507.12	B 1999.37	1158.26	0.001
Time 90 day/1.5	**A 2636.50**	372.65	A 2156.87	1225.07	0.001
P value	0.001		0.001		
2	**mean**	**SD**	**Mean**	**SD**	**P value**
Time 1day/2	C 1560.82	528.99	C 1965.48	1462.40	0.05
Time 30 day/2	B 2294.05	192.71	B 2061.51	1553.90	0.001
Time 90 day/2	**A 2569.34**	248.99	A 2138.68	1511.16	0.001
P value	0.001		0.001		
4	**mean**	**SD**	**Mean**	**SD**	**P value**
Time 1day/4	C 1697.31	1158.91	C 2007.00	1119.29	0.001
Time 30 day/4	B 2456.47	633.45	B 2138.37	1043.29	0.001
Time 90 day/4	**A 2941.10**	673.94	A 2260.88	1061.60	0.001
P value	0.001		0.001		

PBM also encourages nondifferentiated mesenchymal cells to differentiate into osteoblasts, which turn into osteocytes more quickly, and acts as an inducer factor that enhances vascularization has an anti-inflammatory impact, and enhances collagen synthesis, thus enhancing the bone healing process (Lopes et al,2005).The results from (Lopes et al,2005) support this study. Who concluded that PBM encourages improved bone regeneration around dental implants. On the other side, numerous studies have shown that PBM has no benefits and may even have negative consequences on osseointegration, (Pereira et al). This controversy may be attributed to many factors such as selected wavelength, high dose or very low dose, irradiation time, spot size, improper diagnosis, and the number of session treatments (Herranz-Aparicio J et al 2013). To overcome this problem a proper adjustment to power density is needed Within a specific relationship between dose and output power, PBM energy was discovered to have a favorable effect on bone regeneration.

9. Conclusion

Despite the limitations of this study, it can be concluded that photobiomodulation can significantly enhance bone healing around dental implants.

Author Contributions

All authors have contributed to the study's conception and design. The manuscript was written by [Zahraa A. Alameri]. Also, data collection and analysis were performed by [Zahraa A. Alameri]. Material preparation was performed by [Hussein A. Jawad]. All authors have read and approved the final manuscript before submission.

Acknowledgments

The authors would like to thank the Woodpecker company for its support with sensor equipment.

References

Abdullah, Zainab Saleh, Mustafa Shaker Mahmood, Faiza Mohammed Ali Abdul-Ameer, and Abdalbseet Ahmad Fatalla. (2023)."Effect of commercially pure titanium implant coated with calcium carbonate and nanohydroxyapatite mixture on osseointegration." Journal of Medicine and Life., **16** (1): 52.

Albrektsson, T., P-I. Brånemark, H-A. Hansson, and J. Lindström. (1981)."Osseointegrated titanium implants: requirements for ensuring a long-lasting, direct bone-to-implant anchorage in man." Acta Orthopaedica Scandinavica., **52** (2): 155-170.

Arakeeb, Mohamed Ali Ali, Ahmed Abbas Zaky, Tarek Abdel-Hamid Harhash, Walid S. Salem, and Mohamed El-Mofty. (2019."Effect of combined application of growth factors and diode laser bio-stimulation on the osseo integration of dental implants." Open Access Macedonian Journal of Medical Sciences., **7**(15): 2520.

Atsumi, Mihoko, Sang-hoon Park, and Hom-Lay Wang. (2007)."Methods used to assess implant stability: current status." International Journal of Oral & Maxillofacial Implants., **22**(5):743-54.

Avci P, Gupta A, Sadasivam M, Vecchio D, Pam Z, Pam N, Hamblin MR. (2013)."Low-level laser (light) therapy (LLLT) in skin: stimulating, healing, restoring". InSeminars in cutaneous medicine and surgery"., **32**(1): 41–52.

Blay, Alberto, Claudia C. Blay, Samy Tunchel, Sergio Alexandre Gehrke, Jamil Awad Shibli, Eduardo B. Groth, and Denise M. Zezell. (2016)."Effects of a low-intensity laser on dental implant osseointegration: Removal torque and resonance frequency analysis in rabbits." Journal of Oral Implantology., **42**(4): 316-320.

Dahiya, Kirti, Narendra Kumar, Pankaj Bajaj, Avdesh Sharma, Rohan Sikka, and Sagar Dahiya. (2018). "Qualitative Assessment of Reliability of Cone-beam Computed Tomography inevaluating Bone Density at Posterior Mandibular Implant Site." The Journal of Contemporary Dental Practice., **19** (4): 426-430.

Duqum, Ibrahim Salim. (2008)."A Comparative study on the effect of Integrin subunits Beta one and Beta 3 on Osteoblast Implant interactions."

Fahimipour, Farahnaz, Mina Mahdian, Behzad Houshmand, Mohammad Asnaashari, Alireza Naser Sadrabadi, Seid Emadadin Najafi Farashah, Seid Mohsen Mousavifard, and Arash Khojasteh. (2013)."The effect of He-Ne and Ga-Al-As laser light on the healing of hard palate mucosa of mice." Lasers in medical science., **28**: 93-100.

Fávaro-Pípi, Elaine, Suellen Maurin Feitosa, Daniel Araki Ribeiro, Paulo Bossini, Poliani Oliveira, Nivaldo A. Parizotto, and Ana Claudia Muniz Renno. (2010)."Comparative study of the effects of low-intensity pulsed ultrasound and low-level laser therapy on bone defects in tibias of rats." Lasers in medical science., **25**: 727-732.

Gallucci GO, Hamilton A, Zhou W, Buser D, Chen S. (2018). "Implant placement and loading protocols in partially edentulous patients: A systematic review". Clinical oral implants research., **29**:106-34.

García-Morales, Joelle Marie, Pedro Tortamano-Neto, Francisco Fernando Todescan, José Carlos Silva de Andrade, Juliana Marotti, and Denise Maria Zezell. (2012)."Stability of dental implants after irradiation with an 830-nm low-level laser: a double-blind randomized clinical study." Lasers in medical science., **27**: 703-711.

Heinemann F, Hasan I, Bourauel C, Biffar R, Mundt T.(2015)."Bone stability around dental implants: Treatment related factors". Annals of Anatomy-Anatomischer Anzeiger.,**199**:3-8.

Herranz-Aparicio J, Vázquez-Delgado E, Arnabat-Domínguez J, España-Tost A, Gay-Escoda C. The use of low level laser therapy in the treatment of temporomandibular joint disorders. Review of the literature. Medicina oral, patologia oral y cirugia bucal. 2013 Jul;18(4):e603.

Ibraheem, Noor S., and Sahar S. Al-Adili. (2015)."Assessment of dental implant stability during healing period and determination of the factors that affect implant stability by means of resonance frequency analysis (Clinical study)." Journal of Baghdad College of Dentistry., **27**(3): 109-115.

Jani, Ghasak H., Shatha S. Al-Ameer, and Salam N. Jawad. (2015). "Histological and histomorphometric analysis of strontium chloride coated commercially pure titanium implant compared with hydroxyapatite coating." Journal of Baghdad College of Dentistry., **27**(1): 26-31.

Koszuta P, Grafka A, Koszuta A, Łopucki M, Szymańska J. (2015)."Effects of selected factors on the osseointegration of dental implants". Menopause Review/Przegląd Menopauzalny.,**14**(3):184-7.

Lopes, Cibelle B., Antônio LB Pinheiro, Sokki Sathaiah, Janaína Duarte, and Maria Cristinamartins. (2005). "Infrared laser light reduces loading time of dental implants: a Raman spectroscopic study." Photomedicine and Laser Therapy., **23**(1): 27-31.

Mandić, Borka, Zoran Lazić, Aleksa Marković, Bojan Mandić, Miška Mandić, Ana Đinić, and Biljana Miličić. (2015). "Influence of postoperative low-level laser therapy on the osseointegration of self-tapping implants in the posterior maxilla: a 6-week split-mouth clinical study." Vojnosanitetski pregled.,**72** (3): 233-240.

Matys, Jacek, Katarzyna Świder, Kinga Grzech-Leśniak, Marzena Dominiak, and Umberto Romeo. (2019)."Photobiomodulation by a 635nm diode laser on peri-implant bone: primary and secondary stability and bone density analysis—a randomized clinical trial." BioMed research international., **2019**: 2785302.

Matys, Jacek, Rafał Flieger, and Marzena Dominiak. (2017). "Effect of diode lasers with wavelength of 445 and 980 nm on a temperature rise when uncovering implants for second stage surgery: An ex-vivo study in pigs." Advances in Clinical and Experimental Medicine., **26** (4): 687-693.

Mello-Machado RC, de Almeida Barros Mourao CF, Javid K, Ferreira HT, Montemezzi P, Calasans-Maia MD, Senna PM. (2021)." Clinical assessment of dental implants placed in low-quality bone sites prepared for the healing chamber with osseodensification concept: A double-blind, randomized clinical trial". Applied Sciences.,**11**(2):640.

Parithimarkalaignan S., and T.V. Padmanabhan.(2013)."Osseointegration: an update." The Journal of Indian Prosthodontic Society, **13**(1): 2-6.

Pereira, Cecília Luiz, Enilson Antônio Sallum, Francisco Humberto Nociti Jr, and Roger William Fernandes Moreira. (2009)."The effect of low-intensity laser therapy on bone healing around titanium implants: a histometric study in rabbits." International Journal of Oral & Maxillofacial Implants, **24**(1).

Staedt, Henning, Peer W. Kämmerer, Elisabeth Goetze, Daniel GE Thiem, Bilal Al-Nawas, and Diana Heimes. (2020)."Implant primary stability depending on protocol and insertion mode—An ex
vivo study." International Journal of Implant Dentistry, **6**(1): 1-9.

Turkyilmaz, I., T. F. Tözüm, and C. Tumer. (2007)."Bone density assessments of oral implant sites using computerized tomography." Journal of oral rehabilitation, **34**(4): 267-272.

Warreth, Abdulhadi, Najia Ibieyou, Ronan Bernard O'Leary, Matteo Cremonese, and Mohammed Abdulrahim. (2017)."Dental implants: An overview." Dental Update, **44**(7): 596-620.

Yoshiki Oshida. "Osseointegration and bioscience of implant surfaces-current concepts at bone-implant interface." Implant Dentistry-A Rapidly Evolving Practice, 978-953 (2011): 307-658.

Zein, Randa, Wayne Selting, and Stefano Benedicenti. (2017). "Effect of low-level laser therapy on bone regeneration during osseointegration and bone graft." Photomedicine and laser surgery, **35**(12): 649-658.

موثوقية طولين مختلفين من موجات الليزر في تحفيز التئام العظام حول زراعة الأسنان: تجربة سريرية مقارنة

زهراء عبد الرزاق*، حسين علي جواد

معهد الليزر للدراسات العليا، جامعة بغداد، بغداد، العراق

*البريد الإلكتروني للباحث : zahraa.abdulrazaq12021a@ilps.uobaghdad.edu.iq

الخلاصة

الخلفية / الغرض: تتضمن زراعة الأسنان علاجات مختلفة تم استخدامها جنبًا إلى جنب مع جراحة زراعة الأسنان لزيادة استقرار الغرسة وعملية تجديد العظام. يمكن أن يكون التعديل الضوئي (PBM) أحد هذه التقنيات. كان الهدف من هذه الدراسة هو تقييم كثافة العظام حول الغرسات.

المواد والطرق: في هذه الدراسة ، تم إدخال 20 غرسة في الجزء الخلفي من الفك السفلي لعشرة أفراد. تلقى كل مريض غرستين. الجانب الأيسر كان بمثابة التحكم بينما عمل الجانب الأيمن كمجموعة الدراسة باستخدام ليزر ديود (نفس المرضى). تم إجراء قياسات لكل غرسة. تم الحصول على القياسات باستخدام التصوير المقطعي المحوسب ذو الحزمة المخروطية (CBCT).

النتائج: وجد تحليل التصوير المقطعي بالحزمة المخروطية (CBCT) فروق ذات دلالة إحصائية في الحاصل بين مجموعات الدراسة. ($P = <0.001$) كان لديها درجة تكامل عظمي أفضل من المجموعة الضابطة بعد 3 أشهر من ملاحظة القوة المختلفة ، أفضل تأثير للطاقة على كثافة العظام حول الغرسة من المجموعة 1 هو. 50 ميغاواط في حين أن أفضل قوة في كثافة العظام حول الغرسة من المجموعة 2 هي 4 واط. **الخلاصة**: تعزيز تكوين العظم الفعال عن طريق التعديل الحيوي الضوئي ممكن ؛ تم تسريع عملية شفاء العظام حول الغرسات بواسطة قوى مختلفة من 650 نانومتر و 976 نانومتر من عمل التعديل الضوئي بالليزر.

IJL, Issue 2, Vol. 22, 2023 **Research Article**
https://doi.org/10.31900/ijl.v22i2.384

Study the Impact of Silica Nanoparticles on the Properties of Several Dyes for the Fabrication of a Random Laser Gain Medium

Noor Y. Khudair*, Mohammed K. Dhahir

Institute of Laser for Postgraduate Studies, University of Baghdad, Baghdad, Iraq
** Email address of the Corresponding Author: Noor.Yasir2101m@ilps.uobaghdad.edu.iq*

Article history: Received 16 Mar 2023; Revised 25 Aug 2023; Accepted 4 Sep 2023; Published online 15 Dec 2023

Abstract: Random laser gain media is synthesized with different types of dye at the same concentration (1×10^{-3} M) as an active material and silicon dioxide NPs (silica SiO_2) as scatter centers through the Sol-Gel technique. The prepared samples are tested with UV–Vis spectroscopy, Fluorescence Spectroscopy, Field Emission Scanning Electron Microscopy (FESEM), and Energy Dispersive X-ray Diffraction (EDX). The end result demonstrates that doped dyes with silica nanoparticles at a concentration of 0.0016 mol/ml have lower absorbance and higher fluorescence spectra than pure dyes. FESEM scans revealed that the morphology of nanocrystalline silica is clusters of nano-sized spherical particles in the range (25-67) nm. It is concluded that the various dyes with SiO_2 as a scattering center can be proposed to build laser media.

Keywords: Random lasers, sol-gel, silica (SiO_2), dyes, nanoparticles.

1. Introduction

Since the introduction of the first laser in 1960, the manufacturing of high-efficiency laser systems has been one of the most fundamental difficulties in laser physics [1–2]. Lawandy et al. demonstrated in the early 1990s a stimulated emission from laser dye containing microparticles, hence the phrase "random laser" [3], which led to several theoretical [4–5] and experimental [6–7] studies on the amplification of light in diffusive media.

The mechanisms of random lasers (RLs) are based on multiple light scattering . In random lasers, as opposed to two highly reflecting mirrors in conventional lasers, the resonant cavity is constructed by repeated multiple scattering. In an active medium with a disordered distribution of scattering particles or domains, fluorescence photons may be multi-scattered thousands of times in random directions before leaving the medium. When scattering photons propagate via a narrow circuit, recurrent multiple scattering may either produce incoherent or coherent feedback [8]. RL has several advantages such as small size, low cost, flexible shape, and many others; It has several applications in integrated optics [9], temperature

sensing [10], document encoding, material labeling, high-density optical data storage [11], tumor diagnostics [12-13], liquid crystal display [14], and liquid flow monitoring [15]. Many random laser mediums have been widely demonstrated, including ZnO powders [16-17], Rare-earth ion-doped crystalline powders [18-19], conjugated polymers [20-21], dye-doped liquid crystals [22-23], dye-doped polymer films enhanced by silver or gold nanoparticles [24- 25], a few biological issues doped with laser dye [26-27], and organic dye solutions doped with dielectric scatters [3–28].

Laser dyes are one of the organic luminescent materials with high molecular weight that can be used as an active medium because they are composed of carbon atom chains connected alternately by a single and double band called chromfore [29], while many tiny particles such as TiO_2 particles, zinc oxide (ZnO) [30], silica (SiO_2), tungsten oxide (WO_3), alumina (Al_2O_3) [31], and others can be used as scatter.

The goal of this work is to create random laser gain media by doping silica nanoparticles (SiO_2) with different types of dye (Rhodamine B, Rhodamine 101, Crystal Violet, and Fluorescein) at the same concentrations (1×10^{-3} M) in the Sol-Gel method and studying its characterization features.

2. Experimental work

The fabrication of random laser gain media through the sol-gel technique includes mixing 3 ml of ethanol as a solvent (purity 99.9%), 3 ml of tetraethylorthosilicate (Glentham Life Sciences Ltd., 99% purity) as a precursor material, 3 ml of deionized water (pH = 1 by adding 0.15 ml of HCl as a catalyst), and 0.6 ml (0.0001g dissolved in ethanol) from Rhodamine 610 and Rhodamine 640 dyes (supplied by Lambda Physik), Crystal Violet dye (supplied by Avonchem Limited) and Fluorescein dye (supplied by Sinopharm Chemical Reagent) to make all the prepared samples at a concentration of (1×10^{-3} M).

The mixtures are stirred for 15 minutes at 100ºC on the magnetic stirrer, and then the samples are aged and dried at room temperature for around 4 days in closed glass vials to produce four disk samples of random laser gain media. Energy Dispersive X-ray Diffraction (EDX) with XFlash 6L10, Field Emission Scanning Electron Microscopy (FE-SEM) with Inspect TM F50, UV-Visible spectrometry with a Shimadzu UV-VIS 1800 spectrophotometer, and F96 Shanghai Leng Guang Fluorescence Spectrophotometer were used to analyze the structural and optical characteristics of random laser gain media in the Sol-Gel technique.

3. Results and discussion

3.1 Morphological properties

As shown in Fig.1, SEM images indicate clusters of spherical, bright spots (circles and inset picture) that correspond to silicon oxide (SiO_2) nanoparticles with a mean particle size of around (25–67) nm for all prepared samples. By exhibiting peaks corresponding to the energy levels for each element in the test, EDX was used to confirm the structural purity of the samples.

As shown in Fig.2 , all of the samples contain Si as the highest peak in the spectrum, indicating that it is the most concentrated element; the presence of an O peak also confirms the stoichiometry of the silica NPs compound. The other peaks reflect the constituent elements of the dyes in the samples.

3.2 Optical properties

Using UV-Vis spectroscopy, the optical characteristics of the samples were determined. Fig.3 displays the absorption spectra of pure and doped dyes (Rh 101, Rh B, C.V., Fluorescein) with silica at the same concentration (1×10^{-3} M), where the absorption spectra moved to a longer wavelength in the visible region (red shift) after it was doped with SiO_2. This indicates the aggregation of nanoparticles in the dye solution [32], resulting in a shift in wavelengths. While Fig.4 shows the optical transmission spectra of pure and silica-doped dyes , the absorbance spectra for all samples exhibit the opposite pattern.

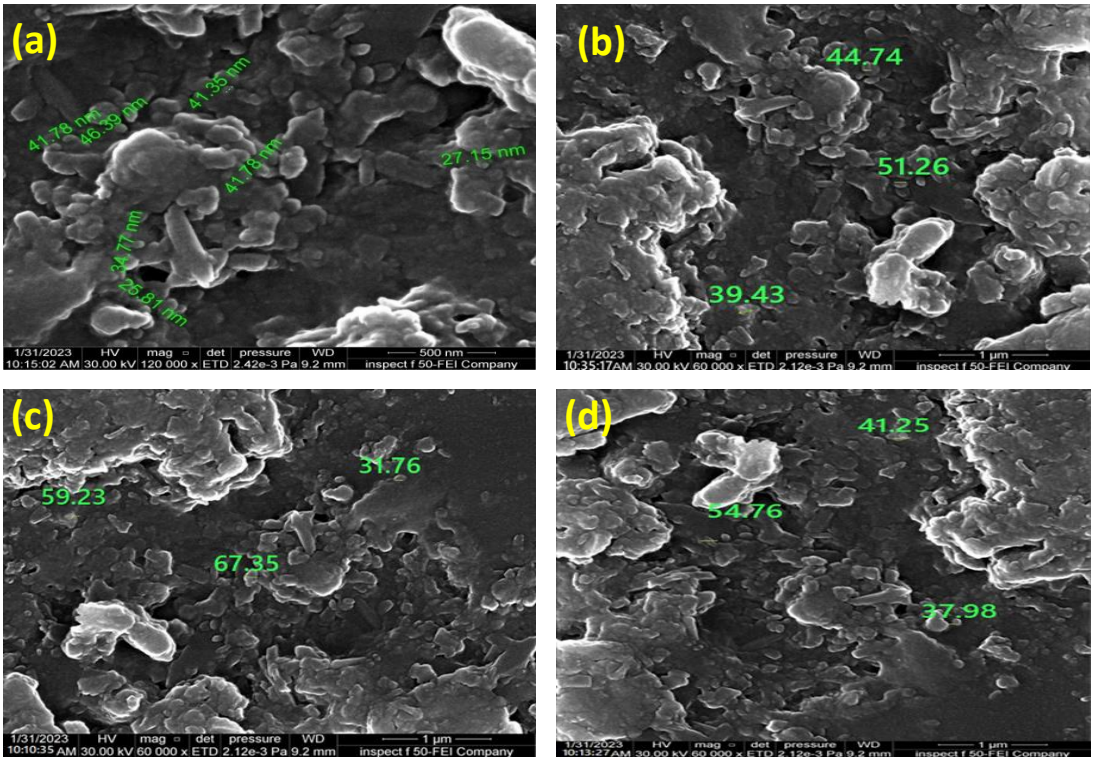

Fig. 1: SEM image of dyes (a) Rh 101, (b) Rh B , (c) C.V , (d) Fluorescein doped with SiO_2 NPs.

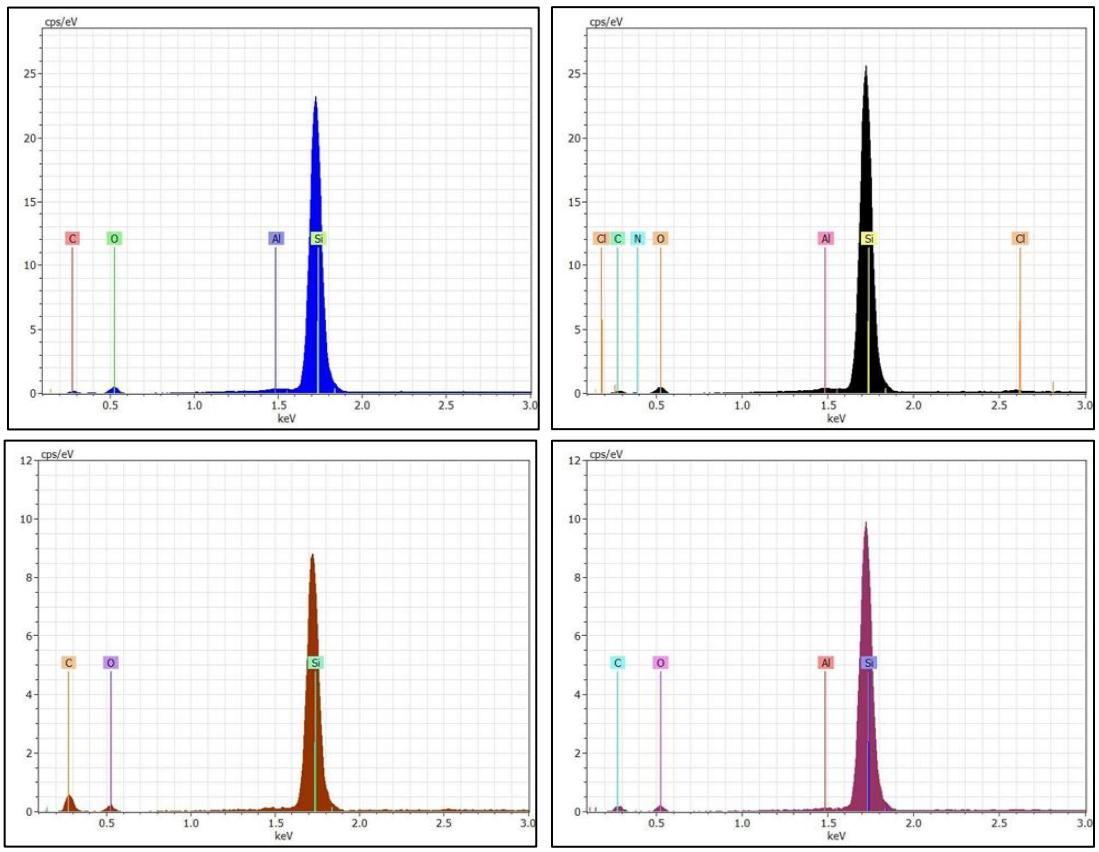

Fig. 2: EDX results of dyes (a) Rh 101, (b) Rh B, (c) C.V , (d) Fluorescein doped with SiO_2 NPs.

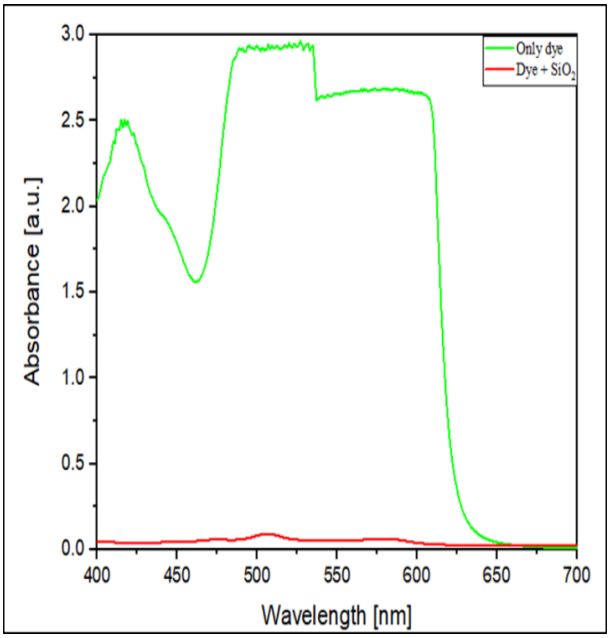

(a)

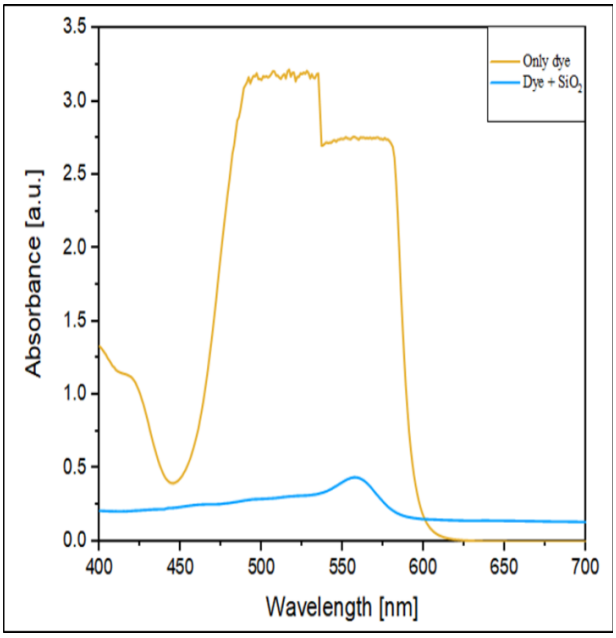

(b)

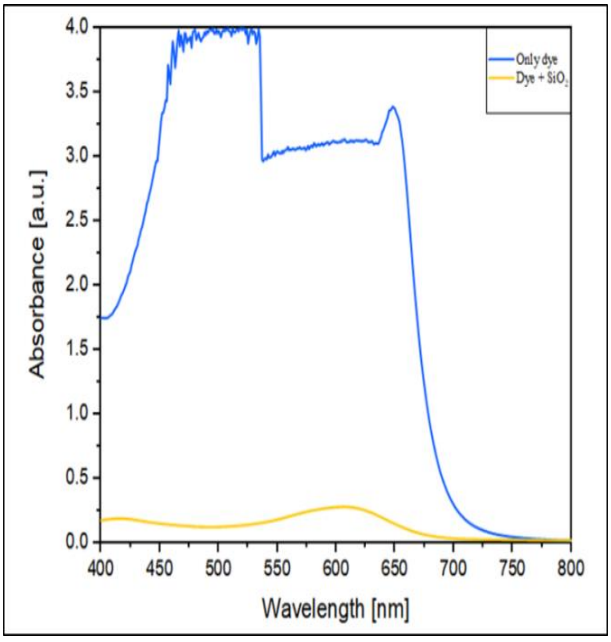

(c)

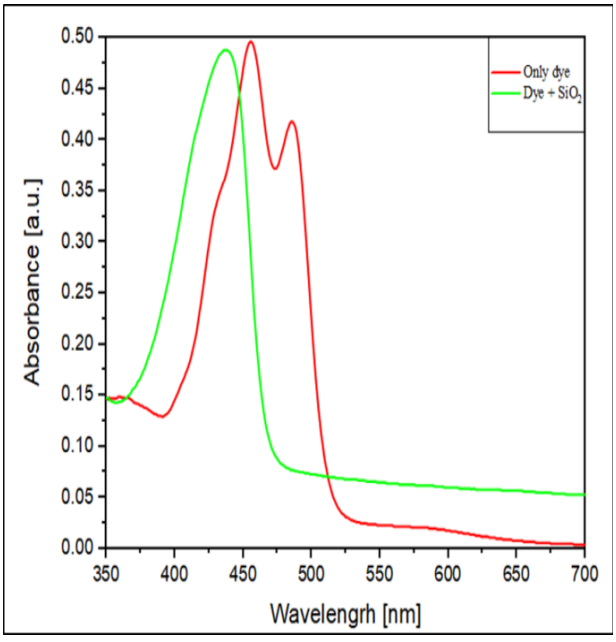

(d)

Fig. 3 Optical absorbance spectra of pure and doped dyes at the same concentration with SiO_2 for (a) Rh 101 (b) Rh B (c) C.V (d) Fluorescein.

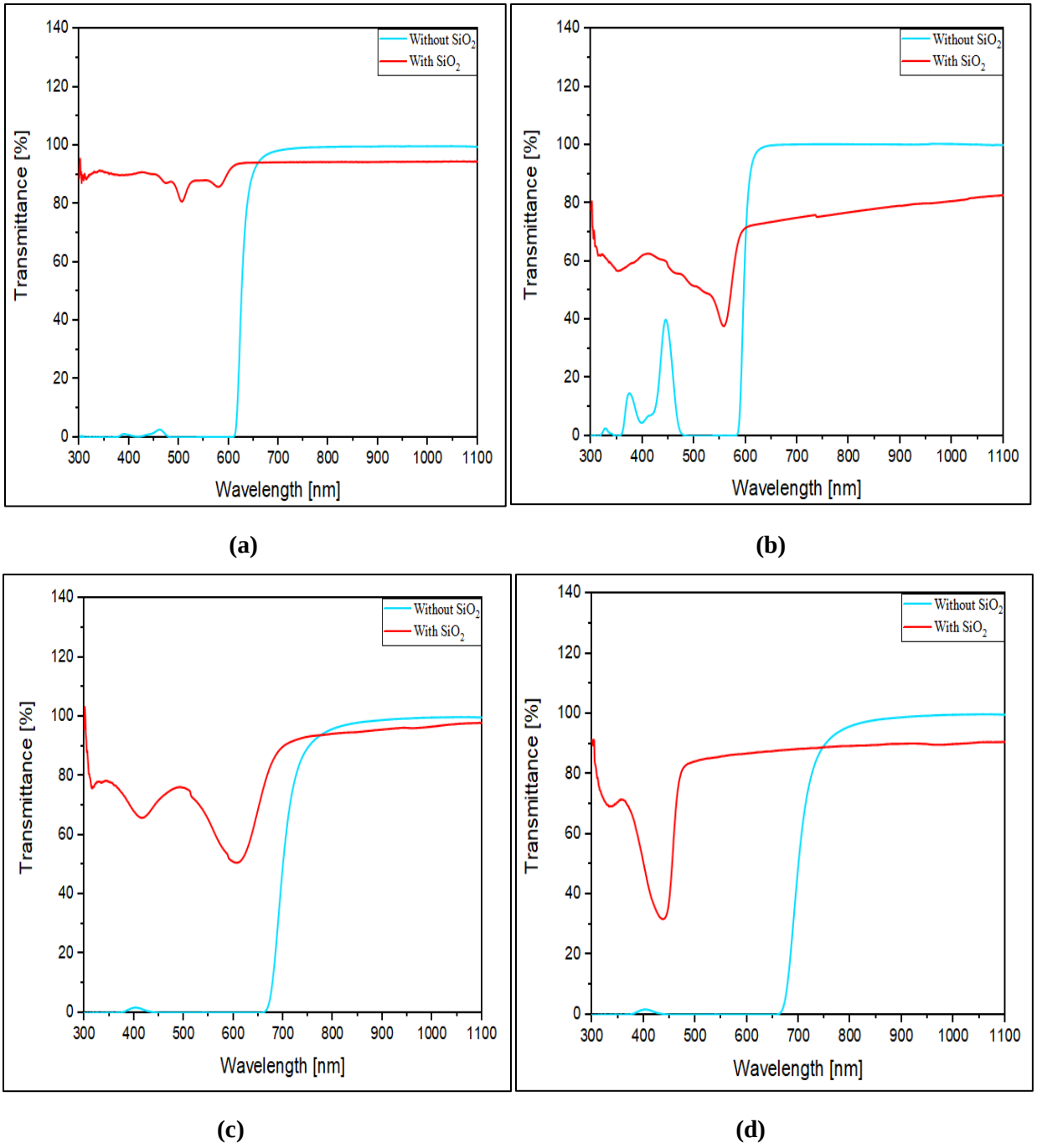

Fig. 4: Optical transmittance spectra of pure and doped dyes at the same concentration with SiO_2 for (a) Rh 101 (b) Rh B (c) C.V (d) Fluorescein. [This is what the results revealed, and they are presented as is].

Fluorescence spectra were acquired using an F96 Shanghai Leng Guang Fluorescence Spectrophotometer. Fig. 5 displays the fluorescence spectra of pure and doped dyes (Rh 101, Rh B, C.V., Fluorescein) with silica at the same concentration (1×10^{-3} M), where the fluorescence spectra became higher after it was doped with SiO_2 with a concentration of 0.0016 mol/ml since nanoparticles can exhibit unique optical and electronic properties that are not present in bulk materials, which means that they can absorb light energy and transfer it to the host material, leading to higher fluorescence

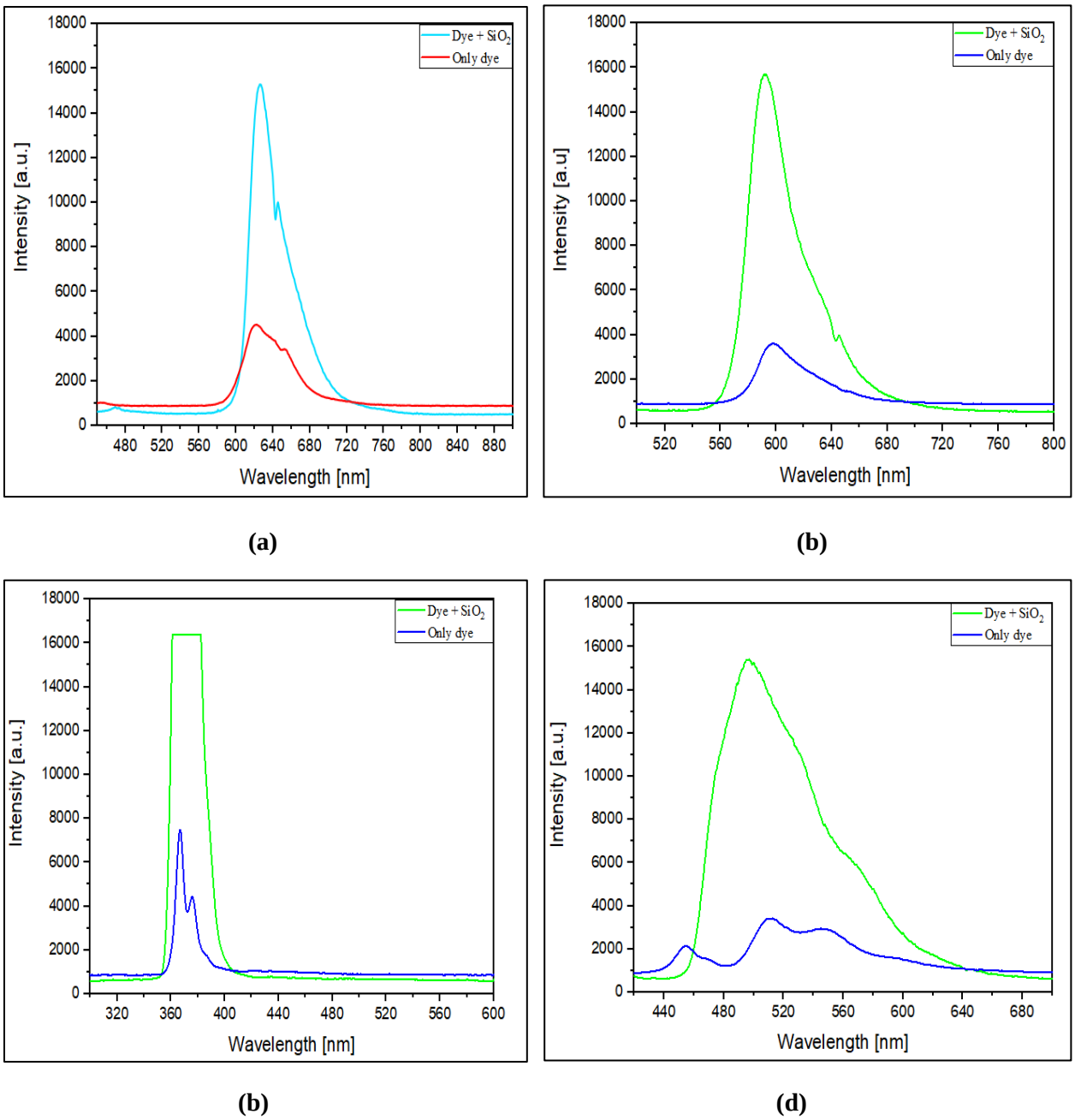

Fig. 5: Optical fluorescence spectra of pure and doped dyes at the same concentration with SiO_2 for (a) Rh 101 (b) Rh B (c) C.V (d) Fluorescein.

4. Conclusion

Using the sol-gel process, several dyes with SiO_2 as a scatter are successfully used to create random laser gain media. FESEM images show that the SiO_2 particles generated in the entire sample are in the nano range (100 nm), EDX demonstrates that Si is the most prevalent element in every sample, UV-Vis spectra demonstrate that all pure dyes have a higher absorbance than when they are doped, and the Fluorescence Spectrophotometer demonstrates that the fluorescence spectra became higher after it was doped with SiO_2 in all samples. [The proposed opinion will be applied to future studies].

References

[1] M. Maeda, Laser dyes: properties of organic compounds for dye lasers. Academic Press, 1984.
[2] S.K. Turitsyn et al., "Random distributed feedback fibre lasers", Phys. Rep., **542**(2),133- 193(2014).
[3] N. M. Lawandy, R. M. Balachandran, A. S. L. Gomes, and E. Sauvain, "Laser action in strongly scattering media," Nature, **368** (6470), 436–438 (1994).
[4] W. L. Sha, C.-H. Liu, and R. R. Alfano, "Spectral and temporal measurements of laser action of Rhodamine 640 dye in strongly scattering media," Opt. Lett.,**19**(23), 1922–1924 (1994).
[5] G. Van Soest, F. J. Poelwijk, R. Sprik, and A. Lagendijk, "Dynamics of a random laser above threshold," Phys. Rev. Lett., **86**(8)1522 (2001).
[6] S. John and G. Pang, "Theory of lasing in a multiple-scattering medium," Phys. Rev. A, **54**(4) , 3642 (1996).
[7] G. A. Berger, M. Kempe, and A. Z. Genack, "Dynamics of stimulated emission from random media," Phys. Rev. E, **56**(5), 6118, (1997).
[8] L. Ye, C. Zhao, Y. Feng, B. Gu, Y. Cui, and Y. Lu, "Study on the polarization of random lasers from dye-doped nematic liquid crystals," Nanoscale Res. Lett., **12**, 1–8 (2017).
[9] D. Wiersma, "The smallest random laser," Nature, **406**(6792), 133–135(2000).
[10] D. S. Wiersma and S. Cavalieri, "A temperature-tunable random laser," Nature, **414**(6865),708–709 (2001).
[11] S. Murai, K. Fujita, T. Hirao, K. Nakanishi, K. Hirao, and K. Tanaka, "Scattering-based hole burning through volume speckles in a random medium with tunable diffusion constant," Appl. Phys. Lett., **93**(15), 151912 (2008).
[12] R. C. Polson and Z. V. Vardeny, "Random lasing in human tissues," Appl. Phys. Lett., **85**(7), 1289–1291, (2004).
[13] Q. Song et al., "Random lasing in bone tissue," Opt. Lett., **35**(9) ,1425–1427 (2010).
[14] L.-W. Li and L.-G. Deng, "Random lasing from dye-doped chiral nematic liquid crystals in oriented and non-oriented cells," Eur. Phys. J. B-Condensed Matter Complex Syst., **86**(3), (2013).
[15] H. Cao, "Lasing in random media," Waves in random media, **13**(3), R1(2003).
[16] H. Cao, Y. G. Zhao, S. T. Ho, E. W. Seelig, Q. H. Wang, and R. P. H. Chang, "Random laser action in semiconductor powder," Phys. Rev. Lett., **82**(11),2278(1999).
[17] C. T. Dominguez, M. de A. Gomes, Z. S. Macedo, C. B. de Araújo, and A. S. L. Gomes, "Multi-photon excited coherent random laser emission in ZnO powders," Nanoscale, **7**(1), 317–323 (2015).
[18] X. Xu, W. Zhang, L. Jin, J. Qiu, and S. F. Yu, "Random lasing in Eu $^{3+}$ doped borate glass-ceramic embedded with Ag nanoparticles under direct three-photon excitation," Nanoscale, **7**(39),16246–16250 (2015).
[19] A. L. Moura, V. Jerez, L. J. Q. Maia, A. S. L. Gomes, and C. B. De Araújo, "Multi-wavelength emission through self-induced second-order wave-mixing processes from a Nd3+ doped crystalline powder random laser," Sci. Rep., 5(1),1–7 (2015).
[20] Y. Wang, X. Yang, H. Li, and C. Sheng, "Bright single-mode random laser from a concentrated solution of π-conjugated polymers.," Opt. Lett., **41**(2), 269–272 (2016).
[21] R. C. Polson, A. Chipouline, and Z. V. Vardeny, "Random lasing in π-conjugated films and infiltrated opals," Adv. Mater., **13**(10), 760–764 (2001).
[22] L. Wang, Y. Wan, L. Shi, H. Zhong, and L. Deng, "Electrically controllable plasmonic enhanced coherent random lasing from dye-doped nematic liquid crystals containing Au nanoparticles,"Opt. Express, **24**(16), 17593–17602 (2016).
[23] J.-L.Zhu et al., "Random laser emission in a sphere-phase liquid crystal," Appl. Phys. Lett., **106**(19), 191903 (2015).
[24] Z. Wang et al.,"Controlling random lasing with three-dimensional plasmonic nanorod metamaterials," Nano Lett., **16** (4), 2471–2477 (2016).
[25] T. Zhai et al.,"Random laser based on waveguided plasmonic gain channels," Nano Lett., **11**(10), 4295–4298 (2011).
[26] D. Huang et al.,"Low threshold random lasing actions in natural biological membranes," Laser Phys. Lett., vol. **13**(6),65603(2016).
[27] F. Lahoz et al., "Random laser in biological tissues impregnated with a fluorescent anticancer drug," Laser Phys. Lett.,**12**(4),45805 (2015).
[28] L. Ye et al.,"Random lasing action in magnetic nanoparticles doped dye solutions," Opt. Commun., **340**,151–154 (2015).
[29] F. S Abbas and N. F Ali, "Study the optical characteristics of epoxy panel doped with fluorescein-sodium dye," J. kerbala Univ.,**10**(2),50–60 (2014).

[30] H. Cao et al., "Ultraviolet lasing in resonators formed by scattering in semiconductor polycrystalline films," Appl. Phys. Lett.,**73**(25), 3656–3658, (1998).
[31] A. G. Ardakani and P. Rafieipour, "Random lasing emission from WO_3 particles dispersed in Rhodamine 6G solution," Phys. B Condens. Matter, **546**,49–53(2018).
[32] S. Rahayu, A. T. Dosi, and P. Wulandari, "Optimization of metal nanoparticles concentration in dye solution to enhance performance of dye sensitized solar cells," in Journal of Physics: Conference Series, **2243**(1), 12090 (2022).

دراسة تأثير جسيمات السليكا النانوية على خصائص عدة صبغات لتصنيع وسط كسب ليزر عشوائي

نور ياسر خضير* , محمد كريم ظاهر

معهد الليزر للدراسات العليا، جامعة بغداد، بغداد، العراق

*البريد الالكتروني للباحث:Noor.Yasir2101m@ilps.uobaghdad.edu.iq

الخلاصة: تم تصنيع وسائط كسب الليزر العشوائي من انواع مختلفة من الصبغات كمادة مضيفة نشطة وجسيمات اوكسيد السيليكون النانوية (السيليكا SiO_2) كمراكز تشتت من خلال تقنية السول- جل. تم فحص العينات المعدة عن طريق استخدام التحليل الطيفي للأشعة المرئية وفوق البنفسجية , التحليل الطيفي الفلوري , طيف المجهر الإلكتروني لمسح الانبعاث الميداني (FESEM) ، و طيف حيود الأشعة السينية المشتتة للطاقة (EDX). أظهرت النتائج النهائية ان الصبغات المشوبة بجسيمات السيليكا النانوية بتركيز 0.0016 mol/ml لها امتصاص اقل واطياف فلورة اعلى من الصبغات النقية , و كشفت فحوصات FESEM أن مورفولوجيا السيليكا النانوية هي عبارة عن مجموعات من الجسيمات الكروية النانوية الحجم (25–67 nm) . تم استنتاج أن الصبغات المختلفة التي تحتوي على SiO_2 كمركز تشتت يمكن اقتراحها في بناء اوساط كسب ليزرية.

IJL, Issue 2, Vol. 22, 2023 **Research Article**
https://doi.org/10.31900/ijl.v22i2.408

Evaluation of Lithium Disilicate Surface Morphology Treated with Er,Cr:YSGG and Fractional CO_2 Laser

Noor Azad Mohammed[1,*], Zainab F. Al-Bawi[1], Balsam Saadi Abdulhameed[2]

[1]*Institute of Laser for Postgraduate Studies, University of Baghdad, Baghdad, Iraq*
[2]*Al-Imamen Al-Kadmen Medical City, Ministry of Health, Baghdad, Iraq*
** Email address of the Corresponding Author: Nour.Azad1202a@ilps.uobaghdad.edu.iq.*

Article history: Received 24 July 2023;Revised 20 Aug 2023; Accepted 11 Sept 2023; Published online 15 Dec2023

Abstract: The use of indirect, all-ceramic restorations has grown in popularity among dentists. Studies have demonstrated that for indirect ceramic restorations to be effective over time, cement and ceramic must be bonded in a stable manner. Chemical, mechanical, and laser irradiation are among the methods used to precondition ceramic surfaces in order to increase bond strength.
The objective of the study: This study was performed to investigate the roughness values and surface topography of lithium disilicate glass-ceramic treated with conventional methods and different Er,Cr:YSGG, and fractional CO_2 laser conditioning parameters.
Material and methods: Sixty samples of lithium disilicate glass-ceramic were divided as follows: 1- (n = 10) untreated; 2- (n = 10) Hydrofluoric acid etched; 3- (n = 10) conditioned by Er,Cr: YSGG laser at (7 W, 25 Hz, 50/50% Water/Air, pulse duration 60 us, irradiation time 2 min); 4- (n = 10) conditioned by Er,Cr:YSGG laser at (5 W, 25 Hz, 50/50% Water/Air, pulse duration 60 us, irradiation time 2 min); 5- (n = 10) conditioned by fractional CO_2 laser at (power 8 W, pulse duration 10 ms); 6- (n = 10) conditioned by fractional CO_2 laser at (power 6 W, pulse duration 10 ms). Then evaluated by: Profilometer, and scanning electron microscopy.
Results: The highest roughness values were found in CO_2 laser power 8 W treated samples, followed by Er,Cr:YSGG laser power 7W treated samples. The hydrofluoric acid-etched samples showed roughness values comparable to those of CO_2 laser-irradiated samples with a power of 6 W. The untreated sample showed the smoothest surface with the lowest roughness value.
Conclusion: The application of Er,Cr:YSGG, fractional CO_2 lasers enhances the surface roughness of lithium disilicate samples positively, showing the promised results of using these parameters in bonding procedures.

Keywords: laser, surface treatment, ceramics.

1. Introduction

In order to restore the enamel, dentin, structural support, protection, and physical integrity, current glass ceramic fixed dental prostheses take advantage of and benefit from combining the features of crystalline ceramics with those of glasses. They help to bridge the gap between synthetic and realistic aesthetics while

performing an essential function in oral rehabilitation. Contrary to restorations made of metal, polymer-based (Lien et al., 2015). All ceramic restorations have been developed in response to the rising need for aesthetics in restorative dentistry due to their superior esthetic metal-free properties.

Many modern dental indirect restorations are made of lithium disilicate (LD) glass ceramics. Using the hot press method, lithium disilicate ceramics have a better potential for restoration thanks to their translucent and aesthetically pleasing properties than zirconia.

In comparison to leucite-reinforced glass ceramics, the flexural strength of lithium silicate ceramics is significantly higher with better mechanical strength, including fracture toughness, chemical endurance, and abrasion resistance (Alkhudhairy et al., 2020). These properties are provided to ceramics by the crystals in lithium disilicate. However, ceramics' poor physical and bonding qualities continue to be an issue. With such widespread application, it is crucial that dental ceramic and resin composites bond securely and reliably; both micromechanical attachment and chemical bonding via a silane coupling agent are common ways of forming this connection. In order for indirect ceramic-bonded restoration or direct ceramic repair to last and look good in the mouth, etching the ceramic surface properly is a must. The surface energy of ceramics and their bonding potential to resin are both altered by acid etching, which also enhances their wettability (Colares et al., 2013).

There are different surface treatment techniques for ceramic's internal surface to create micro-porosities for increasing the surface area and improving the bonding between the restoration and the dental structure. Lithium disilicate ceramics can undergo a number of different surface treatment processes, including hydrofluoric acid etching, sandblasting, and laser irradiation. Etching using hydrofluoric acid is the gold standard for preparing the intaglio surface of glass ceramics.

Ceramic crystalline structures exposed after being etched using hydrofluoric acid, by dissolving and removing the glassy matrix, hydrofluoric acid etchant reveals the elongated crystals of lithium disilicate ceramic, which in turn generate irregularities, peaks, and valleys on the surface. The nature of the ceramic can be changed if the acid etch concentration and/or etching time are increased above what is recommended by the manufacturer. In addition, inappropriate use of the hydrofluoric acid etchant can cause surface micro-defects, grooves, and fissures in lithium disilicate ceramic. Therefore, Lithium disilicate ceramics can be weakened by hydrofluoric acid if the acid is not used correctly per the manufacturer's guidelines (Tarek, 2021).

The capacity of the Er,Cr:YSGG laser to ablate hard dental tissues, as well as its application in different soft tissue treatments, has recently won over trust. The erbium family of lasers has minimal thermal impacts on adjacent tissues because they are well absorbed by hard tissues and water. In addition, it's a conservative, painless, and noninvasive technique employed for dental work. The use of the Er,Cr:YSGG laser for tooth structure conditioning has also been proven to have antibacterial effects. However, the results of laser treatments might vary depending on a number of factors, such as the length of time spent under the beam, the intensity of the beam, the distance between the surface and the laser, and the type of bonding system used (Vohra et al., 2019).

Micro and macro-irregularities are produced by the Er,Cr:YSGG laser because they rely on the principle of microexplosion during tissue ablation. Additionally, ceramic surface conditioning has been achieved with an Er,Cr:YSGG laser [short pulse duration (60 us)] that results in surface roughness analogous to acid etching. Because HF acid is toxic to patients and cannot be administered intraorally for ceramics, the use of the Er,Cr:YSGG laser is advocated as a more bioacceptable, safe, and straightforward approach to surface modification (Muhammed and Jawad, 2021).

The carbon dioxide laser (CO_2) is frequently utilized intraorally, particularly for soft tissue and hard tissue applications. Because ceramic absorbs nearly the entire wavelength of CO2 laser light, the CO_2 laser is ideally suited for the surface treatment of ceramic materials. CO_2 laser ablation may be an efficient method for conditioning surfaces, thereby improving micromechanical retention and bond strength. The heat initiation of ceramic surfaces by focusing a CO2 laser causes conchoidal fissures, which are the result of surface warming. It is believed that these fractures contribute to the mechanical retention between resin composite and ceramic restorations (Ergun Kunt and Duran, 2018).

The evidence for the role of lasers in the surface conditioning of LD is not yet fully clear. In addition, there is no agreed-upon, standardized procedure for optimizing the laser's power, treatment time, or frequency when it comes to ceramic conditioning. Further, lasers work by surface ablation. (Faris and Al-janabi, 2023). Aiming that the use of Er,Cr:YSGG, and fractional CO_2 laser for surface conditioning of LD ceramics with its modified power, frequency, time, and water/air ratio may show superior or similar results on the surface treatment to the typical usage of HF acid.

2. Material and Method

Sixty IPS E.max 4 mm in diameter and 4 mm in height (4x4x4 mm) cylindrical lithium disilicate glass-ceramic specimens (Ivoclar Vivadent, Schaan, Liechtenstein) were heat-pressed per the manufacturer's instructions. There were no glazing procedures performed on sample surfaces. Underwater chilling, the samples' surfaces were smoothed and polished with silicon carbide paper of 1200 grit by a polishing machine (Laryee Technology Co., Beijing, China). The sample was then placed in an ultrasonic device for 10 minutes to eliminate any impurities or detritus prior to surface conditioning and air drying. At this point, samples were assigned randomly to six groups, each group (n = 10), as follows:

Group 1: In this group (the control group), no surface treatment was applied.

Group 2: The samples' surfaces were etched for 90 seconds with 95% (Pisco Porcelain Etchant, USA) and cleansed with distilled water for 10 seconds to remove any remaining acid, the samples were then air-dried by dental triple syringe.

Group 3: The ceramic surfaces were treated with Er:Cr.YSGG laser irradiation (Millennium, Biolase Technology Inc., San Clemente, CA, USA) using the following laser parameters under air and water spray: Configuration: power = 7 W, wavelength = 2.78 um, 25 Hz W/A 50/50%, pulse duration 60 us, irradiation time (2 min) in sweeping motion. The laser conducting tip was positioned perpendicular to the sample surfaces at a one-millimeter distance fixed by a computer numerical control machine (CNC), using a gold handpiece, 6 MZ um laser tip. The samples were then placed in an ultrasonic device for 5 minutes and air-dried.

Group 4: The ceramic surfaces were treated with Er:Cr.YSGG laser irradiation (Millennium, Biolase Technology Inc., San Clement, CA, USA) under air and water discharge with the following laser parameters: power setting = 5 W, wavelength = 2.78 um, 25 Hz W/A 50/50%, pulse duration 60 us, irradiation time (2 min) in sweeping motion. The laser conducting tip was positioned perpendicular to the sample surfaces at a one-millimeter distance fixed by a computer numerical control machine (CNC), using a gold handpiece, 6 MZ um laser tip. The samples were then placed in an ultrasonic device for 5 minutes and air-dried.

Group 5: The ceramic surfaces were treated with a fractional CO_2 laser system (CO_2 Fractional Laser, Brochure, JHC1180, China) using the following laser parameters: power = 8 W, wavelength = 10.6 um, pulse duration 10ms, interval 2ms, distance 0.2 mm, two scanning, irradiation area corresponds to the face of the ceramic cylinder with a diameter of 4 mm.
A custom-made Teflon mold was used to hold the ceramic samples and for fixation the articulating arm of the laser device during the scanning process.

Group 6: The ceramic surfaces were treated with a fractional CO_2 laser system (CO_2 Fractional Laser, Brochure, JHC1180, China) using the following laser parameters: power = 6 W, wavelength= 10.6 um, pulse duration 10ms, interval 2ms, distance 0.2 mm, two scannings, irradiation area corresponds to the face of the ceramic cylinder with a diameter of 4 mm.

A custom made teflon mold was used to hold the ceramic samples and for fixation the articulating arm of the laser device during the scanning process.

3. Procedure

A profilometer (surface roughness device) (SRT-6210, China) measured the surface roughness of each specimen before and after the conditioning procedure. For each sample, three readings were obtained, and the average value was calculated and considered. Surface topography evaluation by scanning electron microscopy (SEM) was performed on representative samples from each study group.

4. Statistical analysis

Data analysis and description were performed using Statistical Package for Social Science (SPSS version 26). The values of roughness were statistically evaluated using a one-way ANOVA test, and these values were shown to have a normal distribution by the Shapiro-Wilk test. The P-value was equal to 0.05, regarded as significant.

5. Results

The data on surface roughness for the six study groups that had been collected showed higher statistical significance than the control group. The mean of groups 2, 3, and 6 was (1.220 ± 0.149, 1.233 ± 0.137, 1.131 ± 0.159) respectively with $P < 0.001$, showing comparable results. The highest mean of surface roughness was found in group 5 (CO2, power 8 W group), and the control group (untreated) had the lowest one as shown in Fig.1. Table (1,2) specifies the results in detail. Figure 2 shows the difference in the scanning electron microscopy (SEM) images of the surface topography between the control group, hydrofluoric acid etched group, and laser irradiated samples.

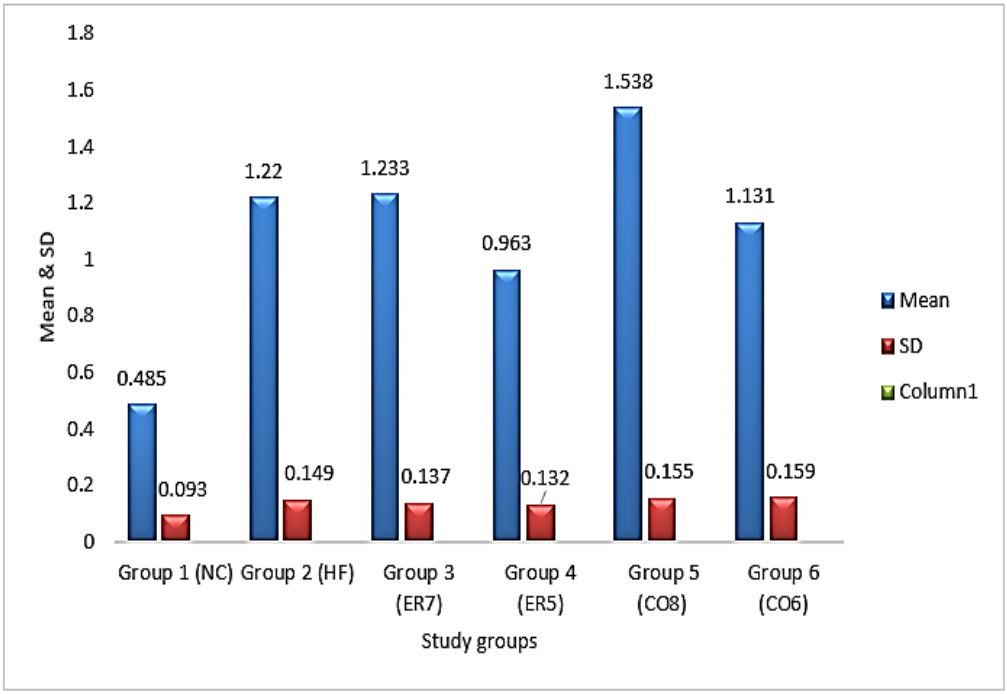

Fig.1: Mean and standard deviation for the surface roughness of the study groups.

Table 1. Descriptive statistics of the roughness values of the study groups.

Study groups	Mean (um)	Standard deviation	Std. error	P-value
Group 1 (NC)	0.485	0.093	0.0625	≤ 0.001 HS
Group 2 (HF)	1.220	0.149		
Group 3 (ER7)	1.233	0.137		
Group 4 (ER5)	0.963	0.132		
Group 5 (CO8)	1.538	0.155		
Group 6 (CO6)	1.131	0.159		

- HS = Highly significant.

Table 2. Descriptive statistics of the roughness values of the study intergroups.

Study groups	Mean difference (um)	Standard deviation respectively	P-value
CN-HF	0.735	0.093 - 0.149	0.000 HS
CN-ER7	0.748	0.093 - 0.137	0.000 HS
CN-ER5	0.477	0.093 - 0.575	0.000 HS
CN-CO8	1.053	0.093 - 0.155	0.000 HS
CN-CO6	0.645	0.093 - 0.159	0.000 HS
HF-ER7	0.013	0.149 - 0.137	0.835 NS
HF-ER5	0.257	0.149 - 0.575	0.000 HS
HF-CO8	0.318	0.149 - 0.155	0.000 HS
HF-CO6	0.089	0.149 - 0.159	0.157 NS
ER7-ER5	0.270	0.137 - 0.575	0.000 HS
ER7-CO8	0.305	0.137 - 0.155	0.000 HS
ER7-CO6	0.102	0.137 - 0.159	0.106 NS
ER5-CO8	0.575	0.132 - 0.155	0.000 HS
ER5-CO6	0.168	0.132 - 0.159	0.01 S
CO8-CO6	0.407	0.155 - 0.159	0.000 HS

- CN = Group 1, HF = Group 2, ER7 = Group 3, ER5 = Group 4, CO8 = Group 5, CO6 = Group 6, HS = Highly significant, S = Significant, NS = Not significant.

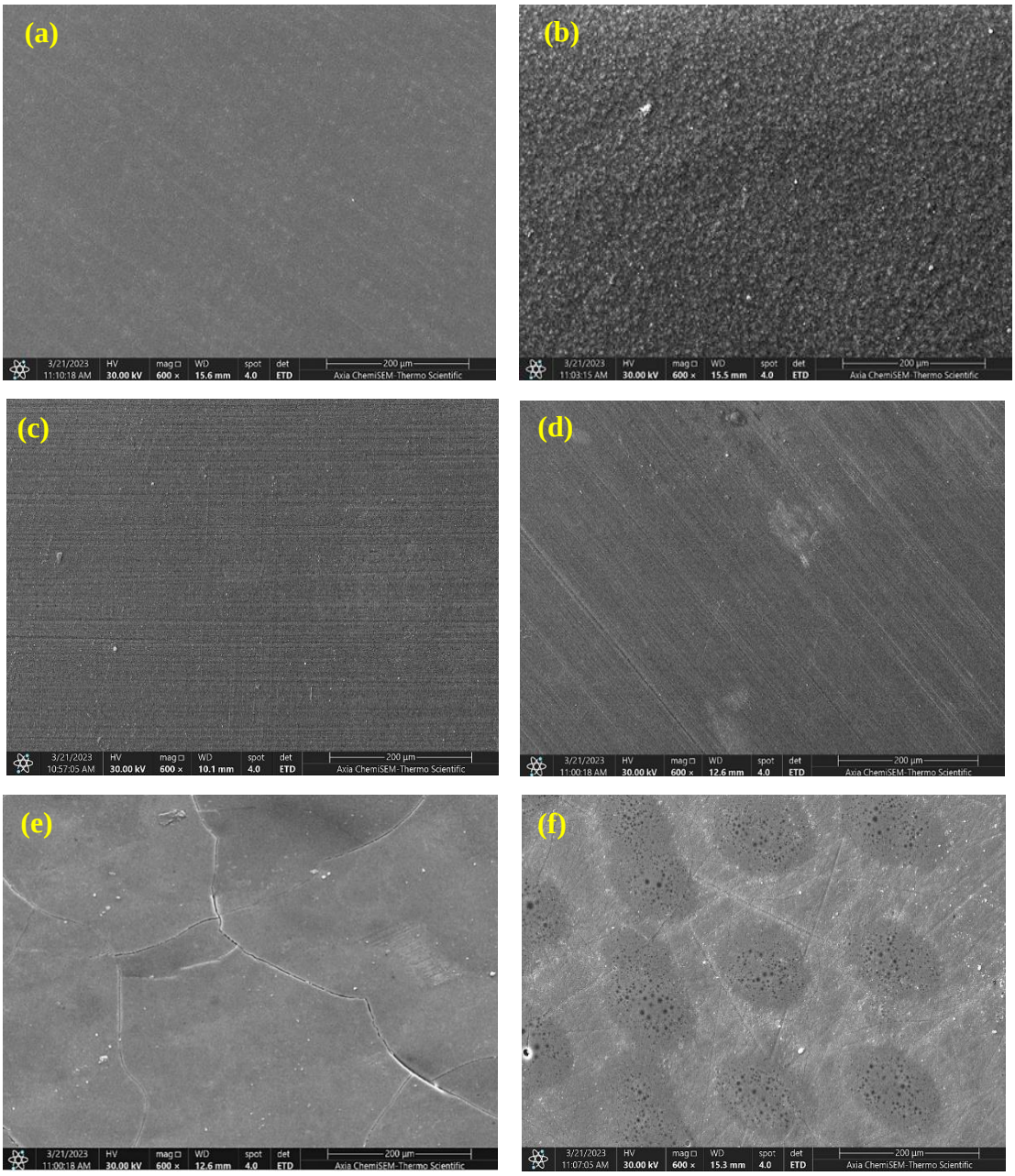

Fig.2: Scanning electron microscopy (SEM) images of the lithium disilicate cylinders at 600X: (A) SEM of untreated sample; (B) SEM of acid etched sample); (c) SEM of laser irradiated (Er,Cr:YSGG) sample, power 7 w; (D) SEM of laser irradiated (Er,Cr:YSGG) sample, power 5 w; (E) SEM of laser irradiated (CO_2) sample power 8 w; (F) SEM of laser irradiated (CO_2) sample power 6 w.

6. Discussion

The assumption was that using laser (Er,Cr:YSGG, fractional CO_2) to condition the surface of lithium disilicate would be superior or equal to using HF.

For optimal adhesion and bonding of ceramics for restorative purposes, inert surfaces must be prepared. There are many ways to accomplish this, including grinding, abrasion with rotary tools (diamond), and abrasion with airborne particles (Al_2O_3), Which provide acceptable bonding despite possible negative

effects that cause irreversible changes in the ceramic's surface. Acid etching includes orthophosphoric and hydrofluoric acid, although its usage is constrained by negative effects such as dissolving ceramic's glaze layer, it attacks the glassy phase of ceramics, dissolving the surface to a depth of a few micrometers and as a result, LD crystal protrudes from the glassy matrix (Mohammed and Ali, 2020). It's difficult to apply in the mouth cavity and it has the potential for tissue damage. In addition to these methods, laser irradiation is also used, as are combinations of two or more of these roughening methods (Mirhashemi et al., 2017).

The resulting altered topography increased the surface area for micromechanical bonding. Laser systems have been the subject of substantial research and development due to their ease of use, safety, and increased efficiency. It was shown that the etching precision of Er,Cr:YSGG laser can be affected by the distance of the laser's head from the irradiated surface. To achieve the best results, the optimal distances were determined to be 1 mm for Er,Cr:YSGG (Alhassani and Jawad, 2018). This recommendation was taken into account in this investigation. An earlier study found that using the Er,Cr:YSGG laser at 0.5 W, 10 Hz, pulse duration 230 us ($22.83 \pm 5.07, P < 0.01$) was less effective than using hydrofluoric acid (28.15 ± 4.72 MPa, $P < 0.01$) (Al Rifaiy, 2018). It's interesting to note that extended laser application increases surface roughness, yet the laser generates excessive heat, weakening and overly destroying the surface. Therefore, longer-term laser-treated ceramics showed stronger bond strengths, although somewhat lower than HF (Alkhudhairy et al., 2020). Additionally, there was no discernible difference between the use of the 1.5 W, 10 Hz (27 ± 0.9, $P < 0.001$) and 2.5 W, Hz, time 60 s (21 ± 0.85, $P < 0.001$) on the ceramic materials; both showed noticeably lower mean values than the HF acid-etched treated samples (Mandil et al., 2020). Therefore, higher power was used in this study.

In this study, an examination of the effect of laser surface irradiation on ceramic samples was done by SEM and a profilometer. Also, Er,Cr:YSGG irradiated samples with power 5 W,25 Hz have a uniform smooth surface topography opposite to the acid-etched samples; this disagrees with (Alqerban et al., 2021), who speculated that comparable bond strength treated by Er,Cr:YSGG at 4.5 W, 30 Hz (17.09 ± 1.114, $P > 0.05$) to HF (17.85 ± 1.25, $P>0.05$) is due to the formation of micro-depths and abrasion on the LDC surface.

The Er,Cr:YSGG laser-irradiated samples (power 5 W, 25 Hz) resulted in the lowest Ra value correlating with (Kursoglu et al., 2013), Who hypothesize that the usage of Er:Cr.YSGG laser at 6 W, time 60 s (3.59 ± 1.19, $P > 0.05$) may not be an effective surface treatment technique. Although the use of high power may affect the ceramic surface negatively, the high power (7 W, 25 Hz) Er,Cr:YSGG laser-irradiated samples that used this power for 2 min resulted in increasing surface roughness which correlates with higher bond strength values, correspond with those of (Vohra, Fahim, et al., 2019) using (7 W, 25 Hz, time 2 min.) with a mean and standard deviation of bond strength (19.95 ± 1.014, $P < 0.001$). Repeated applications with low frequency, high power, and longer duration laser parameters are proposed to be more effective in enhancing the roughness and the bonding integrity of ceramic specimens since it is known that laser characteristics can precisely affect the outcome of Er,Cr:YSGG applications. The Er,Cr:YSGG laser ablates tissues using the principle of micro-explosion, resulting in microscopic and macroscopic irregularities (Albaker et al., 2020). In addition, it was found that the mean of surface roughness increased with both the power and duration of the laser treatment. Yet bond strength may decrease at high power due to surface degradation and weakening. Moreover, inadequate micro-depth generation, severe degradation of the matrix phase, or the heat-damaged layer may all contribute to affecting the roughness and the bond strength of laser-prepared ceramic surfaces.

Previous research may have employed inconsistent values for laser power, which may explain the conflicting findings. In contrast to a study by Kursoglu et al., which compared 6 W to 1.5 and 2.5 W, this study increased the power from 5 W to 7 W. In addition, the application period in this study was longer than that of (Kursoglu et al., 2013, Gökçe et al., 2007). The fractional CO_2 laser can increase micromechanical retention and bond strength by roughening the surface via the process of thermomechanical ablation. The use of fractional CO_2 lasers is associated with other benefits, such as the fact that the emission wavelength of the CO_2 laser is almost completely absorbed by ceramics, it is ideally adapted for ceramic surface treatment and scanning the surface by the laser apparatus itself would result in a more homogeneous etching pattern on the ceramic specimen (Ahrari et al., 2017). More research is needed to confirm this assumption.

SEM of the fractional CO_2 groups' surface-treated specimens reveals substance loss and the concentration of hollow depressions at power 6 W, as well as the progressive effect of laser material removal proportional to the parameters and cracks formation at power 8 W. According to SEM analysis, lithium disilicate has a uniform and no cracks on surfaces when irradiated with a 6 W CO_2 laser. This agreed with (El Gamal et al., 2017), who demonstrated that the surface hardness with a CO_2 laser (continuous mode) power 5 W, 60 s was (6.32 ± 0.09, P < 0.0003), Comparing the shear bond strength of irradiated ceramic (16.71 ± 4.04, P = 0.909) to HF acid etched ceramic (16.90 ± 6.42, P = 0.909), revealed no significant differences but confirmed the concept of hydrofluoric acid etching on the surface treatment. It has been reported that whenever focused CO_2 laser beams are used to heat ceramic surfaces, conchoidal tears (typically caused by surface heating) emerge on the surface. The fissures are believed to provide mechanical retention between resin cement and the ceramic surface (Alavi et al., 2021, Zarif Najafi et al., 2014). The fractional CO_2 laser-treated samples at power 8 W have microcracks formation according to the SEM imaging, this may affect the strength of the material in spite of the high surface roughness value and corresponding bond strength. This disagreed with Al Gamal et al., 2017) who reported that 10 W CO_2 laser beams (continuous mode) did not affect microhardness (6.34 ± 0.17, P < 0.0003). Although (AlShahrani et al., 2019) claimed that fractional CO_2 increased the bond strength of ceramics when bonded to a metallic bracket without damaging the surface when using 10 W, 200 Hz, time 60 s,pulse duration 1.75 ms (19.98 ± 2.94, P < 0.05), this was not the case in the present study, as SEM imaging revealed the formation of absolute cracks.

Variations in study outcomes can be attributed to variations in laser parameters, resin cement type, ceramic type, thermocycling procedures, and water storage duration. Blister-like globules and surface cracks on the surface structure of ceramic in laser-irradiated groups lead to increased roughness and greater resin penetration, which may contribute to the micromechanical bond strength in laser-irradiated groups (Hegazy et al., 2016). On ceramic surfaces, the type of laser and the laser's parameters have a significant impact. Since the most important effect of a laser is to convert radiant energy to heat (the thermo-mechanical effect), the most important interaction between the material and laser is the absorption of laser energy by the material's surface (Usumez et al., 2013). To prevent thermal energy from accumulating in surrounding tissue and thereby collateral harm, tissues should be allowed to cool for approximately three times their thermal relaxation time. This can be properly managed (Yeragi et al., 2014).

The in vitro approach used in this study presents certain drawbacks. The outcomes depend on the specific laser used, the parameter, and the ceramic type used in the experiment. The effectiveness of ceramic restorations can also be affected by factors like surface roughness and ceramic strength (which are affected by ceramic heat treatment). For this reason, it is suggested that additional research be conducted utilizing this methodology to examine its effect on the surface roughness and hardness of the ceramic for foreseeable functional results.

7. Conclusions

The application of an Er,Cr:YSSG laser at a power of 7 W enhanced the surface roughness of lithium disilicate samples positively, showing the promised results of using these parameters in bonding procedures of ceramic dental material. The surface treatment by CO_2 laser at 8 W demonstrated roughness values higher than hydrofluoric acid etching with obvious crack formation. The CO_2 laser-irradiated samples at 6 W have comparable Ra values to the HF group.

References

Lien, W., Roberts, H. W., Platt, J. A., Vandewalle, K. S., Hill, T. J. & Chu, T.-M. G. (2015). microstructural evolution and physical behavior of a lithium disilicate glass–ceramic. dental materials, **31**, 928-940.

Alkhudhairy, F., Al-johany, S. S., Naseem, M., Bin-Shuwaish, M. & Vohra, F. (2020). "Dentin bond strength of bioactive cement in comparison to conventional resin cement when photosensitized with er, Cr: YSGG laser". pakistan journal of medical sciences, **36**, 85.

Colares, R. C. R., Neri, J. R., Souza, A. M. B. D., Pontes, K. M. D. F., Mendonca, J. S. & Santiago, S. l. (2013). "Effect of surface pretreatments on the microtensile bond strength of lithium-disilicate ceramic repaired with composite resin". Brazilian Dental Journal, **24**, 349-352.

Tarek, M. (2021). "Effect of er, cr: ysgg laser versus acid etching surface treatment on the surface roughness and topography of two pressable lithium disilicate ceramics."in-vitro study". Egyptian Dental Journal, **67**, 1571-1581.

Vohra, F., Labban, N., Al-hussaini, A., Al-jarboua, M., Zawawi, R., Alrahlah, A. & Naseem, M. (2019). "Influence of ER; CR: YSGG laser on shear bond strength and color stability of lithium disilicate ceramics: an in vitro study. Photobiomodulation", photomedicine, and laser surgery, **37**, 483-488.

Muhammed, F. S. & Jawad, H. A. (2021). "The influence of short pulse er: cr: ysgg laser on the shear bond strength of cad-cam zerconia material to resin cement". Indian Journal of Forensic Medicine & Toxicology, **15**.

Ergun Kunt, G. & Duran, I. (2018)."Effects of laser treatments on surface roughness of zirconium oxide ceramics". BMC Oral Health, **18**, 1-7.

Faris, R. A. & Al-janabi, A. (2023). "Ultrafast lithium disilicate veneer debonding time assisted by a Co2 laser with temperature control". Optics Continuum, **2**, 825-837.

Mohammed, H. A. & Ali, O.S. (2020)."Three-dimensional surface evaluation and shear bond strength of three pre-treatment e-max surfaces for metal and ceramic orthodontic brackets: in vitro study". Polytechnic Journal, **10**, 113-118.

Mirhashemi, A., Sharifi, N., Moharrami, M. & Chiniforush, N.(2017)."Evaluation of different types of lasers in surface conditioning of porcelains: a review article". Journal of Lasers in Medical Sciences, **8**, 101.

Alhassani, l. I. & Jawad, H. A. (2018). "Influence of fractional Co2 laser irradiation on temperature elevation and bonding strength of resin cement to the zirconia ceramic". Iraqi Journal of Laser, **17**, 23-31.

Al rifaiy, M. Q. (2018). "Effect of Erbium-Yttrium, scandium, gallium and garnet (Er-YSGG) laser on the bond strength of lithium disilicate ceramics". Pakistan Journal of Medical Sciences, **34**, 32.

Mandil, S. T., Katamish, H. & Salah, T. (2020). Effect of surface treatment of two ceramic materials by Er, Cr: YSGG laser irradiation on the shear bond strength to resin cement "a comparative in-vitro study". Brazilian Dental Science, **23**, 12 p-12 p.

Alqerban, A. (2021)." Lithium di silicate ceramic surface treated with Er, Cr: YSGG and other conditioning regimes bonded to orthodontic bracket". The Saudi Dental Journal, **33**, 188-193.

Kursoglu, P., Motro, P. F. K. & Yurdaguven, H. (2013). "Shear bond strength of resin cement to an acid etched and a laser irradiated ceramic surface". The Journal of Advanced Prosthodontics, **5**, 98-103.

Albaker, A. M., Al deeb, L., Alhenaki, A. M., Aldeeb, M., Al Ahdal, K., Abduljabbar, T. & Vohra, F. (2020). "Bonding integrity and compressive strength of re-bonded, surface conditioned and Er Cr YSGG laser treated lithium disilicate ceramics". Journal of Applied Biomaterials & Functional Materials, **18**, 2280800020910954.

Gökçe, B., Özpinar, B., Dündar, M., Cömlekoglu, E., Sen, B. & Güngör, M. (2007). "Bond strengths of all-ceramics: acid vs laser etching". Operative Dentistry, **32**, 173-178.

Ahrari, F., Boruziniat, A., Mohammadipour, H. S. & Alirezaei, M. (2017). The effect of surface treatment with a fractional carbon dioxide laser on shear bond strength of resin cement to a lithium disilicate-based ceramic. dental research journal, **14**, 195.

El gamal, A., Medioni, E., Rocca, J. P., Fornaini, C., Muhammad, O. H. & Brulat-bouchard, N. (2017). "Shear bond, wettability and afm evaluations on Co 2 laser-irradiated cad/cam ceramic surfaces. lasers in medical science, **32**, 779-785.

Alavi, S., Samie, S. & Raji, S. A. H. 2021. Comparison of lithium disilicate–reinforced glass ceramic surface treatment with hydrofluoric acid, Nd: YAG, and Co2 lasers on shear bond strength of metal brackets. clinical oral investigations, **25**, 2659-2666.

Zarif Najafi, H., Oshagh, M., Torkan, S., Yousefipour, B. & Salehi, (2014). “Evaluation of the effect of four surface conditioning methods on the shear bond strength of metal bracket to porcelain surface. Photomedicine and Laser surgery”, **32**, 694-699.

El Gamal, A., Rocca, J. P., Fornaini, C., Medioni, E. & Brulat-bouchard, N. (2017). “Microhardness evaluations of cad/cam ceramics irradiated with Co2 or Nd: YAP laser”. Laser Therapy, **26**, 13-18.

Alshahrani, I., Kamran, M. A., Almoammar, S. & Alhaizaey, A.(2019). “Photosensitization of lithium di-silicate ceramic by Er, Cr: YSGG and fractional carbon dioxide laser bonded to orthodontic bracket”. Photodiagnosis and Photodynamic Therapy, **28**, 273-276.

Hegazy, S. S., Hashem, A. M. A. Z. & Habib, S. I. (2016). “The efficacy of laser glazing on surface roughness and structure of all-ceramic veneers. Egyptian Dental Journal”, **62**, 1089-1096.

Usumez, A., Hamdemirci, N., Koroglu, B. Y., Simsek, I., Parlar, O. & Sari, T. (2013). Bond strength of resin cement to zirconia ceramic with different surface treatments. lasers in Medical Science, **28**, 259-266.

Yeragi, E., Nalawade, K. P., Gotmare, S., Mahajan, K. & Yeragi, P. (2014). Laser physics& its application in dentistry–a review. IOSR journal of Dental and Medical Sciences, **18**, 33-46.

تقييم سطح تركيبات الايماكس المعالجة بليزرات الاربيوم كروميوم و ثنائي اوكسيد الكاربون الجزيئي

نور آزاد محمد صالح[1]*، زينب فاضل الباوي[1] , بلسم سعدي عبد الحميد[2]

[1]معهد الليزر للدراسات العليا, جامعة بغداد, بغداد, العراق
[2]مدينة الامامين الكاظمين الطبية, وزارة الصحة العراقية, بغداد, العراق

*البريد الالكتروني للباحث:Nour.Azad1202a@ilps.uobaghdad.edu.iq

الخلاصة الخلفية و المعلومات : ازداد استخدام تركيبات الاسنان المصنوعة من السيراميك بكثرة في الاونة الاخيرة في طب الاسنان. حيث اظهرت الدراسات وجوب معاملة سطحها بصورة كيميائية او ميكانيكية او بواسطة التشعيع بالليزر من اجل ثباتيتها لاطول فترة ممكنة ونجاحها. **هدف الدراسة**: هذه الدراسة تهدف الى تقييم خشونة وسمات سطح تركيبات الايماكس (سليكات الليثيوم) بعد معالجتها بالطرق التقليدية اضافة الى استخدام الليزر.**المواد والطرق**: ستون عينة من تركيبات الايماكس قسمت الى ستة مجموعات حيث تركت المجموعة الاولى بدون اي معالجة و عولجت المجموعة الثانية بواسطة حمض الهايدروفلوريك اما المجموعة الثالثة والرابعة فعولجت بأستخدام ليزر الاربيوم كروميوم, ثم عولجت المجموعة الخامسة والرابعة بواسطة ليزر ثنائي اوكسيد الكاربون الجزيئي. **النتائج**: اكبر قيمة لخشونة السطح وجدت في المجموعة المستخدم بها ليزر ثنائي اوكسيد الكاربون الجزيئي بقدرة 8 واط و من ثم المجموعة المستخدم بها ليزر الاربيوم كروميوم بقدرة 7 واط. حيث وجد ان مجموعة حمض الهايدروفلوريك وليزر ثنائي اوكسيد الكاربون ذو القدرة 6 واط لديهما ذات القيمة بالنسبة لخشونة السطح. اما المجموعة الاولى الغير معالجة فقد اظهرت اقل قيمة لخشونة السطح. **الاستنتاج**: لقد نتج عن استخدام ليزرات الاربيوم كروميوم و ثنائي اوكسيد الكاربون الجزيئي نتيجة ايجابية في زيادة خشونة السطح حيث ممكن ان تستخدم مستقبلا في عملية تثبيت تركيبات الاسنان.

IJL, Issue 2, Vol. 22, 2023 **Research Article**
https://doi.org/10.31900/ijl.v22i2.401

D-shape Optical Fiber Development and Enhancement as a Refractive Indices Sensor Using Surface Plasmon Resonance

Hiba Kh. Abbas*, Zainab F. Mahdi

Institute of Laser for Postgraduate Studies, University of Baghdad, Baghdad, Iraq
** Email address of the Corresponding Author: heba.khodair1101a@ilps.uobaghdad.edu.iq*

Article history: Received 8 July 2023; Revised 25 Aug 2023; Accepted 12 Sept 2023; Published online 15 Dec 2023

Abstract: This article showcases the development and utilization of a side-polished fiber optic sensor that can identify altered refractive index levels within a glucose solution through the investigation of the surface Plasmon resonance (SPR) effect. The aim was to enhance efficiency by means of the placement of a 50 nm-thick layer of gold at the D-shape fiber sensing area. The detector was fabricated by utilizing a silica optical fiber (SOF), which underwent a cladding stripping process that resulted in three distinct lengths, followed by a polishing method to remove a portion of the fiber diameter and produce a cross-sectional D-shape. During experimentation with glucose solution, the side-polished fiber optic sensor revealed an adept detection sensitivity of 0.2015 au. /RIU. In order to improve sensitivity, a recent sensor was subjected to a coating process utilizing a thin film layer of gold (Au) measuring a thickness of 50 nm. The sensor was subsequently subjected to a series of tests utilizing the same glucose solutions as in previous experiments. A notable enhancement in sensitivity was observed when utilizing gold as the sensing material, with an equivalent maximum sensitivity of 3.101 au. /RIU.

Keywords: D-shaped fiber, fiber sensor, refractive index, gold nano-layer, surface plasmon.

1. Introduction

There has been a growing interest in using optical fiber technology for refractive index (RI) measurements in recent years because of the significant benefits it offers over traditional sensor technologies. There are numerous benefits provided by this technology, such as swift reaction time, small dimensions, reliable and secure operation, adaptability, the ability to be remotely monitored, and adeptness in handling challenging conditions [1]. The main techniques used to measure RI, an optical phenomenon, are fiber Bragg gratings [2], fiber ring laser [3], tapered multimode optical fiber [4], single mode-coreless-single mode (SCS) fiber [5], fiber-based surface Plasmon resonance [6], Most fascinating strategies for detecting surface Plasmon stimulation are those based on surface plasmon resonance (SPR), which are extremely sensitive to changes in the refractive index (RI) of their surroundings [7-8]. Significant work has been expended in recent years to alter a D-shaped fiber optic to use in SPR sensors. Jing Zhao et al. (2016) The researchers examined the

sensor performance reduction brought on by the degradation of the silver coating while also demonstrating a surface plasmon resonance refractive sensor based on a single-mode optical fiber that has been side-polished. The sensor was quick to react with liquids with refractive indices between 1.32 and 1.40 RIU [9]. Zakaria et al. (2017) examined the modeling and fabrication of a D-shaped fiber optic for SPR sensors. Methods for designing the SPR D-shaped fiber sensor are presented in this study, both computational and experimental, which include two setup approaches: finite element simulation and experimental methods. The experimental findings are highly correlated to the modeled results [10]. D-shaped, silver-coated, graphene-encased sensors were conceptualized and theoretically explored by Arthor A. Melo. et al. (2018). The proposed sensor achieves its best performance between 1.33 and 1.35 RIU with reduced sensing area lengths and higher polished thicknesses [10]. In 2019, Li-Ye N. et al. developed & tested a gold nanoparticle–Au layer–interacting optical fiber sensor in a D shape with a big core. In the area of refractive index (1.3332–1.3710 RIU), the SPR sensor was enhanced with gold nanoparticles (Au NPS) [12].

In this study, the goal was to enhance efficiency by applying a layer of gold 50 nm thick to the D-shaped fiber's sensing region. we develop a simple but efficient D-shape multimode fiber sensor for RI detection in a glucose solution. The samples were initially evaluated, and the findings were recorded using a D-shaped fiber sensor with a section of stripped fiber cladding as the detecting zone. After that, a 50-nm coating of gold (Au) was added to the initial sensor to increase its sensitivity. To determine the sensor's sensitivity throughout the glucose RI range of 1.334 to 1.346 RIU, the effect of the length of the stripped cladding portion is also examined. The benefits of this type of sensor are its ease of use, low cost, broad dynamic range, and good sensitivity at RI values below but near to the fiber core's RI value.

2. Fabrication of D-shaped Fiber Sensor

A schematic configuration of an optical fiber sensor in the D-shape, according to Fig.1(a). Thorlabs', step-index, and multimode silica optical fibers were used to fabricate a D-shaped fiber sensor with silica core 400 μm and fluorinated polymer cladding 25μm. In the visible spectrum, silica exhibits a refractive index of approximately 1.45, while the fluorinated polymer's refractive index is around 1.40. Initially, a collection of fiber specimens was sliced using a specialized tool to achieve 15 cm segments. In order to get ready for the polishing process, a small section in the middle of the fiber covering was taken off using an Ls sensing region (1 cm, 1.5 cm, 2 cm).

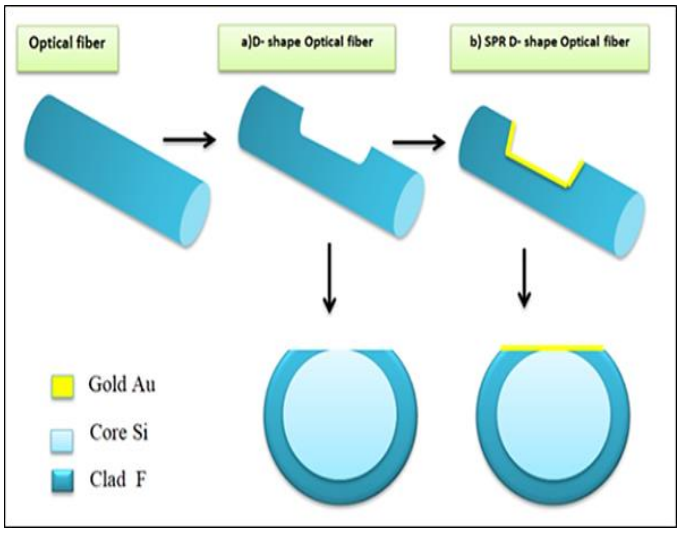

Fig.1: The steps included in the schematic design for the following sensors: a) D-shape fiber sensor; and b) SPR D-shaped fiber sensor.

This section was then fixed onto a slide that had a slot using epoxy. By repeatedly refining the sensor with 6 μm grit-sized polishing sheets (specifically Thorlabs sheets), the entire detection area of the sensor was manually polished along its entire length [15]. After each polishing stage, the sensing zone's surface was examined with a Novel NMM-800 optical microscope to estimate its average thickness. The SPR D-shaped fiber sensor has been achieved by coating Au-film on a polished fiber surface with a Quorum Tech Q150RES magnetron sputtering system. The plan is to utilize the sputter coating setup to cover thin layers of gold measuring 50 nm as shown in Fig.1(b) [16].

The refractive index of a liquid can be measured using a D-shape optical fiber sensor based on the evanescent field. As shown in Fig.1(a), the basic structure of a D-shape optical fiber sensor consists of a core, cladding, and sensing medium at the polishing area. The guiding light depends on the total internal reflection phenomenon at the core-cladding interface and produces an evanescent wave that travels along the core-cladding interface. In the sensing zone, this ephemeral field decreases at an exponential rate [20]. As a result of these characteristics. To improve the sensitivity of the D-shaped optical fibers sensor a gold nanofilm is deposited on the core-cladding interface, as shown in Fig.2(b). A D-shaped optical fiber sensor based on the SPR principle has been developed. When incident light strikes a continuous metal film at just the right angle, it will be totally reflected back into its source. Surface plasmon resonance (SPR) is excited when an evanescent wave penetrates a metal, and the location of the SPR's wavelength is dependent on the refractive index (RI) [21].

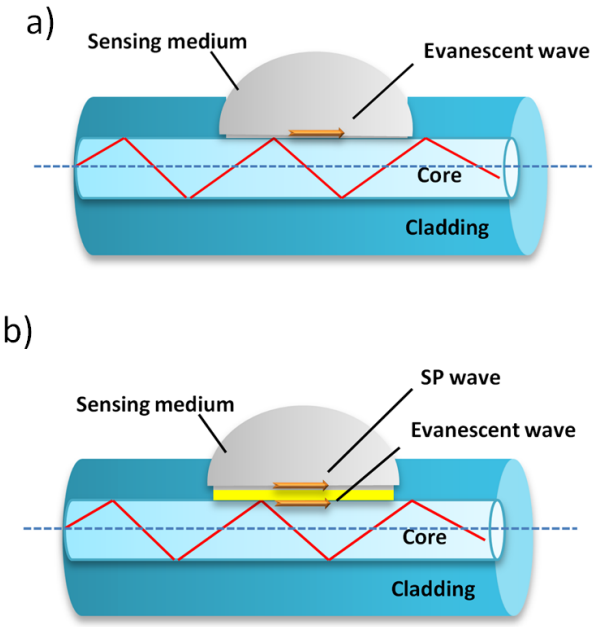

Fig.2: The schematic structure of a) D-shape fiber sensor; and b) SPR D-shape fiber sensor

3. Experiment Setup

Figure 3 depicts the test setup for RI detection using a D-shape optical sensor. The source of light for the experiment was an NKT Photonics ultra-compact white light laser. To select the 650 nm laser light, Thorlabs multi-mode fiber optic filter/attenuator was used. Thorlabs, a PM100 USB power meter was used to measure how much energy was being emitted or absorbed by the fiber optic sensor element, and the data was processed in software. The sensors' refractive index sensing experiments were performed in refractive index areas (1.334-1.346 RIU) using two sensors to compare and evaluate their sensitivity and linearity and select the most efficient sensor. The refractive indices of the investigated solutions were determined using a hand-hold "pocket" refractometer. At constant temperature, Fig.4 depicts the connection between a

solution's concentration and the refractive indices of its component parts. Refractive index and concentration are directly proportional, meaning that as material solution concentration increases, so does refractive index.

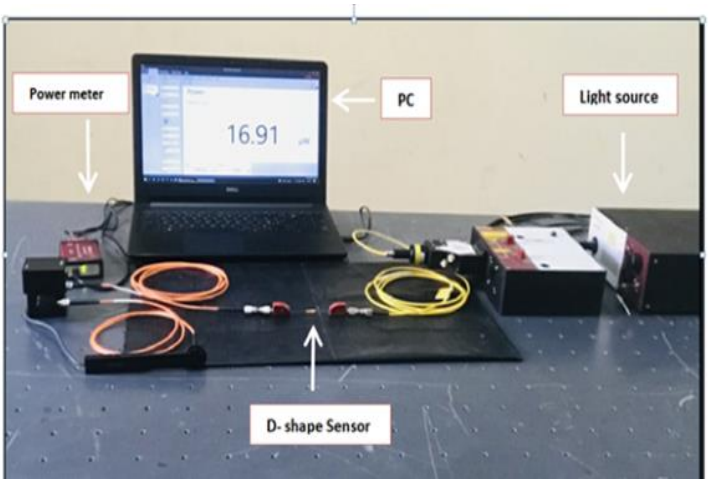

Fig. 3: Experimental setup device for IR sensor measurement.

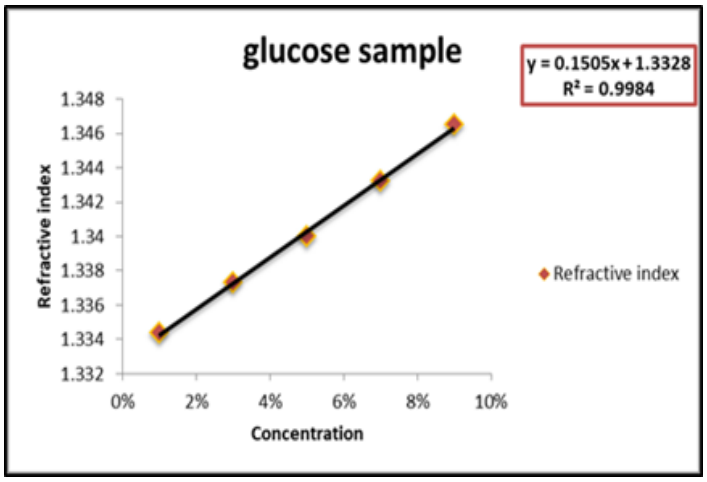

Fig. 4: The concentration of a glucose solution affects the solution's refractive index.

.

4. Results and Discussion

4.1 Optical Microscope Image and Energy Dispersive Spectroscopy spectra

Figure 5 depicts the photo image and optical microscopy representations of a D-shape fiber sensor both prior to subsequent to its coating with Au, with a magnification of 5X. The SPR D-shaped fiber sensor was analyzed using energy dispersive X-ray spectroscopy (Axia Chemi) SEM. This innovative method combines the use of data from scanning electron microscopy (SEM) as shown in Fig.6, and energy-dispersive X-ray spectroscopy (EDS). Figure 7 depicts the EDS spectra, which exhibit the existence of a multitude of elements in the specimen, namely fluorine F, silicon Si, gold Au, oxygen O, and carbon C, along with their individual atomic number and mass, as illustrated in Table 1.

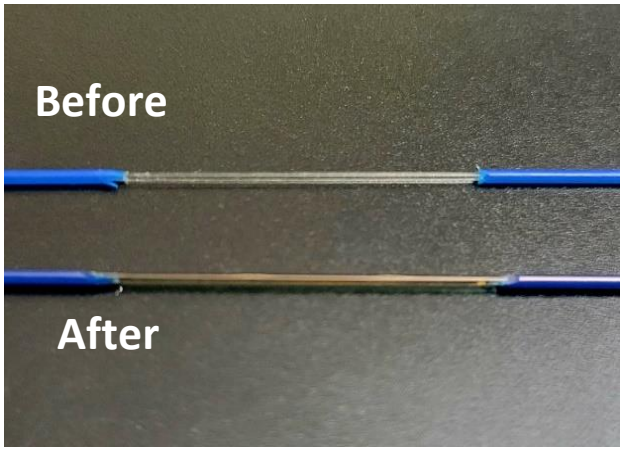

(a)

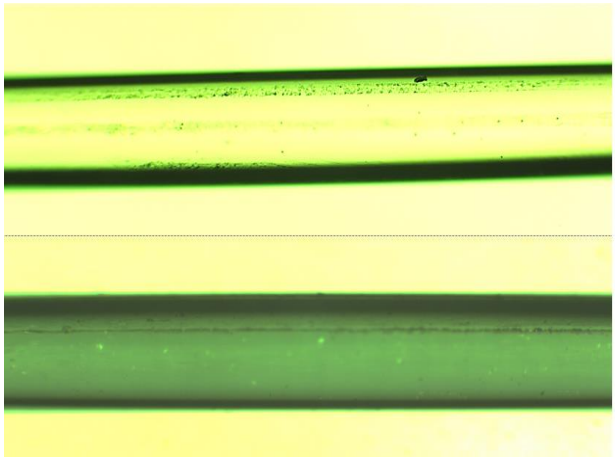

(b)

Fig.5: a) The photo image and b) Optical microscopy images, before and after Au coating, of a D-shaped fiber sensor.

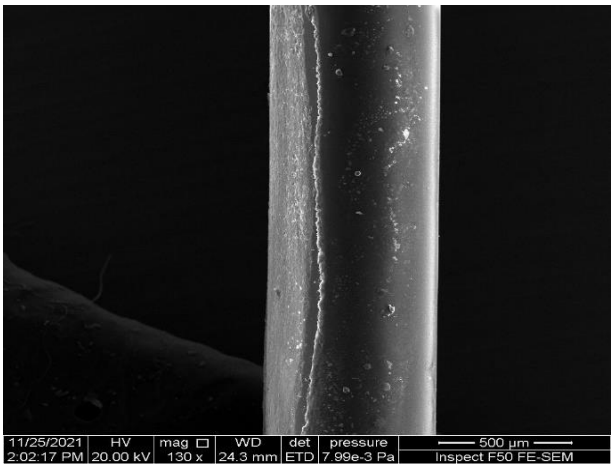

Fig.6: D-shaped SPR fiber sensor SEM image.

Table 1: EDS data for SPR D-shape fiber sensor elements.

Element	Atomic %	Weight %
C	62.7	53.8
O	23.6	27.0
F	13.7	18.6
Au	0.0	0.6
Totals	100.0	100.0

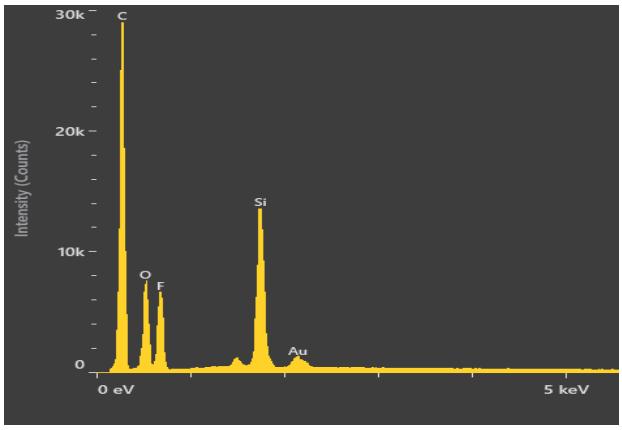

Fig.7: Sensor EDS spectra for SPR D-shaped fibers.

4.2 A D-shape fiber sensor's performance

Figure 8 plots the normalized intensity against the glucose solution's refractive index for all the D-shape fiber sensors that were examined as the sensors interact with the surrounding medium outside the fiber core, the normalized intensity rises linearly with increasing RI in the range of (1.334 to 1.346) RIU.

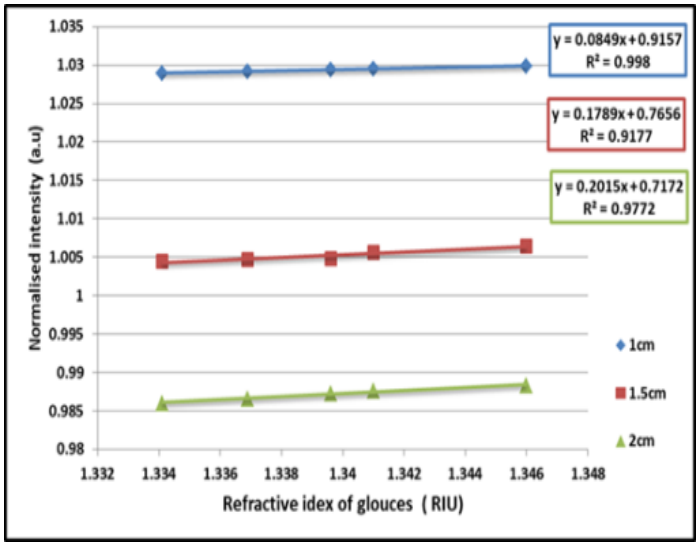

Fig. 8: Intensity normalized by sensing length for D-shaped fiber sensors.

The glucose solution will stop the evanesces wave from exiting the fiber because the surrounding medium's refractive index has increased, which acts as an optical fiber cladding .

4.3 SPR D-shaped fiber sensor performance

Here, a D-shaped fiber covered with Au nanofilm senses the refractive index (RI) of the glucose solution. A gold nano-film is required for a surface plasmon resonance-based detection technique. This film must be exposed to both incident and absorbed light for detection to be possible, and detection is defined by the detected light intensity.
Normalized intensity and corresponding refractive indices for increasing glucose concentration are shown in Figure 9 for the SPR D-shaped fiber sensor. As the glucose RI rises, so does the sensitivity of the proposed sensor. The decrease in the refractive index difference between the two media may be responsible for this influence on the SPR D-shaped fiber structure [13].

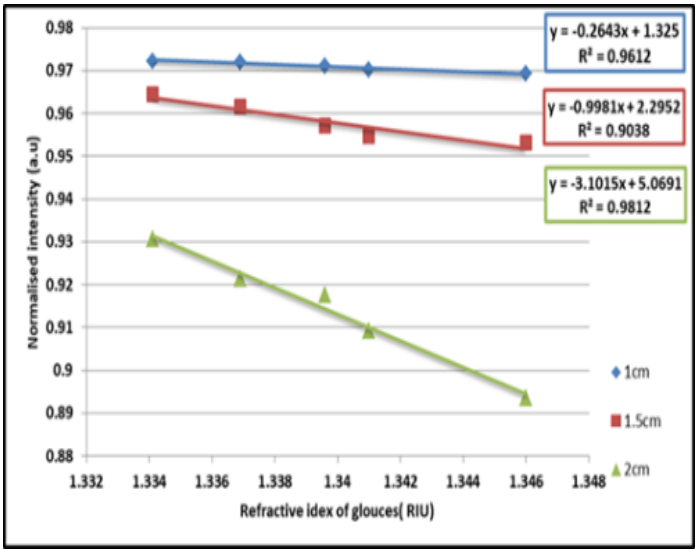

Fig. 9: Intensity normalized by sensing length for SPR D-shaped fiber sensors.

5. Sensitivity analyses and enhancement

The suggested D-shape fiber sensor and SPR D-shape fiber sensor performance have been evaluated in this study for glucose materials which have a range of 1.334 to 1.346 RIU for their refractive indices.
The sensitivity for each sensor at various sensing lengths is the absolute number obtained by the slope of the line fitting. By using the following equation to compute the sensitivity S:

$$S = \left|\frac{\Delta\ I_N}{\Delta\ n}\right| \qquad (1)$$

Where ΔI_N is the variation in the normalized intensity and Δn indicates the material's fluctuating refractive index [14]. Table 2 displays the calculated sensitivity using eq. (1). Figure 10 shows the sensitivity vs. sensing length relationship for D-shape fiber sensors and SPR D-shape fiber sensors. An SPR D-shape fiber sensor with a 2 cm detecting length was used to obtain the high sensitivity of 3.1 au. / RIU.

The addition of an Au nanolayer to the D-shaped fiber sensor improves its sensitivity. The results of the experiments show that the SPR D-shaped fiber sensor has ~ a 15% enhancement in sensitivity compared with the D-shape fiber sensor.

Table 2. Sensitivity comparator and enhancement.

Sensing length	D-shape fiber sensor	SPR D-shape fiber sensor	Enhancement
	S	***S***	***En***
Ls = 1 cm	0.0849	0.2643	3.11 %
Ls =1.5 cm	0.1789	0.9981	5.58 %
Ls = 2 cm	0.2015	3.1	15.39 %

Table 3. Comparison of different fiber sensors for measuring refractive index.

Fiber sensor	Method	Analyte	Sensitivity	Ref
Un-cladding fiber	LSPR	sucrose solution	1.612 au/RIU	[17]
hetero-core structure	LSPR	glycerin solutions	2.93au/RIU	[18]
D-shape fiber	--	glycerin solutions	2.827 au/RIU	[19]
D-shape fiber	SPR	sucrose solution	3.101 au/RIU	This work

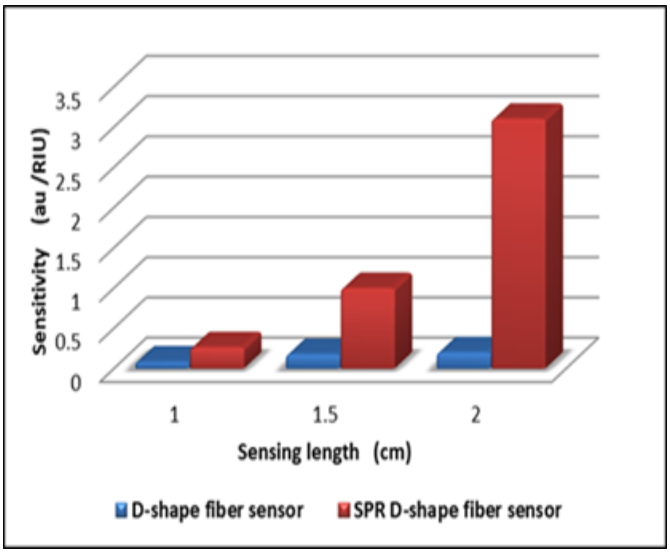

Fig. 10: The relationship between sensitivity and sensing length for IR fiber sensors.

The D-type optical fiber structure increases the effective detection area of the sensor by increasing the polishing depth of the fiber, resulting in improved sensitivity. The gold film on the flat section of the fiber structure enhances the field intensity of the local electric field, leading to improved sensor performance.

Finally, the results of the present work's SPR D-shaped fiber sensors are compared to those of other existing fiber sensor architectures in Table 3. Since the D-shape structure simply requires the side polishing of the multimode fiber, its manufacture is easy to fabricate and low cost from the others.

6. Conclusions

The current research describes the creation and design of a side-polished optical fiber sensor that is both straightforward and efficient in measuring values for the RI of glucose solutions. The sensor's sensing region is located within the uncoated section of the optical fiber cladding. The present study also examines the influence of the length of the exposed cladding section on the sensor's ability to monitor variations in refractive index at a reasonable range. The sensor underwent development and refinement through the utilization of surface plasmon resonance (SPR) characteristics. The experimental results of the developed sensors demonstrate that the SPR D-shape fiber sensor has ∼15% enhancement in sensitivity compared with the D-shape fiber sensor.

References

[1] Qazi, H. H., Mohammad, A. B., Ahmad, H., & Zulkifli, M. Z. “D-shaped polarization maintaining fiber sensor for strain and temperature monitoring”. Sensors, **16**(9), 1505.(2016) .
[2] Wong, A. C., Chung, W. H., Tam, H. Y., & Lu, C. “Single tilted Bragg reflector fiber laser for simultaneous sensing of refractive index and temperature”. Optics express, **19**(2), 409-414. (2011).
[3] Khaleel, W. A., & Al-Janabi, A. H. M. “High-sensitivity sucrose erbium-doped fiber ring laser sensor”. Optical Engineering, **56**(2), 026116-026116.(2017) .
[4] Salman, N. A., Taher, H. J., & Mohammed, S. A. “Tapered splicing points SMF-PCF-SMF structure based on Mach-Zehnder interferometer for enhanced refractive index sensing”. Iraqi Journal of Laser, **16**(A), 19-24.|((2017).
[5] Mohammed, S. A., & Al-Janabi, A. H. “All fiber chemical liquids refractive index sensor based on multimode interference”. Iraqi Journal of Laser, **17**(A), 33-39. (2018).
[6] Abbas, F. F., & Ahmed, S. S. “Photonic crystal fiber pollution sensor based on the surface plasmon resonance technology”. Baghdad Science Journal, **20**(2), 0452-0452. (2018).
[7] Jassam, G. M., Alâ, S. S., & Sultan, M. F. “Fabrication of a chemical sensor based on surface plasmon resonance via plastic optical fiber”. Iraqi Journal of Science, 765-771. (2020).
[8] Sarker, H., Alam, F., Khan, M. R., Mollah, M. A., Hasan, M. L., & Rafi, A. S. “Designing highly sensitive exposed core surface plasmon resonance biosensors”. Optical Materials Express, **12**(5), 1977-1990.(2022).
[9] Zhao, J., Cao, S., Liao, C., Wang, Y., Wang, G., Xu, X., ... & Wang, Y. “Surface plasmon resonance refractive sensor based on silver-coated side-polished fiber”. Sensors and Actuators B: Chemical, **230**, 206-211.(2016).
[10] Zakaria, R., Kam, W., Ong, Y. S., Yusoff, S. F. A. Z., Ahmad, H., & Mohammed, W. S. “Fabrication and simulation studies on D-shaped optical fiber sensor via surface plasmon resonance”. Journal of Modern optics, **64**(14), 1443-1449.(2017).
[11] Yasin, M., Irawati, N., Isa, N. M., Harun, S. W., & Ahmad, F.“Graphene coated silica microfiber for highly sensitive magnesium sensor”. Sensors and Actuators A: Physical, **273**, 67-71. (2018).
[12] Niu, L. Y., Wang, Q., Jing, J. Y., & Zhao, W. M. “Sensitivity enhanced D-type large-core fiber SPR sensor based on Gold nanoparticle/Au film co-modification”. Optics Communications, **450**, 287-295. (2019).
[13] Yasin, M., Irawati, N., Isa, N. M., Harun, S. W., & Ahmad, F. “Graphene coated silica microfiber for highly sensitive magnesium sensor”. Sensors and Actuators A: Physical, **273**, 67-71.(2018).
[14] Qazi, H. H., Memon, S. F., Ali, M. M., Irshad, M. S., Ehsan, S. A., Salim, M. R. B.,& Idrees, M. “Surface roughness and the sensitivity of D-shaped optical fibre sensors”. Journal of Modern Optics, **66**(11), 1244-1251. (2019).
[15] Abbas, H.K., Mahdi, Z.F., “Fabricate a Highly Sensitive Surface Plasmon Resonance Optical Fiber Sensor Based on a D-Shape Fiber Coated with Gold (Au) Nano-Layer”. Results in Optics, **12**, 100497.(2023).
[16] Saad, Y., Selmi, M., Gazzah, M. H., & Belmabrouk, H. “Numerical modeling of surface plasmon resonance response of fiber optic sensors”. International Conference on Engineering & MIS (ICEMIS).1-4. (2017).

[17] Liu, S., Su, S., Chen, G. and Zeng, X., "January. Optical fiber sensors based on local surface plasmon resonance modified with silver nanoparticles". Second International Conference on Intelligent System Design and Engineering Application .1444-1447.(2012).
[18] Hosoki, A., Nishiyama, M. and Watanabe, K., "Localized surface plasmon sensor based on gold island films using a hetero-core structured optical fiber". applied optics, **56**(23), 6673-6679.(2017).
[19] Sequeira F, Duarte D, Bilro L, Rudnitskaya A, Pesavento M, Zeni L and Cennamo N "Refractive Index Sensing with D-Shaped Plastic Optical Fibers for Chemical and Biochemical Applications" Sensors, **16**, 2119, (2016).
[20] Peng, Gang-Ding. "Handbook of Optical Fibers.", (2019).
[21] Gong, Pengqi, et al. "Optical fiber sensors for glucose concentration measurement: A review." Optics & Laser Technology, **139**, 106981, (2021).

تطوير الألياف الضوئية على شكل D وتحسينها كمستشعر لمؤشرات الانكسار باستخدام رنين البلازمون السطحي

هبة خضير عباس * , زينب فاضل مهدي

معهد الليزر للدراسات العليا، جامعة بغداد، بغداد، العراق

*البريد الالكتروني للباحث: heba.khodair1101a@ilps.uobaghdad.edu.iq

الخلاصة: تعرض هذه المقالة تطوير واستخدام مستشعر الألياف البصرية المصقول جانبياً الذي يمكنه تحديد مستويات معامل الانكسار المتغيرة داخل محلول الجلوكوز من خلال تنفيذ تأثير رنين البلازمون السطحي. تم إنشاء الكاشف باستخدام ألياف السليكا الضوئية، والتي خضعت لعملية تجريد الكسوة التي أسفرت عن ثلاثة أطوال متميزة ، تليها طريقة تلميع لإزالة جزء من قطر الألياف وإنتاج مقطعي عرضي على شكل حرف D . أثناء تجربة محلول الجلوكوز ، كشف مستشعر الألياف البصرية المصقول جانبياً D- shaped fiber عن حساسية كشف تبلغ (0.2015 au./RIU). من أجل تحسين الحساسية ، تعرض جهاز الاستشعار لعملية طلاء باستخدام طبقة رقيقة من الذهب (Au) بسمك 50 نانومتر. خضع المستشعر SPR D- shaped fiber لاحقا لسلسلة من الاختبارات باستخدام نفس محاليل الجلوكوز كما في التجارب السابقة. لوحظ تحسن ملحوظ في الحساسية عند استخدام الذهب كمادة استشعار ، حيث بلغت حساسية المستشعر (3.101 au / RIU).